MOLECULAR MODELING STUDY OF SULFATE AND PHOSPHATE ADSORPTION AT THE MINERAL-WATER INTERFACE

by

Kristian W. Paul

A dissertation submitted to the Faculty of the University of Delaware in partial fulfillment of the requirements for the degree of Doctor of Philosophy in Plant and Soil Sciences

Summer 2007

MOLECULAR MODELING STUDY OF SULFATE AND PHOSPHATE ADSORPTION AT THE MINERAL-WATER INTERFACE

by

Kristian W. Paul

Approved: ______________________________

Donald L. Sparks, Ph.D.
Chair of the Department of Plant and Soil Sciences

Approved: ______________________________

Robin W. Morgan, Ph.D.
Dean of the College of Agriculture and Natural Resources

Approved: ______________________________

Carolyn A. Thoroughgood, Ph.D.
Vice Provost for Research and Graduate Studies

I certify that I have read this dissertation and that in my opinion it meets the academic and professional standard required by the University as a dissertation for the degree of Doctor of Philosophy.

Signed: ____
Donald L. Sparks, Ph.D.
Professor in charge of dissertation

I certify that I have read this dissertation and that in my opinion it meets the academic and professional standard required by the University as a dissertation for the degree of Doctor of Philosophy.

Signed: ____
Douglas J. Doren, Ph.D.
Member of dissertation committee

I certify that I have read this dissertation and that in my opinion it meets the academic and professional standard required by the University as a dissertation for the degree of Doctor of Philosophy.

Signed: ____
George W. Luther, III, Ph.D.
Member of dissertation committee

I certify that I have read this dissertation and that in my opinion it meets the academic and professional standard required by the University as a dissertation for the degree of Doctor of Philosophy.

Signed: ____
James D. Kubicki, Ph.D.
External member of dissertation committee

ACKNOWLEDGEMENTS

This dissertation, not unlike any other dissertation, could not have come to fruition without the help of numerous dedicated individuals who, throughout the last five years, inspired me to research this topic. Above all, I would like to acknowledge my advisor Donald Sparks who allowed me to pursue this research topic at the risk of not knowing whether we'd be successful. Furthermore, Donald Sparks continually trusted in me and put his faith into this pursuit, even when I was lacking thereof. I could not have asked for a more dedicated advisor, a better work environment, or a mentor than Donald Sparks. I am forever grateful. I would like to also acknowledge the following dedicated individuals:

Jim Kubicki, who took me under his wing during the past three years, was an unrelenting advocator of our research, provided an enormous amount of computational resources, and served as a committee member. I am very appreciative for Jim Kubicki's willingness to help and enthusiasm to collaborate.

Doug Doren and George Luther, both of whom inspired me tremendously in their classrooms, also served as committee members. Thank you both for always being willing to answer my questions and teaching me the essentials of quantum and inorganic chemistry. This pursuit would have been in vain without your help. My only wish is that you've both imparted me an ounce of your respective expertise and knowledge.

Daniel Strongin, Daniel Tunega, and Andrei Bandura, all of whom were coauthors on several manuscripts, served as inspiring research collaborators,

colleagues, and mentors. It was my utmost pleasure to publish our research with each of you. I hope our professional collaborations continue.

Douglas O'Neal and Jason Holmes for always being willing to help me run Gaussian and VASP calculations on the servers they managed at UD and PSU, respectively.

Ryan Tappero, who was a fellow graduate student and friend, never tired of reviewing my manuscripts and always provided a fresh and insightful perspective.

My friends and family at Glorious Presence Church who were always lifting me up in prayer.

My family who indirectly reminded me that successfully completing the dissertation and earning a Ph.D. was less about me and much more about others.

DEDICATION

I dedicate this dissertation to my loving wife Jalice who, throughout the last several years, celebrated the best of days with me and ceaselessly encouraged and strengthened me on the worst of days. I love you.

EPIGRAPH

A voice says, "Cry out."

And I said, "What shall I cry?"

"All men are like grass,

and all their glory is like the flowers of the field.

The grass withers and the flowers fall,

because the breath of the LORD blows on them.

Surely the people are grass.

The grass withers and the flowers fall,

but the word of our God stands forever."

Isaiah 40: 6-8, NIV

TABLE OF CONTENTS

APPENDICES

LIST OF TABLES

LIST OF FIGURES

ABSTRACT

The transport and bioavailability of sulfate and phosphate are significantly affected by adsorption reactions with soil minerals. Elucidating the adsorption mechanisms and kinetics is critical to improving surface complexation models, which are used to simulate the reactive transport of nutrients in soils. The objective of this investigation was to utilize computational DFT methods to improve our understanding of sulfate and phosphate adsorption at the mineral-H_2O interface.

The effect of dehydration on sulfate adsorption at the α-Fe_2O_3-H_2O interface was investigated, using ATR-FTIR spectroscopy and DFT calculations. The DFT calculations were performed with edge-sharing dioctahedral Fe^{3+} cluster models of sulfate and bisulfate complexes. The DFT calculations suggested that sulfate formed a monodentate or bidentate bridging complex under hydrated conditions, but that bisulfate formed under dehydrated conditions (i.e., speciation change). A QMD simulation of monodentate bisulfate at the (101) α-FeOOH-H_2O interface, however, suggested that a speciation change is probably reversible.

The energies of sulfate adsorption pathways on edge-sharing dioctahedral Al^{3+} and Fe^{3+} cluster models were estimated with DFT calculations. The DFT-calculated adsorption energies were directly related to the H^+/SO_4^{2-} stoichiometry and the overall charge of the Al^{3+} and Fe^{3+} clusters. DFT-calculated adsorption energies for bidentate

bridging and monodentate sulfate on a +1 charged Fe^{3+} cluster agreed reasonably well with experimental measurements of sulfate adsorption on α-FeOOH.

The binding geometries of bidentate bridging and monodentate sulfate complexes at the Fe-(hydr)oxide-H_2O interface were investigated, using cluster and periodic slab DFT calculations. The DFT cluster calculations were performed with edge-sharing dioctahedral Fe^{3+} models. The periodic DFT calculations were performed with a slab model of the (100) α-FeOOH surface. The cluster model predictions of the interatomic distances and angles of monodentate and bidentate bridging sulfate were in good agreement with the periodic slab model predictions.

QMD simulations were performed to better understand the dynamical behavior of sulfate and phosphate complexes at the (101) α-FeOOH-H_2O interface. The H-bonding interactions of sulfate and phosphate with α-FeOOH surface OH functional groups and with solvent H_2O molecules were investigated. To explain why phosphate is a stronger competitor than sulfate for α-FeOOH surface sites, a proton-assisted ligand exchange mechanism was proposed.

Chapter 1

INTRODUCTION

1.1 Environmental Significance

1.1.1 Sulfate

Sulfur is an essential plant nutrient and a constituent of enzymes that regulate photosynthesis and nitrogen fixation. In addition, sulfur is a constituent of several amino acids and vitamins. The dominant chemical form of sulfur available for plant uptake is the sulfate anion. Sulfate minerals, for example $CaSO_4$(s) and $MgSO_4$(s), have high solubility in soils and dissolved sulfate can be readily transported to surface or ground water. However, sulfate is adsorbed by Al- and Fe-(hydr)oxides and 1:1 clay minerals (e.g. kaolinite). Sulfate adsorption is generally categorized as either outer-sphere or inner-sphere. Outer-sphere adsorption refers to the electrostatic attraction between a negatively-charged sulfate ion and positively-charged mineral surface sites (i.e., Coulombic attraction). Inner-sphere adsorption refers to ligand exchange between a negatively-charged sulfate ion and one or two functional groups coordinated to surface metal atoms [1]. An inner-sphere sulfate complex is directly coordinated to a mineral surface and, in comparison with an outer-sphere sulfate complex, will desorb less easily (i.e., more slowly available for plant uptake) [2].

Despite its vital role in plant physiology, sulfate can be associated with severe environmental problems, such as acid mine drainage (AMD) and acid precipitation. For example, unusually high concentrations of dissolved sulfate are common in AMD. In excess of 250 mg L^{-1}, sulfate is a potential contaminant [3]. The unusually high concentrations of dissolved sulfate can be mitigated by adsorption to amorphous Fe-(hydr)oxides. Unfortunately, however, alkalinity treatment methods (e.g. application of $CaCO_3(s)$ or NaOH(s)) are typically used to precipitate and immobilize toxic metals in AMD. Alkalinity treatment methods can inadvertently enhance the transport of sulfate to surface or ground water resources [4]. For soils that receive acid precipitation, the importance of sulfate transport is profound. For example, sulfate transport in forest soils can enhance the transport of base cation nutrients. Hence, sulfate is considered as an indirect conserver of base cations. The transport of base cations, for example Ca^{2+} and Mg^{2+}, is particularly problematic because of their replacement by Al^{3+} ions to maintain soil solution electroneutrality (Al^{3+} ions are toxic to many organisms) [2].

1.1.2 Phosphate

Phosphorus is an essential plant nutrient and a constituent of adenosine triphosphate, which is the energy source of many biochemical processes, such as nutrient acquisition and translocation. In addition, phosphorus is an important constituent of deoxyribonucleic acid, ribonucleic acid, and phospholipids. Similar to sulfur, the dominant chemical forms of phosphorus available for plant uptake are the phosphate anions (i.e., HPO_4^{2-} and $H_2PO_4^-$), in addition to a minor component of organic phosphorus compounds. In contrast to sulfur, however, the quantity of available phosphate in solution or as soluble minerals is negligible. The plant availability of phosphate is minimal in soils, principally because of phosphorus fixation and phosphorus retention [2]. In phosphorus fixation, phosphate forms inorganic Al, Fe, and Ca minerals that have very low solubility over a wide pH range (e.g. $AlPO_4 \cdot 2H_2O$, $FePO_4 \cdot 2H_2O$, and $[3Ca_3(PO_4)_2] \cdot Ca(OH)_2$). In phosphorus retention, phosphate tends to form strong inner-sphere complexes that are not easily desorbed and therefore unavailable for plant uptake. In comparison with sulfate, inner-sphere phosphate complexes exhibit greater affinity for Fe-(hydr)oxides [5], and are therefore significantly less available for plant uptake.

Despite its vital role in plant physiology and bioenergetics, phosphate can also severely affect environmental quality. In particular, too little plant-available phosphate can cause land degradation. Conversely, too much plant-available phosphate can cause accelerated eutrophication. In both cases, the effects of phosphate on environmental quality are related to its plant availability [2]. For example, when the vegetation of a natural ecosystem is removed for production agriculture, plant-available phosphorus is normally depleted through erosion, runoff, and biomass loss. Consequently, the initial regrowth of a production crop may be sparse and accelerate further erosion, thereby promoting land degradation. On the other hand, accelerated eutrophication is caused by high concentrations of phosphorus (typically as phosphate) entering fresh water or marine resources (e.g. [6]). Excess phosphorus stimulates the growth of algae and other higher plants. When the algae and higher plants die, microorganisms can exhaust the available dissolved oxygen by consuming it for decomposition. A significant reduction of available dissolved oxygen, in turn, limits the growth of fish and can potentially lead to massive fish kills. Thus, accelerated eutrophication is detrimental to ecological health.

1.2 IR Vibrational Spectroscopy – A Brief Review of Model Systems

Given that the plant availability and transport of sulfate and phosphate are predominantly controlled by adsorption to soil minerals, an understanding of the reaction mechanisms and kinetics has long been sought. In particular, numerous IR vibrational spectroscopic studies have been performed to investigate the molecular-scale adsorption of sulfate and phosphate by Fe-(hydr)oxide minerals. Previous IR vibrational spectroscopic studies were performed either *ex situ* (without water present) or *in situ* (with water present). The application of IR vibrational spectroscopy to the investigation of sulfate and phosphate adsorption by Fe-(hydr)oxide minerals will now be briefly reviewed. It is important to note, however, that IR vibrational spectroscopy has also been applied to the investigation of sulfate and phosphate adsorption by Al-(hydr)oxide minerals. Nevertheless, for the purposes of this brief discussion, studies exclusively involving Fe-(hydr)oxide minerals will be mentioned, as their use has been more frequent. First, IR vibrational spectroscopic studies of sulfate adsorption performed *ex situ* and *in situ* will be briefly reviewed.

1.2.1 *Ex Situ* and *In Situ* Sulfate Adsorption

A number of seminal studies were published in the 1970's that investigated the mechanisms of sulfate and phosphate (Section 1.2.2) adsorption by Fe-(hydr)oxide minerals, using *ex situ* IR vibrational spectroscopy. For example, Parfitt and Smart [7, 8] proposed that sulfate formed a bidentate bridging complex on Fe-(hydr)oxide surfaces. Furthermore, Parfitt and Smart [7, 8] proposed a ligand exchange mechanism, in which two adjacent OH or OH_2 functional groups were replaced by one sulfate ion. Harrison and Berkheiser [9] also proposed that sulfate formed a bidentate bridging complex on freshly precipitated, hydrous Fe-(hydr)oxide (presumably ferrihydrite). Turner and Kramer [10] investigated the adsorption of sulfate by goethite (α-FeOOH) and hematite (α-Fe_2O_3), using *ex situ* IR vibrational spectroscopy. Turner and Kramer [10] proposed that sulfate preferably formed a bidentate bridging complex, in contrast to a monodentate complex. In general, therefore, sulfate was unanimously proposed to form a bidentate bridging complex on Fe-(hydr)oxide surfaces based upon *ex situ* IR vibrational spectroscopic evidence.

In 1997, Hug [11] published the first *in situ* IR vibrational spectroscopic study of sulfate adsorption. The attenuated total reflectance (ATR) Fourier transform infrared (FTIR) spectroscopic technique was applied to sulfate adsorption at the α-Fe_2O_3-H_2O interface. In the study of sulfate or phosphate adsorption, ATR-FTIR spectroscopy is undoubtedly superior to conventional FTIR spectroscopic techniques (e.g. transmission and diffuse-reflectance). Specifically, ATR-FTIR spectroscopy can be applied to the investigation of adsorption at the mineral-H_2O interface in real-time, and as a function of pH, ionic strength, reactant concentration (i.e., surface loading), flow-rate, and temperature. The study by Hug [11] revealed two particularly noteworthy findings with respect to previously published *ex situ* studies. First, Hug [11] proposed that sulfate formed a monodentate complex at the α-Fe_2O_3-H_2O interface. Second, upon removal of the solvent (i.e., dehydration), Hug [11] observed a diagnostic IR spectral feature that suggested a change in sulfate coordination or speciation. These findings indicated that our understanding of sulfate adsorption at the Fe-(hydr)oxide-H_2O interface was incomplete.

In situ ATR-FTIR spectroscopic studies of sulfate adsorption at the α-FeOOH-H_2O interface have also been performed [12, 13]. For example, Peak *et al.* [12] investigated sulfate adsorption at the α-FeOOH-H_2O interface as a function of pH, ionic strength, and reactant concentration. A novel mechanism was proposed, namely, that sulfate adsorption occurred as a continuum of outer- and inner-sphere complexes. At pH values less than 6, Peak *et al.* [12] proposed that sulfate formed both outer- and inner-sphere monodentate sulfate complexes. On the other hand, sulfate only formed outer-sphere complexes at pH values greater than 6. Wijnja and Schulthess [13] investigated sulfate adsorption at the α-FeOOH-H_2O interface, using *in situ* ATR-FTIR and Raman spectroscopy. Wijnja and Schulthess [13] arrived at essentially the same conclusions as Peak *et al.* [12], regarding the formation of outer- and inner-sphere sulfate complexes as a function of pH. The novel idea that sulfate adsorption occurred as a continuum of outer- and inner-sphere complexes [12, 13] was in stark contrast to previously published interpretations based upon *ex situ* IR vibrational spectroscopic evidence.

1.2.2 *Ex Situ* and *In Situ* Phosphate Adsorption

In comparison with the aforementioned sulfate adsorption studies, interpretations of phosphate adsorption by Fe-(hydr)oxide minerals, based upon IR vibrational spectroscopic evidence, have been largely inconsistent. Parfitt and coworkers published several studies of phosphate adsorption by Fe-(hydr)oxide minerals, using *ex situ* IR vibrational spectroscopy [14-17]. Similar to their sulfate adsorption studies, Parfitt and coworkers proposed that phosphate formed a bidentate bridging complex. Furthermore, Parfitt and coworkers [14-17] proposed a ligand exchange mechanism in which two adjacent OH or OH_2 functional groups were replaced by one phosphate ion [14-17]. It should be noted, however, that a bidentate bridging phosphate complex was proposed, regardless of the type of Fe-(hydr)oxide mineral studied.

Nanzyo and Watanabe [18] also proposed that phosphate formed a bidentate bridging complex on α-FeOOH. In a subsequent study, Nanzyo [19] proposed that phosphate formed a bidentate bridging complex on Fe-hydroxide gels (presumably ferrihydrite) at high pH, but formed an iron phosphate precipitate at low pH. Persson *et al.* [20] also investigated the adsorption of phosphate by α-FeOOH, using *ex situ* IR vibrational spectroscopy (diffuse-reflectance FTIR). In contrast to the aforementioned phosphate adsorption studies, Persson *et al.* [20] proposed that phosphate formed diprotonated, monoprotonated, and deprotonated monodentate phosphate complexes at low, intermediate, and high pH values, respectively.

Parfitt and Atkinson [21] published the first quasi-*in situ* IR vibrational spectroscopic study of phosphate adsorption at the α-FeOOH-H_2O interface. The measurements were performed on wet pastes, using transmission IR spectroscopy, as opposed to contemporary ATR-FTIR spectroscopic measurements, performed on thin films. Nevertheless, Parfitt and Atkinson [21] asserted that phosphate formed a bidentate bridging complex, though it was suggested that the protonation state of the phosphate complex would vary as a function of pH. Since the study performed by Parfitt and Atkinson [21], several studies have been published using *in situ* IR vibrational spectroscopy to investigate phosphate adsorption at the Fe-(hydr)oxide-H_2O interface.

Tejedor-Tejedor and Anderson [22] and Luengo *et al.* [23], for example, investigated the adsorption of phosphate at the α-FeOOH-H_2O interface, using *in situ* cylindrical internal reflectance and ATR-FTIR spectroscopic methods, respectively. Tejedor-Tejedor and Anderson [22] proposed that phosphate formed protonated bidentate bridging, deprotonated bidentate bridging, and deprotonated monodentate complexes as a function of pH and reactant concentration. Luengo *et al.* [23]

investigated the kinetics of phosphate adsorption at the α-FeOOH-H_2O interface and proposed that phosphate formed protonated and deprotonated bidentate bridging complexes, depending upon the sample pH.

Arai and Sparks [24] investigated the adsorption of phosphate at the ferrihydrite-H_2O interface, using ATR-FTIR spectroscopy. At pH values greater than 7.5, Arai and Sparks [24] proposed that phosphate formed a deprotonated bidentate bridging complex. However, between pH 4 and 6, protonated inner-sphere phosphate complexes were proposed to form at the ferrihydrite-H_2O interface (the binding geometry of the protonated inner-sphere phosphate complex was not identified). Most recently, Elzinga and Sparks [25] investigated the adsorption of phosphate at the α-Fe_2O_3-H_2O interface, using ATR-FTIR spectroscopy. Based upon experiments performed with D_2O and H_2O, Elzinga and Sparks [25] proposed that phosphate formed monoprotonated bidentate bridging and monodentate complexes between pH 3.5 and 7. At pH values between 8.5 and 9, Elzinga and Sparks [25] proposed that phosphate formed both monoprotonated and deprotonated monodentate complexes at the α-Fe_2O_3-H_2O interface.

1.3 Research Justification

Collectively, the IR vibrational spectroscopic studies briefly discussed in Sections 1.2.1 and 1.2.2 revealed unprecedented molecular-scale insight into the adsorption of sulfate and phosphate at the Fe-(hydr)oxide-H_2O interface, over a wide range of experimental conditions. Despite the significant advances achieved, however, there remains little consensus with respect to the mechanisms of sulfate and phosphate adsorption at the Fe-(hydr)oxide-H_2O interface. In particular, since the analysis of IR vibrational spectroscopic data can be ambiguous, it is not well understood whether sulfate and phosphate complexes at the Fe-(hydr)oxide-H_2O interface are outer- or inner-sphere, monodentate or bidentate bridging, protonated or deprotonated, etc. Two principal limitations continue to restrict the application of IR vibrational spectroscopic methods to the elucidation of sulfate and phosphate adsorption mechanisms at the Fe-(hydr)oxide-H_2O interface. First, the interpretation of IR spectra is generally based upon a qualitative point group symmetry analysis of the sulfate and phosphate complexes. Second, the interpretation of IR spectra is hindered by a lack of available reference compounds needed for empirical fingerprinting analysis [25].

In the aforementioned IR vibrational spectroscopic studies, assignments of the sulfate and phosphate IR-active vibrational modes were based upon a point group symmetry analysis of the complexes. For a description of how point group symmetry analyses can be qualitatively related to the binding geometry of a sulfate or phosphate complex, refer to publications by Peak *et al.* [12] and Elzinga and Sparks [25], respectively. Briefly, the binding geometry of a sulfate or phosphate complex can be tentatively identified by the IR activity of its ν_1 vibrational mode (symmetric stretch) and degeneracy of its ν_3 vibrational mode (asymmetric stretch). In other words, the IR activity of ν_1 and degeneracy of ν_3 are qualitatively related to the point group symmetry of a particular sulfate or phosphate complex.

For example, as discussed by Elzinga and Sparks [25], aqueous PO_4^{3-} has T_d point group symmetry. As a result of its T_d point group symmetry, aqueous PO_4^{3-} will exhibit one IR-active ν_3 vibrational mode (i.e., triply degenerate). Aqueous HPO_4^{2-} has C_{3v} point group symmetry and will exhibit two IR-active ν_3 vibrational modes and an IR-active ν_1 vibrational mode. Likewise, aqueous $H_2PO_4^-$ has C_{2v} point group symmetry and will exhibit three IR-active ν_3 vibrational modes and an IR-active ν_1 vibrational mode. Since the IR-activity of the vibrational modes of an aqueous phosphate species are determined by its point group symmetry, similar arguments have been used to interpret the binding geometries of phosphate complexes. For example, if the ν_1 vibrational mode and two ν_3 vibrational modes are IR-active, a deprotonated monodentate phosphate complex can be proposed (i.e., C_{3v} point group symmetry). Similarly, if the ν_1 vibrational mode and three ν_3 vibrational modes are IR-active, a deprotonated bidentate bridging phosphate complex can be proposed (i.e., C_{2v} point group symmetry).

Unfortunately, the IR-activity (and energy) of the vibrational modes of a sulfate or phosphate complex do not only depend upon its binding geometry, but also upon its protonation state and H-bonding to hydroxyl functional groups. Consequently, interpretations of the binding geometry of a sulfate or phosphate complex are often qualitative and imprecise. For example, if four IR-active vibrational modes (i.e., C_{2v} point group symmetry) are measured for adsorbed phosphate at the Fe-(hydr)oxide-H_2O interface, then a minimum of four binding geometries could be possible: bidentate bridging PO_4^{3-}, bidentate bridging $H_2PO_4^-$, monodentate HPO_4^{2-}, and monodentate PO_4^{3-} H-bonded to an OH/H_2O functional group. It is important to recall that the transport and bioavailability of sulfate and phosphate are directly related to their interactions with mineral surfaces (e.g. binding geometries). The limited applicability of point group symmetry analysis to the investigation of phosphate adsorption at the Fe-(hydr)oxide-H_2O interface, for example, led Arai and Sparks [24] to suggest that extended X-ray absorption fine structure (EXAFS) spectroscopic measurements were needed to differentiate between different binding geometries.

The majority of our current understanding, with respect to the molecular-scale adsorption of sulfate and phosphate at the mineral-H_2O interface, is based upon qualitative interpretations of IR vibrational spectroscopic evidence. Unfortunately, many fundamental aspects of sulfate and phosphate adsorption at the mineral-H_2O interface remain inadequately understood. For example, under typical soil solution conditions, sulfate and phosphate will compete for identical mineral surface adsorption sites (e.g. [5]). The equilibrium distribution of sulfate and phosphate complexes (e.g. outer- versus inner-sphere or monodentate versus bidentate bridging) will depend upon the thermodynamic favorability of the various adsorption pathways. From an agricultural and environmental perspective, the equilibrium distribution of the complexes at the mineral-H_2O interface will directly influence the transport and plant availability of sulfate and phosphate in soils.

IR vibrational spectroscopic studies have revealed critical information regarding how sulfate and phosphate are coordinated to surface Al and Fe atoms of Al- and Fe-(hydr)oxide minerals, respectively (e.g. monodentate or bidentate bridging adsorption). In general, however, point group symmetry analyses do not describe the H-bonding interactions of sulfate and phosphate O atoms with surface hydroxyl functional groups. In fact, point group symmetry analyses often neglect these H-bonding interactions, which undoubtedly influence the binding geometries of sulfate and phosphate complexes. Furthermore, our understanding of the dynamics of sulfate and phosphate complexes at the mineral-H_2O interface is sorely lacking. As a result, the H-bonding dynamics of sulfate and phosphate complexes with surface hydroxyl functional groups have been largely overlooked.

Because of the limited ability of IR vibrational spectroscopy to elucidate the mechanisms of sulfate and phosphate adsorption at the mineral-H_2O interface, the need for reliable and accurate predictive methods has become increasingly important. A reliable and accurate predictive method that has recently emerged in soil chemistry is density functional theory (DFT). DFT calculations can be used to independently test and validate proposed adsorption mechanisms and have recently shown promise in soil chemistry (see Chapters 2 – 5 and references therein). For example, DFT calculations can predict the thermodynamic favorability of adsorption reactions and elucidate the H-bonding dynamics of sulfate and phosphate complexes at the mineral-H_2O interface. Furthermore, DFT calculations are not susceptible to the shortcomings of qualitative point group symmetry analyses.

Prior to the undertaking of this investigation, DFT calculations had not been applied to the investigation of sulfate and phosphate adsorption at the Al- and Fe-(hydr)oxide-H_2O interface. Therefore, the principal goal of this investigation was to utilize DFT calculations to improve our understanding of sulfate and phosphate adsorption at the Al- and Fe-(hydr)oxide-H_2O interface. This investigation will demonstrate that DFT calculations are indispensable, with respect to the improvement of our fundamental understanding of sulfate and phosphate adsorption at the mineral-H_2O interface.

1.4 Research Objectives

Based upon the need to improve our fundamental understanding of sulfate and phosphate adsorption at the Al- and Fe-(hydr)oxide-H_2O interface, DFT calculations were performed to address the following research objectives:

1) Investigate the effect of hydration on sulfate speciation at the Fe-(hydr)oxide-H_2O interface by predicting the IR-active vibrational modes of various sulfate complexes;
2) Investigate the thermodynamic favorability of sulfate adsorption pathways on variably-charged Al- and Fe-(hydr)oxides, with the

ultimate goal of elucidating the mechanisms of ligand exchange;

3) Investigate the binding geometries of inner-sphere sulfate complexes using static cluster and periodic slab DFT calculations, with the ultimate goal of theoretically fitting experimental EXAFS spectra;
4) Investigate the dynamical behavior of SO_4^{2-} and HPO_4^{2-} complexes at the (101) α-FeOOH-H_2O interface, and their H-bonding interactions with hydroxyl functional groups and solvent H_2O molecules.

1.5 References

1. Sparks, D. L., *Environmental Soil Chemistry*. 2nd ed.; Academic Press: San Diego, CA, 2003.

2. Brady, N. C.; Weil, R. R., *The Nature and Properties of Soils*. 12th ed.; Prentice Hall: Upper Saddle River, N.J., 1999.

3. Freeze, R. A.; Cherry, J. A., What Has Gone Wrong. *Ground Water* **1989,** *27*, (4), 458-464.

4. Rose, S.; Elliott, W. C., The Effects of pH Regulation Upon the Release of Sulfate from Ferric Precipitates Formed in Acid Mine Drainage. *Applied Geochemistry* **2000,** *15*, (1), 27-34.

5. Geelhoed, J. S.; Hiemstra, T.; VanRiemsdijk, W. H., Phosphate and Sulfate Adsorption on Goethite: Single Anion and Competitive Adsorption. *Geochimica Et Cosmochimica Acta* **1997,** *61*, (12), 2389-2396.

6. Khan, F. A.; Ansari, A. A., Eutrophication: An Ecological Vision. *Botanical Review* **2005,** *71*, (4), 449-482.

7. Parfitt, R. L.; Smart, R. S. C., Infrared Spectra from Binuclear Bridging Complexes of Sulfate Adsorbed on Goethite (α-FeOOH). *Journal of the Chemical Society-Faraday Transactions I* **1977,** *73*, 796-802.

8. Parfitt, R. L.; Smart, R. S. C., The Mechanism of Sulfate Adsorption on Iron Oxides. *Soil Science Society of America Journal* **1978,** *42*, (1), 48-50.

9. Harrison, J. B.; Berkheiser, V. E., Anion Interactions with Freshly Prepared Hydrous Iron Oxides. *Clays and Clay Minerals* **1982,** *30*, (2), 97-102.

10. Turner, L. J.; Kramer, J. R., Sulfate Ion Binding on Goethite and Hematite. *Soil Science* **1991,** *152*, (3), 226-230.

11. Hug, S. J., *In Situ* Fourier Transform Infrared Measurements of Sulfate Adsorption on Hematite in Aqueous Solutions. *Journal of Colloid and Interface Science* **1997,** *188*, (2), 415-422.

12. Peak, D.; Ford, R. G.; Sparks, D. L., An *In Situ* ATR-FTIR Investigation of Sulfate Bonding Mechanisms on Goethite. *Journal of Colloid and Interface Science* **1999,** *218*, (1), 289-299.

13. Wijnja, H.; Schulthess, C. P., Vibrational Spectroscopy Study of Selenate and Sulfate Adsorption Mechanisms on Fe and Al (hydr)oxide Surfaces. *Journal of Colloid and Interface Science* **2000,** *229*, (1), 286-297.

14. Atkinson, R. J.; Parfitt, R. L.; Smart, R. S., Infrared Study of Phosphate Adsorption on Goethite. *Journal of the Chemical Society-Faraday Transactions I* **1974,** *70*, (8), 1472-1479.

15. Parfitt, R. L.; Atkinson, R. J.; Smart, R. S. C., The Mechanism of Phosphate Fixation by Iron Oxides. *Soil Science Society of America Proceedings* **1975,** *39*, (5).

16. Parfitt, R. L.; Atkinson, R. J.; Smart, R. S. C., Mechanism of Phosphate Fixation by Iron Oxides. *Soil Science Society of America Journal* **1975,** *39*, (5), 837-841.

17. Parfitt, R. L.; Russell, J. D.; Farmer, V. C., Confirmation of Surface Structures of Goethite (α-FeOOH) and Phosphated Goethite by Infrared Spectroscopy. *Journal of the Chemical Society-Faraday Transactions I* **1976,** *72*, 1082-1087.

18. Nanzyo, M.; Watanabe, Y., Diffuse Reflectance Infrared Spectra and Ion Adsorption Properties of the Phosphate Surface Complex on Goethite. *Soil Science and Plant Nutrition* **1982,** *28*, (3), 359-368.

19. Nanzyo, M., Infrared Spectra of Phosphate Sorbed on Iron Hydroxide Gel and the Sorption Products. *Soil Science and Plant Nutrition* **1986,** *32*, (1), 51-58.

20. Persson, P.; Nilsson, N.; Sjoberg, S., Structure and Bonding of Orthophosphate Ions at the Iron Oxide-Aqueous Interface. *Journal of Colloid and Interface Science* **1996,** *177*, 263-275.

21. Parfitt, R. L.; Atkinson, R. J., Phosphate Adsorption on Goethite (α-FeOOH). *Nature* **1976,** *264*, (5588), 740-742.

22. Tejedor-Tejedor, M. I.; Anderson, M. A., The Protonation of Phosphate on the Surface of Goethite as Studied by CIR-FTIR and Electrophoretic Mobility. *Langmuir* **1990,** *6*, (3), 602-611.

23. Luengo, C.; Brigante, M.; Antelo, J.; Avena, M., Kinetics of Phosphate Adsorption on Goethite: Comparing Batch Adsorption and ATR-IR Measurements. *Journal of Colloid and Interface Science* **2006,** *300*, (2), 511-518.

24. Arai, Y.; Sparks, D. L., ATR-FTIR Spectroscopic Investigation on Phosphate Adsorption Mechanisms at the Ferrihydrite-Water Interface. *Journal of Colloid and Interface Science* **2001,** *241*, (2), 317-326.

25. Elzinga, E. J.; Sparks, D. L., Phosphate Adsorption onto Hematite: An *In Situ* ATR-FTIR Investigation of the Effects of pH and Loading Level on the Mode of Phosphate Surface Complexation. *Journal of Colloid and Interface Science* **2007,** *308*, (1), 53-70.

Chapter 2

EFFECT OF HYDRATION ON SULFATE ADSORPTION AT THE IRON OXIDE-WATER INTERFACE – A DFT AND FTIR STUDY

2.1 Abstract

The effect of hydration on sulfate adsorption and speciation at the Fe-(hydr)oxide-H_2O interface was investigated with density functional theory (DFT) and attenuated total reflectance Fourier transform infrared (ATR-FTIR) spectroscopy. The majority of DFT calculations were performed with the UB3LYP/6-31+G(d) method, using edge-sharing dioctahedral Fe^{3+} cluster models of sulfate and bisulfate complexes. The IR vibrational frequencies predicted by the DFT calculations were compared to previously published *in situ* and *ex situ* IR spectroscopic studies. The DFT cluster calculations predicted that sulfate forms a bidentate bridging or monodentate complex at the Fe-(hydr)oxide-H_2O interface. However, under dehydrated conditions, the DFT cluster calculations predicted that a speciation change occurs, in which sulfate protonates to form a bidentate bridging or monodentate bisulfate complex. To qualitatively determine whether the speciation change could be reversible, a quantum molecular dynamics (QMD) simulation was performed for a monodentate bisulfate complex at the (101) α-FeOOH-H_2O interface. The QMD simulation indicated that deprotonation of monodentate bisulfate was extremely rapid

under hydrated conditions (< 100 fs). Consequently, a speciation change resulting from dehydration is probably reversible as a function of rehydration.

2.2 Introduction

In a seminal study, Mortland and Raman [1] observed that the acidity of clay mineral surfaces (e.g. bentonite and nontronite) was directly related to moisture content (i.e., degree of relative humidity). The hydrolysis of exchangeable cations at the clay mineral surfaces was observed to increase as a function of decreasing moisture content. It was hypothesized that at low moisture content, water molecules were strongly polarized and their proton donating ability enhanced [1]. Previous investigators have also observed that dehydration significantly affects the redox properties and reactivity of manganese oxides [2, 3], and their adsorption affinity for the heavy metal Ni^{2+} [4]. Unfortunately, the effect of hydration on nutrient (e.g. sulfate) adsorption and speciation are poorly understood. Because the moisture content of soils fluctuates, an understanding of how hydration affects nutrient adsorption may be important to accurately predicting transport and bioavailability.

Several investigators have studied the adsorption of sulfate on Fe-(hydr)oxide minerals at the molecular-scale, using *ex situ* (i.e., without water present) infrared (IR) spectroscopy [5-8]. For example, Parfitt and Smart [6] proposed that sulfate formed a bidentate bridging complex on several different Fe-(hydr)oxide minerals. Turner and Kramer [8] also proposed that sulfate predominantly formed a bidentate bridging complex on goethite (α-FeOOH) and hematite (α-Fe_2O_3). The IR spectra reported by Turner and Kramer [8] agreed reasonably well with previously published IR studies [5-7]. In each of these studies, at least four IR-active vibrational modes were measured, and the consensus was that sulfate formed a bidentate bridging complex on Fe-(hydr)oxide minerals [5-8].

In the aforementioned IR spectroscopic studies, the IR-active vibrational modes of sulfate were assigned from a point group symmetry analysis. For an excellent description of how a point group symmetry analysis can be used to qualitatively determine the binding geometry of a sulfate complex, refer to Peak *et al.* [9]. Briefly, the binding geometry of a sulfate complex can be tentatively identified by determining the IR activity of its ν_1 vibrational mode (symmetric stretch) and degeneracy of its ν_3 vibrational mode (asymmetric stretch). The IR activity of ν_1 and degeneracy of ν_3 are qualitatively related to the point group symmetry of a sulfate complex. For example, if only the triply degenerate ν_3 vibrational mode is IR-active, an outer-sphere sulfate complex can be proposed (i.e., T_d point group). Similarly, if the ν_1 vibrational mode and two ν_3 vibrational modes are IR-active, a monodentate sulfate complex can be proposed (i.e., C_{3v} point group). In other words, an assignment can be proposed based upon the number of measured IR-active vibrational modes.

In recent years, the adsorption of sulfate on α-FeOOH and α-Fe_2O_3 has been investigated *in situ* (i.e., with water present), using attenuated total reflectance Fourier transform infrared (ATR-FTIR) spectroscopy [9-11]. For example, Hug [10] investigated the adsorption of sulfate on α-Fe_2O_3 as a function of reactant concentration and pH. The *in situ* ATR-FTIR spectra were characterized by an IR-active ν_1 vibrational mode and two IR-active ν_3 vibrational modes. Because three IR-active vibrational modes were measured, a monodentate sulfate complex (C_{3v} point group) was proposed [10]. Prior to Hug's study [10], the majority of IR experiments were performed *ex situ* [5-8], and the consensus assignment was a bidentate bridging complex based upon four observed IR-active vibrational modes. Hug [10] hypothesized that sample drying may affect the adsorption or speciation of sulfate. Interestingly, Hug observed a diagnostic IR-active vibrational mode ≥ 1200 cm^{-1} when experiments were performed *ex situ* [10]. The diagnostic IR-active vibrational mode ≥ 1200 cm^{-1} was also observed for aqueous sulfate solutions acidified below pH 2 (i.e., less than the pK_a of HSO_4^-). Thus, a relationship between hydration and pH was discovered that directly influenced the adsorption or speciation of sulfate.

The principal objective of this study was to use density functional theory (DFT) to investigate the effect of hydration on sulfate adsorption and speciation at the Fe-(hydr)oxide-H_2O interface. DFT is emerging as a valuable computational method used in soil chemistry to interpret the IR spectra of adsorption complexes at the mineral-H_2O interface (e.g. [12-16]). This investigation attempts to determine whether dehydration causes a change in sulfate coordination or speciation [10]. Results from this investigation will demonstrate that dehydration probably causes a speciation change, whereby sulfate accepts a proton to form bisulfate. A quantum molecular dynamics (QMD) simulation of a monodentate bisulfate complex at the (101) α-FeOOH-H_2O interface, however, will demonstrate that the speciation change is probably reversible as a function of rehydration. Two mechanisms are tentatively proposed to explain how dehydration may cause sulfate to accept a proton and form a bisulfate complex.

2.3 Materials and Methods

2.3.1 α-Fe_2O_3 Synthesis and Bulk Characterization

Synthetic α-Fe_2O_3 was prepared according to a method of Schwertmann and Cornell [17]. Briefly, 500 mL of a 0.20 M $Fe(ClO_4)_3$ solution were heated at 371 K for seven days. The product was centrifuged and washed several times with ultra-pure deionized (DI) H_2O, freeze dried, and stored as a powder in the dark. Powder X-ray diffraction verified that the synthesized α-Fe_2O_3 was free of mineral impurities. The BET-measured surface area was 47.8 $m^2\ g^{-1}$ (± 0.5 $m^2\ g^{-1}$) and the total pore volume was 0.074 $cm^3\ g^{-1}$ (sample degassed overnight at 373 K).

2.3.2 ATR-FTIR Spectroscopic Measurements and Data Analysis

The FTIR measurements were performed using a Thermo Electron™ NEXUS 670 spectrometer and a PIKE Technologies™ horizontal (H) ATR flow-through accessory mounted with a germanium (Ge) internal reflection element (IRE). The HATR flow-through accessory contained an internal volume of 100 μL. A liquid nitrogen-cooled mercury-cadmium-telluride (MCT-A) detector was used to acquire the IR spectra in the energy region of interest (ca. 1350 – 900 cm^{-1}). The IR spectra were acquired by adding 128 individual scans measured at 8 cm^{-1} resolution.

Approximately 200 μL of a 40 g L^{-1} suspension of α-Fe_2O_3 particles (ca. 8 mg of solid in a 70:30 H_2O:CH_3CH_2OH mixture) were deposited on the Ge IRE. After evaporation of the 70:30 H_2O:CH_3CH_2OH mixture, the Ge IRE was coated with a film of α-Fe_2O_3 particles. The α-Fe_2O_3 film was rinsed three times with 1 mL aliquots of DI H_2O adjusted to pH 4.0 with HCl. Rinsing removed α-Fe_2O_3 particles that were not in contact with the IRE and would therefore not be sampled by the IR beam. After the α-Fe_2O_3 film was rinsed, the IRE was placed in the flow-through accessory and sealed. DI H_2O (pH 4.0) was then pumped through the flow-though accessory for approximately 4 hours, using a peristaltic pump (ca. 500 μL min^{-1}).

After the α-Fe_2O_3 film was hydrated, a single beam background spectrum was acquired, in order to sample the spectrometer atmosphere, IRE, α-Fe_2O_3 film, and aqueous solution. A second single beam spectrum was immediately acquired, in order to generate a baseline for the sulfate adsorption experiment. In principle, IR spectra acquired after the baseline was generated should have only measured sulfate introduced into the system that interacted with the α-Fe_2O_3 film. The input solution was then switched to 50 μM Na_2SO_4 (pH 4.0) and pumped through the flow-through accessory for approximately 1 hour. An IR spectrum was acquired every 5 minutes until the IR spectra were superimposed. This condition likely represented complete loading of the α-Fe_2O_3 surface sites with sulfate. The 50 μM Na_2SO_4 solution was then switched back to DI H_2O (pH 4.0), which was pumped through the flow-through accessory for approximately 1 hour to remove sulfate remaining in solution. No differences were observed in the IR spectra before or after rinsing with DI H_2O.

An inverse second derivative spectrum (ISDS) was used to estimate the energies of the IR-active vibrational modes of sulfate measured by the ATR-FTIR experiment. The peak maxima identified in the ISDS corresponded to peak maxima in the ATR-FTIR spectrum. For the ISDS, baseline correction was not necessary. To test the validity of peak maxima tentatively identified in the ISDS, non-linear peak fitting was also performed (linear baseline correction applied to data set). Non-linear peak fitting was performed in Origin™ 6.0. Four Gaussian or Lorentzian functions were needed to reasonably fit the IR spectrum. The initial peak positions corresponded to the peak maxima identified in the ISDS, which resulted in a high quality fit (r^2=0.99). A second fit was performed using only three Gaussian functions. Non-linear peak fitting with only three Gaussian functions resulted in a significantly lower quality fit ($r^2 \approx 0.8$, data not shown). Adjustable parameters in the non-linear peak fitting included the peak center, amplitude, and FWHM. Negative Gaussian or Lorentzian functions were not permitted in the optimization of the non-linear peak fit.

2.3.3 DFT Calculations

The DFT calculations were performed with static configurations of edge-sharing dioctahedral Fe^{3+} cluster models. Similar edge-sharing dioctahedral cluster models of metal cations, for example Al^{3+} and Mg^{2+}, have been shown to reproduce the main geometrical features of metal oxides and clay minerals [18]. The edge-sharing dioctahedral Fe^{3+} cluster models were coordinated with sulfate (bidentate bridging, monodentate, and H-bonded) or bisulfate (bidentate bridging and monodentate) complexes (see Figure 2.3). The overall charge of the edge-sharing dioctahedral Fe^{3+} cluster models was determined by the ratio of terminating OH and OH_2 functional groups. In this investigation, the overall charge of the sulfate and bisulfate cluster models was neutral or +1, respectively. Therefore, the cluster models simulated adsorption below the pH_{pzc} (i.e., $pH \leq pH_{pzc}$, where pH_{pzc} is defined as the pH at which the net surface charge density equals zero [19]).

To simulate a hydrated environment, several explicit H_2O molecules were H-bonded to the sulfate and bisulfate complexes (see Figure 2.3). Experimental studies have shown that hydration can significantly influence the vibrational modes of oxyanion complexes [10, 20]. It should be noted that including at least four explicit H_2O molecules was necessary to maintain the structural integrity of the edge-sharing dioctahedral Fe^{3+} cluster models. Therefore, simulating completely dry conditions (no explicit H_2O molecules H-bonded to the (bi)sulfate complexes) could not be realistically achieved. Despite the simplicity of these cluster models, similar DFT studies have successfully compared energy-minimized binding geometries and predicted IR vibrational frequencies to spectroscopic measurements [12-16, 21-25].

The DFT calculations were performed with Gaussian 03 [26]. In this study, the DFT calculations were performed with the unrestricted Becke 3-parameter nonlocal-exchange functional [27, 28] and the gradient-corrected correlation functional of Lee *et al.* [29], denoted UB3LYP. The 6-31+G(d) all-electron basis set was used to minimize the total electronic energy. The 6-311+G(d,p) all-electron basis set was also used for the bidentate bridging cluster models, to evaluate potential differences in the predicted IR-active vibrational frequencies (i.e., effect of increased valence orbital splitting and addition of polarization functions to the H atoms). The high-spin state of Fe^{3+} was specified for each Fe atom.

The edge-sharing dioctahedral Fe^{3+} cluster models were geometry optimized without symmetry or geometrical constraints. Frequency calculations were subsequently performed to determine whether the geometry optimization had successfully located a potential energy minimum (i.e., no imaginary frequencies). The DFT-predicted IR-active vibrational frequencies were compared to previous experimental IR spectroscopic studies. It should be noted, however, that only one static configuration was geometry-optimized for each sulfate and bisulfate cluster model. Therefore, the potential energy minima did not likely correspond to the global minima for these configurations. Conformational analysis of the potential energy surfaces was not attempted.

To qualitatively determine whether a speciation change caused by dehydration would be reversible, a QMD simulation was performed for a monodentate bisulfate complex at the (101) α-FeOOH-H_2O interface. For complete details and references related to the QMD simulation, refer to Section 5.3.2 of Chapter 5. Briefly, the geometry-optimized monodentate HPO_4^{2-} system investigated in Chapter 5 was replaced with HSO_4^- (i.e., P atom replaced by S atom). To maintain a neutrally-charged simulation cell, a singly coordinated OH_2 functional group adjacent to the monodentate HSO_4^- complex was replaced with an OH functional group. The QMD simulation was performed using the *NVT* canonical ensemble at 300 K for 12 ps. The equilibration phase was approximately equal to 6 ps.

2.4 Results

2.4.1 ATR-FTIR Spectrum

In Figure 2.1, the ATR-FTIR spectrum of sulfate adsorbed at the α-Fe_2O_3-H_2O interface is shown (IR-active vibrational modes of sulfate are observed between approximately 1350 – 900 cm^{-1}). ATR-FTIR spectra collected before maximum surface loading (not shown) exhibited differences in the absorbance intensity of the sulfate IR-active vibrational modes, but their relative positions were not significantly affected. The peak maxima identified in the ISDS (Figure 2.1) are listed in Table 2.1. After maximum surface loading was achieved, DI H_2O adjusted to pH 4 was pumped through the flow-through accessory to remove sulfate remaining in solution.

Relative to the vibrational mode at approximately 1008 cm^{-1}, the other sulfate vibrational modes, measured at approximately 1130, 1055, and 976 cm^{-1}, had comparatively larger absorbance intensities (Table 2.1, Figure 2.1). To tentatively determine whether the vibrational mode at approximately 1008 cm^{-1} was real, a non-linear peak fit was performed on the ATR-FTIR spectrum (initial peak positions estimated from the ISDS were used as input values). In Figure 2.2, the non-linear peak-fitted ATR-FTIR spectrum is shown, and the corresponding peak maxima are listed in Table 2.1. The non-linear peak-fitted sulfate vibrational modes (Gaussian peak maxima) were relatively similar to those estimated by the ISDS (mean difference ≈ 8 cm^{-1}). Due to the imprecision of estimating peak maxima from either an ISDS or a non-linear peak fit, a mean difference of approximately 8 cm^{-1} was probably insignificant. A non-linear peak fit was also performed with only three Gaussian functions, which resulted in a significant reduction to the overall fit quality ($r^2 \approx 0.8$, data not shown). Therefore, at maximum surface loading, four vibrational modes were tentatively identified for sulfate adsorbed at the α-Fe_2O_3-H_2O interface. It should be noted, however, that the lowest intensity sulfate vibrational mode did exhibit significant variability, with respect to the other vibrational modes (Table 2.1).

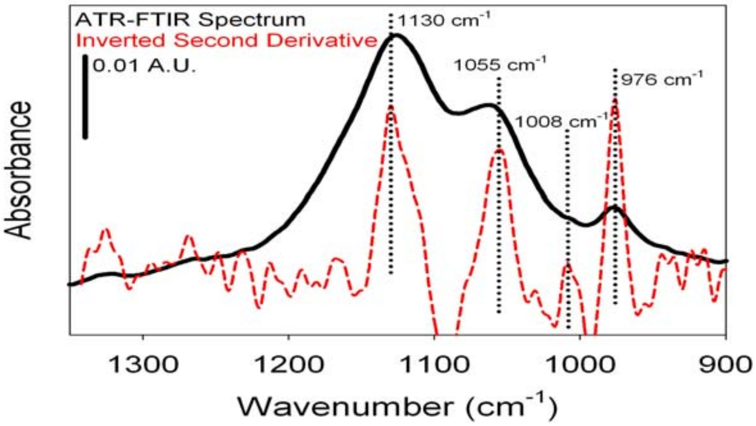

Figure 2.1 ATR-FTIR spectrum of the S-O stretching region for sulfate adsorbed at the α-Fe_2O_3-H_2O interface (pH 4.0). Solid black line corresponds to the ATR-FTIR spectrum. Red dotted line corresponds to the ISDS.

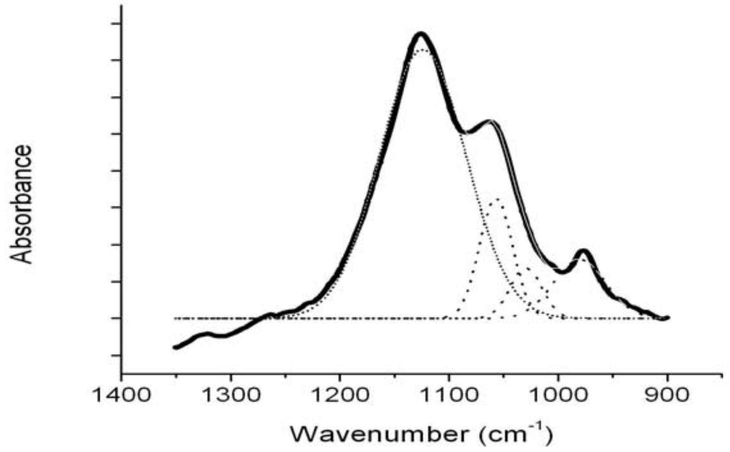

Figure 2.2 Baseline-corrected ATR-FTIR spectrum of the S-O stretching region for sulfate adsorbed at the α-Fe_2O_3-H_2O interface (pH 4.0). Solid black line corresponds to the baseline-corrected ATR-FTIR spectrum. Thin dotted lines are Gaussian functions used to fit the overlapping IR-active vibrational modes.

Table 2.1 Experimental ATR-FTIR vibrational modes (cm^{-1}) of sulfate adsorbed at the α-Fe_2O_3-H_2O interface (pH 4.0), determined by the ISDS (Figure 2.1) and non-linear peak fitting with Gaussian or Lorentzian (in parentheses) functions (Figure 2.2).

Inverse Second Derivative Spectrum	**Non-linear Peak Fit (r^2=0.99)**
1130	1124 (1128)
1055	1057 (1060)
1008	1029 (1040)
976	980 (974)

2.4.2 DFT Frequency Calculations

The DFT-predicted IR vibrational frequencies corresponding to the geometry-optimized sulfate and bisulfate cluster models (Figure 2.3) are listed in Table 2.2. For each system, all of the calculated IR vibrational frequencies were real (i.e., no imaginary frequencies). Therefore, the geometry-optimized cluster models corresponded to local potential energy minima. Based upon the predicted IR vibrational frequencies, the sulfate and bisulfate cluster models were readily distinguishable, thus facilitating their comparison to experimental measurements. It should be noted, however, that the bidentate bridging and monodentate sulfate and bisulfate cluster models, respectively, were predicted to have the same number of IR vibrational frequencies with relatively similar energies (Table 2.2). The mean difference between the predicted IR vibrational frequencies for the bidentate bridging and monodentate sulfate cluster models was approximately 16 cm^{-1}. Likewise, the mean difference between the predicted IR vibrational frequencies for the bidentate bridging and monodentate bisulfate cluster models was only 7 cm^{-1}. As a result, distinguishing between bidentate bridging and monodentate (bi)sulfate, based solely upon the DFT-predicted IR vibrational frequencies, was probably not feasible.

Table 2.2 UB3LYP/6-31+G(d) predicted IR-active vibrational frequencies (cm^{-1}) of the geometry-optimized cluster models (Figure 2.3). Intensities are provided in parentheses.

Sulfate			Bisulfate	
BB	**M**	**H-bonded**	**BB**	**M**
			1236 (347)	1229 (262)
1143 (468)	1139 (338)	1157 (336)	1152 (317)	1158 (423)
			1119 (243)	1131 (219)
1070 (423)	1043 (426)	1060 (376)		
1032 (183)	1006 (245)	976 (451)	1012 (266)	1009 (206)
937 (45)	942 (171)			
		900 (248)		

BB, bidentate bridging; M, monodentate.

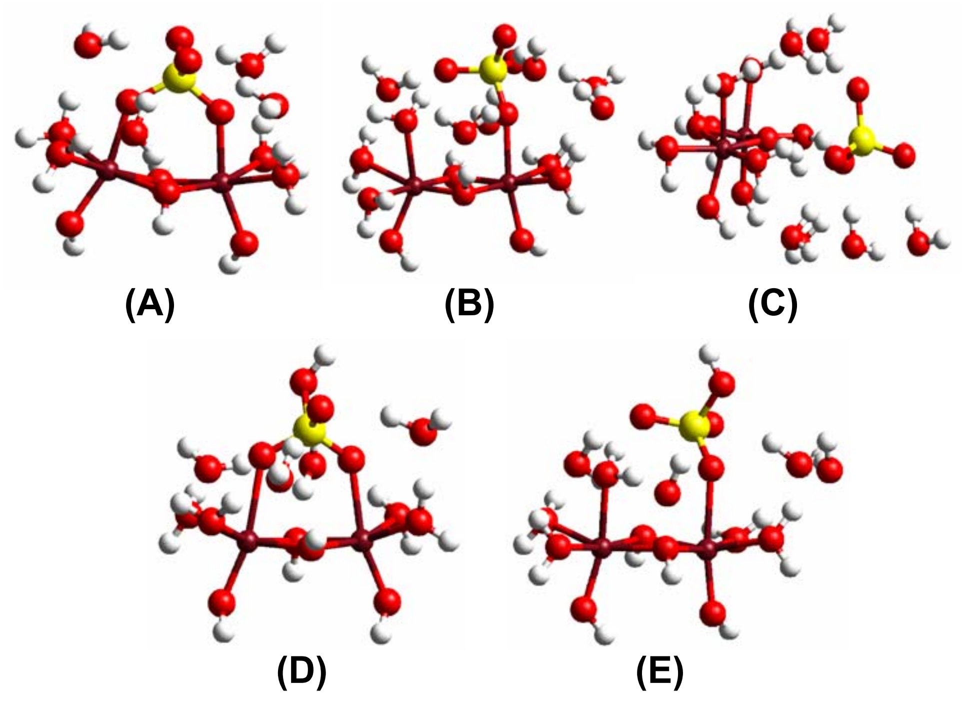

Figure 2.3 Geometry-optimized sulfate and bisulfate cluster models: (A) bidentate bridging sulfate; (B) monodentate sulfate; (C) H-bonded sulfate; (D) bidentate bridging bisulfate; (E) monodentate bisulfate. Red, oxygen; white, hydrogen; yellow, sulfur; and brown, iron.

A test of the effect of basis set size on the DFT-predicted IR vibrational frequencies was performed. Specifically, the bidentate bridging sulfate and bisulfate cluster models were geometry optimized with the UB3LYP/6-311+G(d,p) method (geometry optimizations had been previously performed with the UB3LYP/6-31+G(d) method, Table 2.2). Table 2.3 lists the DFT-predicted IR vibrational frequencies corresponding to the bidentate bridging cluster models optimized with the UB3LYP/6-311+G(d,p) method. A comparison of the IR vibrational frequencies calculated with the UB3LYP/6-31+G(d) and UB3LYP/6-311+G(d,p) methods (Tables 2.2 and 2.3, respectively) shows that the predicted frequency shifts were minor (mean difference of 9 and 7 cm^{-1} for the bidentate bridging sulfate and bisulfate cluster models, respectively). Therefore, a reduction in computational cost was satisfactorily achieved, without sacrificing the accuracy of DFT-predicted IR vibrational frequencies (recall that the maximum experimental resolution was only 8 cm^{-1}).

Table 2.3 UB3LYP/6-311+G(d,p) predicted IR-active vibrational frequencies (cm^{-1}) of the geometry-optimized bidentate bridging cluster models. Intensities are provided in parentheses.

Bidentate Bridging Sulfate	Bidentate Bridging Bisulfate
	1227 (394)
1137 (484)	1143 (400)
	1111 (168)
1067 (560)	
1013 (416)	1014 (227)
945 (52)	

The bidentate bridging sulfate cluster model was also used to test the effect of solvation on the DFT-predicted IR vibrational frequencies. In the first test, the number of explicit H_2O molecules was doubled from four to eight. A comparison of the IR vibrational frequencies calculated with four (Table 2.2) and eight (Table 2.4) explicit H_2O molecules shows that the predicted frequency shifts were minor (mean difference of 13 cm^{-1}). Although the number of H-bonds formed between the sulfate complex and the explicit H_2O molecules increased, the DFT-predicted IR vibrational frequencies were not significantly affected. Therefore, with respect to the sulfate IR vibrational frequencies, including four explicit H_2O molecules in the bidentate bridging cluster model was probably sufficient to simulate conditions at the Fe-(hydr)oxide-H_2O interface.

In the second test, solvation was modeled both explicitly (four explicit H_2O molecules) and implicitly, using the Integral Equation Formalism Polarized Continuum Model (IEFPCM). This particular calculation was performed with the UPBE0/LanL2DZ//6-311+G(d,p) method. For complete details and references related to this particular DFT calculation, refer to Section 4.3.1 of Chapter 4. When the bidentate bridging sulfate cluster model was geometry-optimized with both explicit and implicit solvation, the predicted ν_1 vibrational frequency was significantly closer to the experimental value of approximately 980 cm^{-1} (see Discussion in Section 2.5). However, the two lowest energy ν_3 vibrational frequencies significantly overestimated the experimental values (see Discussion in Section 2.5). It should be noted, however, that the UPBE0/LanL2DZ//6-311+G(d,p) calculation also differed with respect to the exchange-correlation functional (E_{xc}) and basis set used in this study. Therefore, it is unknown whether differences in the DFT-predicted energies of the ν_1 and ν_3 vibrational frequencies resulted from the solvation method, E_{xc}, and/or basis set.

Table 2.4 UB3LYP/6-31+G(d) predicted IR-active vibrational frequencies (cm^{-1}) of the geometry-optimized bidentate bridging sulfate cluster model, using 8 explicit H_2O molecules. UPBE0/LanL2DZ//6-311+G(d,p) IR-active predicted vibrational frequencies (cm^{-1}) of the geometry-optimized bidentate bridging sulfate cluster model, using 4 explicit H_2O molecules and the IEFPCM implicit solvation method (see Section 4.3.1). Intensities are provided in parentheses.

8 Explicit H_2O Molecules	4 Explicit H_2O Molecules + IEFPCM
1120 (421)	1118 (751)
1057 (293)	1088 (1042)
1040 (513)	1069 (528)
931 (28)	979 (52)

2.5 Discussion

Hug [10] used ATR-FTIR spectroscopy to investigate the adsorption of sulfate on α-Fe_2O_3 (pertinent data are listed in Table 2.5). At pH 3 and 4, Hug [10] proposed that sulfate formed a monodentate complex at the α-Fe_2O_3-H_2O interface. A monodentate sulfate complex was proposed because three dominant IR-active vibrational modes were observed (i.e., C_{3v} point group). The DFT calculation of monodentate sulfate shows that four IR-active vibrational frequencies were predicted (Table 2.2). The predicted IR-active vibrational frequencies at 1139, 1043, and 1006

cm^{-1} corresponded to the ν_3 vibrational modes. The IR-active vibrational frequency predicted at 942 cm^{-1} corresponded to the ν_1 vibrational mode. Interestingly, the static DFT calculation of monodentate sulfate predicted that all three ν_3 vibrational frequencies were IR-active. In other words, this particular monodentate sulfate cluster model cannot be rigorously described by C_{3v} point group symmetry. Excluding the predicted ν_3 vibrational frequency at 1006 cm^{-1}, the DFT-predicted IR vibrational frequencies (Table 2.2) for monodentate sulfate compared reasonably well to Hug's *in situ* ATR-FTIR measurements (Table 2.5). One exception was that the predicted ν_1 vibrational frequency at 942 cm^{-1} underestimated the IR-active ν_1 vibrational mode by 33 cm^{-1}.

Table 2.5 Experimental ATR-FTIR vibrational modes (cm^{-1}) of sulfate adsorbed on α-Fe_2O_3 previously published by Hug [10].

100 µM, pH 3	20 µM, pH 4	Dry
		1200
1130	1128	1131
1052	1057	1057
975	975	975

In this study, four IR-active vibrational modes were tentatively identified for sulfate adsorbed at the α-Fe_2O_3-H_2O interface (Table 2.1). Similar to monodentate sulfate, the DFT-predicted IR-active vibrational frequencies for bidentate bridging sulfate at 1143, 1070, and 1032 cm^{-1} corresponded to the ν_3 vibrational modes. The predicted IR-active vibrational frequency at 937 cm^{-1} corresponded to the ν_1

vibrational mode (Table 2.2). The *in situ* ATR-FTIR vibrational modes measured at pH 4 (Table 2.1) compared reasonably well to the DFT-predicted IR-active vibrational frequencies for bidentate bridging and monodentate sulfate. Yet again, however, the ν_1 vibrational mode was significantly underestimated. Interestingly, if the bidentate bridging sulfate cluster was geometry optimized with the IEFPCM method (Table 2.4), then the predicted ν_1 vibrational frequency at 979 cm^{-1} was in much better agreement with experiment (Table 2.1). However, the predicted ν_3 vibrational frequencies at 1088 and 1069 cm^{-1} (Table 2.4) overestimated the IR-active ν_3 vibrational modes by at least 30 cm^{-1}. Therefore, whether the IR-active vibrational frequencies were predicted in the gas (Table 2.1) or aqueous (Table 2.4) phase, one or two of the frequencies were in disagreement with experiment by at least 30 cm^{-1}.

Another potential adsorption complex that may be present under typical experimental conditions is H-bonded sulfate. The DFT-predicted IR-active vibrational frequencies for H-bonded sulfate at 1157, 1060, and 976 cm^{-1} corresponded to the ν_3 vibrational modes. The DFT-predicted IR-active vibrational frequency at 900 cm^{-1} corresponded to the ν_1 vibrational mode (Table 2.2). In comparison with the *in situ* ATR-FTIR vibrational modes (Tables 2.1 and 2.5), the lowest energy ν_3 and ν_1 vibrational frequencies (Table 2.2) grossly underestimated their corresponding IR-active vibrational modes. Therefore, a bidentate bridging or monodentate sulfate complex probably better describes the experimental data.

The ATR-FTIR data presented in this study (Table 2.1) and published by Hug [10] (Table 2.5) differed with respect to the number of sulfate IR-active vibrational modes observed. This discrepancy can be rationalized by one of the following possibilities. First, an IR-active vibrational mode between 1000 –1040 cm^{-1} was not accounted for by Hug. Second, the binding geometry of sulfate at the α-Fe_2O_3-H_2O interface may be influenced by the surface loading. Below maximum surface loading, for example in Hug's study, monodentate sulfate may be energetically favored. The influence of surface loading on sulfate adsorption has not been determined. Third, the low intensity peak tentatively identified in this study between 1000 –1040 cm^{-1} was not an IR-active vibrational mode of sulfate. Unfortunately, it remains challenging to distinguish between monodentate and bidentate bridging sulfate complexes with the ATR-FTIR method, particularly when the IR-active vibrational modes are broad and overlapping. Regardless of the resolution of ATR-FTIR spectra, however, the DFT-predicted IR-active vibrational frequencies of bidentate bridging and monodentate sulfate were nearly indistinguishable (Table 2.2).

Sample drying significantly affects the adsorption of sulfate, which is evident from the diagnostic IR-active vibrational mode ≥ 1200 cm^{-1} [10]. Hug [10] hypothesized that the IR-active vibrational mode ≥ 1200 cm^{-1} corresponded to a change of sulfate coordination or speciation. A change of sulfate coordination, from a monodentate to bidentate bridging complex, or vice-versa, was unlikely. Based upon the DFT calculations, neither the bidentate bridging nor monodentate sulfate complex was predicted to have an IR-active vibrational frequency ≥ 1200 cm^{-1} (Table 2.2). However, a speciation change is plausible. Both the bidentate bridging and monodentate bisulfate complexes were predicted to have an IR-active vibrational frequency ≥ 1200 cm^{-1}, in excellent agreement with experiment (Table 2.5). The predicted IR-active vibrational frequency ≥ 1200 cm^{-1} corresponded to an S-OH stretching mode. Note that the IR-active vibrational modes < 1200 cm^{-1} (Table 2.5) maintained their positions with respect to the pH 3 and 4 *in situ* experiments, suggesting that some sulfate remains after drying. Furthermore, neither the bidentate bridging nor monodentate bisulfate complexes were predicted to have ν_1 vibrational frequencies close to 980 cm^{-1} (i.e., ν_1 vibrational frequency of sulfate).

In Figure 2.4, two potential H^+ transfer mechanisms are proposed that could describe the formation of bisulfate on α-Fe_2O_3. In the first mechanism, Figure 2.4(A), dehydration induces an H^+ transfer from a singly coordinated OH_2 functional group to a monodentate sulfate complex occupying an adjacent surface site. This mechanism is similar to the Mortland and Raman [1] model, whereby dehydration polarizes OH_2 functional groups and enhances their H^+ donating ability. The energy barrier for this particular H^+ transfer is probably low because the OH_2 functional group and monodentate sulfate complex are H-bonded. In the second mechanism, Figure 2.4(B), an H^+ transfer occurs from an H_3O^+ ion in solution to a monodentate sulfate complex. Between pH 3 – 5, dehydration may result in an increased interaction of

H_3O^+ ions with inner-sphere sulfate complexes. An inner-sphere sulfate complex may subsequently become protonated by interacting with an H_3O^+ ion.

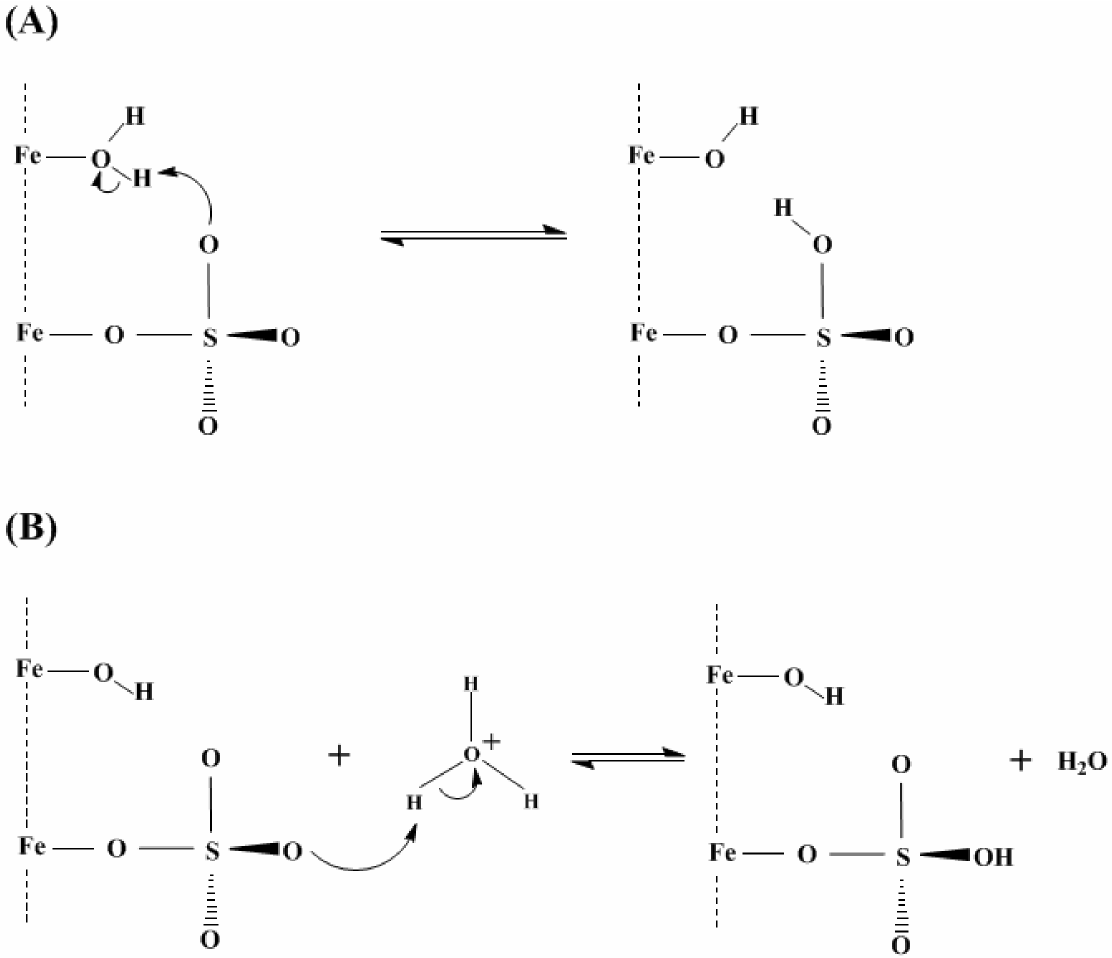

Figure 2.4 Potential H^+ transfer mechanisms that could describe the formation of bisulfate on α-Fe_2O_3 as a function of dehydration. (A) H^+ transfer from a singly coordinated OH_2 functional group to an adjacent monodentate sulfate complex. (B) H^+ transfer from an H_3O^+ ion in solution to a monodentate sulfate complex.

The static DFT calculations performed with the edge-sharing dioctahedral Fe^{3+} cluster models (Figure 2.3) provided evidence that dehydration results in bisulfate formation. Unfortunately, the dynamics of the speciation change (e.g. H^+ transfer reactions) could not be effectively studied with the use of static DFT calculations. To qualitatively determine whether a speciation change resulting from dehydration could be reversible, a 12 ps QMD simulation (*NVT* ensemble) was performed for a monodentate bisulfate complex at the (101) α-FeOOH-H_2O interface. Figure 2.5 displays three snapshots from the QMD simulation at 0, 50, and 800 fs. Within 50 fs, the monodentate HSO_4^- complex transferred its proton (blue H atom displayed in Figure 2.5(A)) to a nearby H_2O molecule (Figure 2.5(B)). A subsequent H^+ transfer rapidly occurred from the previously formed H_3O^+ molecule (Figure 2.5(B)) to another H_2O molecule (Figure 2.5(C)). The H_3O^+ molecule displayed in Figure 2.5(C) briefly interacted with the monodentate SO_4^{2-} complex at the (101) α-FeOOH-H_2O interface, via H-bonding.

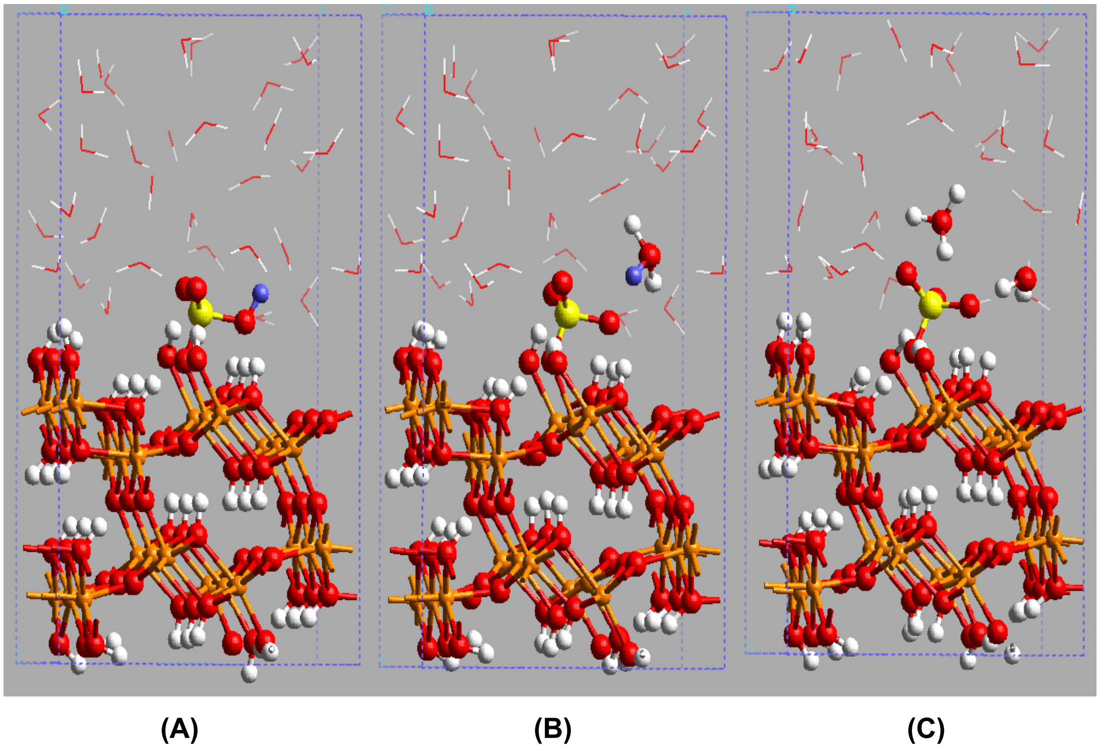

Figure 2.5 Snapshots from the QMD simulation of monodentate HSO_4^- at the (101) α-FeOOH-H_2O interface: (A) starting configuration; (B) 50 fs; (C) 800 fs. Blue H atom highlights the initial H^+ transfer from monodentate HSO_4^- to a nearby H_2O molecule. Red, oxygen; white, hydrogen; yellow, sulfur; and orange, iron.

After the QMD simulation had proceeded for approximately 1.2 ps, another H^+ transfer occurred from an H_3O^+ molecule to a singly coordinated OH functional group adjacent to the monodentate SO_4^{2-} complex. Figure 2.6 displays two additional snapshots from the QMD simulation at 3 and 10 ps. The blue H atom in Figure 2.6(A) highlights the H^+ transfer that occurred from the H_3O^+ molecule to the OH functional group adjacent to monodentate SO_4^{2-}.

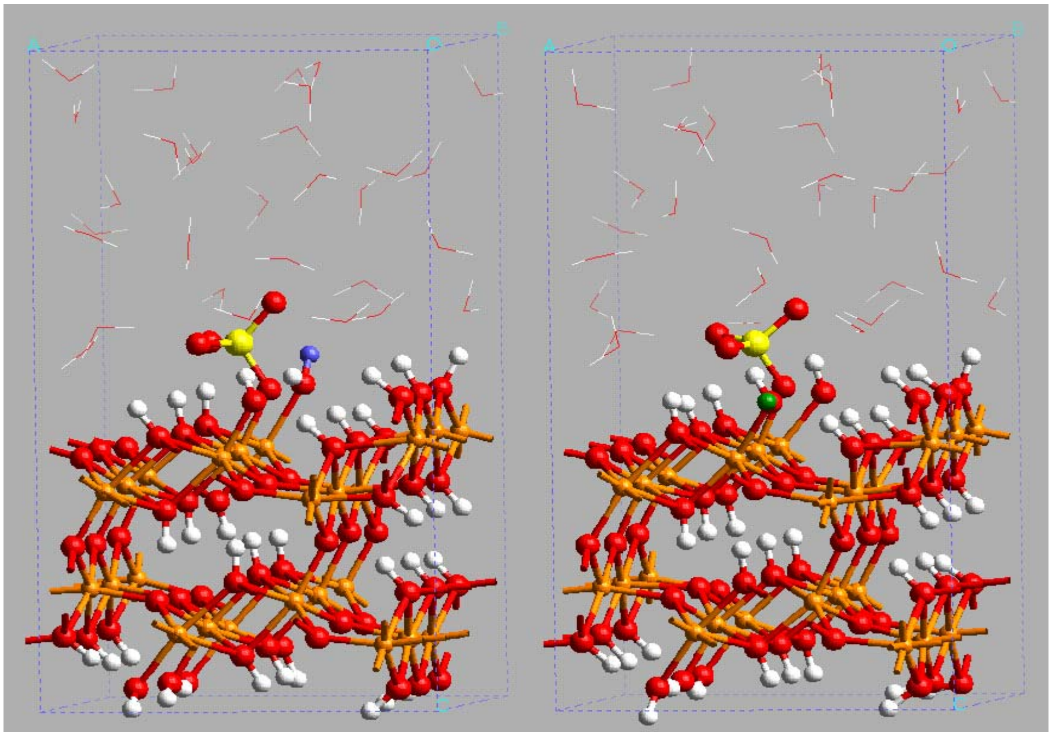

(A) (B)

Figure 2.6 Snapshots from the QMD simulation of monodentate HSO_4^- at the (101) α-FeOOH-H_2O interface: (A) 3 ps; (B) 10 ps. Blue H atom highlights H^+ transfer from an H_3O^+ molecule to an OH functional group adjacent to monodentate SO_4^{2-}. Green H atom highlights interaction between adjacent OH and OH_2 functional groups. Red, oxygen; white, hydrogen; yellow, sulfur; and orange, iron.

The OH_2 functional group highlighted in Figure 2.6(A) remained relatively stable for approximately 2 ps. The dynamics of the O-H bond distance corresponding to the blue H atom bonded to the OH_2 functional group are shown by the blue line in Figure 2.7. Between approximately 1.2 – 3.2 ps, two transient H^+ transfers occurred at approximately 1.5 and 2.7 ps, which involved a nearby H_2O molecule. After approximately 3.2 ps, however, the OH_2 functional group began to interact with a neighboring OH functional group (via the periodic image of the simulation cell). The 10 ps snapshot displayed in Figure 2.6(B) corresponds to a configuration in which the H^+ was transferred from the OH_2 functional group to the OH functional group (highlighted by the green H atom). The dynamics of the O-H bond distance corresponding to the green H atom bonded to the OH_2 functional group are shown by the green line in Figure 2.7. Note from Figure 2.7 that the H^+ hopped between these two OH functional groups throughout the remainder of the QMD simulation (i.e., H^+ transfers correspond to intersecting vertical lines).

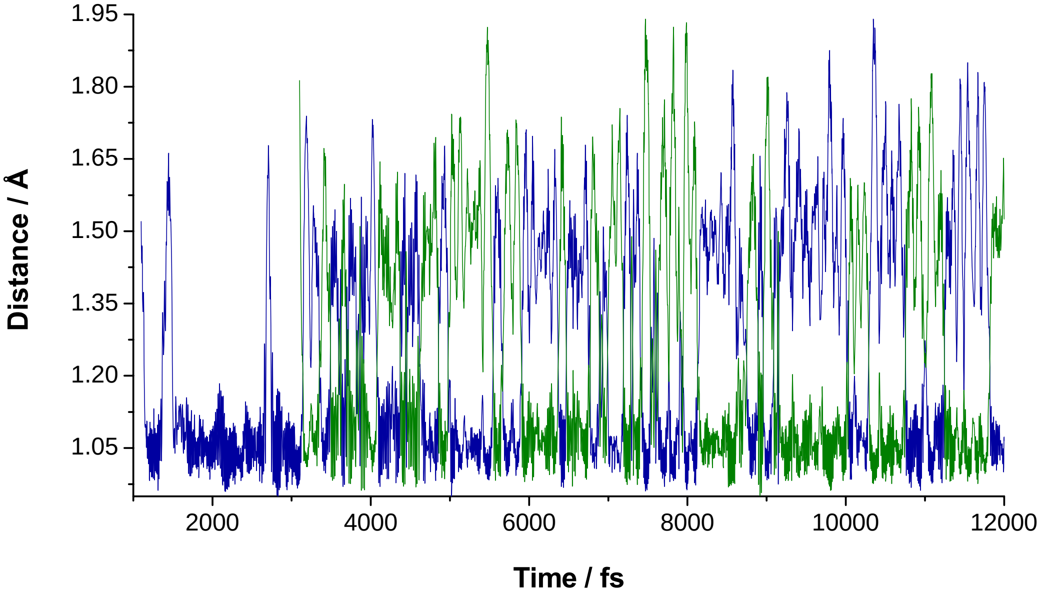

Figure 2.7 Dynamics of the O-H bond distances highlighted in Figure 2.6. The blue line corresponds to the blue H atom bonded to the OH_2 functional group displayed in Figure 2.6(A). The green line corresponds to the green H atom bonded to the OH_2 functional group displayed in Figure 2.6(B).

The principal objective of performing the QMD simulation was to qualitatively determine if a bisulfate complex would be stable under hydrated conditions (i.e., test the reversibility of a speciation change). After the initial H^+ transfer had occurred from the monodentate HSO_4^- complex to a nearby H_2O molecule, a subsequent H^+ transfer back to monodentate SO_4^{2-} did not occur. A QMD simulation of a monodentate SO_4^{2-} complex at the (101) α-FeOOH-H_2O interface was performed for 23.5 ps and is discussed in Chapter 5. At no point during the QMD simulation did monodentate SO_4^{2-} accept a proton. Thus, the QMD simulation performed in this study for monodentate HSO_4^- was terminated after 12 ps. Most importantly, the QMD simulation provided qualitative evidence that bisulfate was not stable under hydrated conditions. In other words, a speciation change resulting from dehydration is probably reversible as a function of rehydration. It is important to note, however, that the rate of monodentate HSO_4^- deprotonation could be strongly influenced by the pH and salt concentration of the solvent.

Before the use of *in situ* ATR-FTIR spectroscopy, several *ex situ* sulfate adsorption studies were performed with a variety of Fe-(hydr)oxide minerals, using transmission and diffuse-reflectance IR spectroscopy [5-8, 30]. In Table 2.6, selected results from studies performed by Turner and Kramer [8] and Persson and Lovgren [30] are shown. Turner and Kramer [8] proposed that sulfate formed a bidentate bridging complex on α-Fe_2O_3 (i.e., C_{2v} point group). However, the IR-active vibrational mode measured at 1255 cm^{-1} (Table 2.6) does not correspond to a DFT-predicted IR-active vibrational frequency for one of the sulfate cluster models (Table 2.2). The results from Turner and Kramer's study [8] were qualitatively similar to the *ex situ* results reported by Hug [10] (Table 2.5), in which an IR-active vibrational mode ≥ 1200 cm^{-1} was measured. Based upon the DFT calculations, the IR-active vibrational mode > 1200 cm^{-1} probably corresponded to a bisulfate complex that formed because of sample drying prior to the IR measurement (Table 2.2).

Table 2.6 Experimental IR vibrational modes (cm^{-1}) of sulfate adsorbed on α-Fe_2O_3[a] and α-FeOOH[b].

α-Fe_2O_3	**α-FeOOH**
1255	1250
1130	1130
1030	1050
950	980

[a]Turner and Kramer [8]. [b]Persson and Lovgren [30].

Persson and Lovgren [30] proposed that sulfate formed an outer-sphere complex on α-FeOOH. The IR-active vibrational modes measured by Persson and Lovgren [30] were similar to those measured by Turner and Kramer [8] (Table 2.6), qualitatively suggesting that similar adsorption complexes had formed on dried α-FeOOH and α-Fe_2O_3 samples. Persson and Lovgren [30] also suggested that a component of protonated sulfate (i.e., bisulfate) had formed on goethite below pH 5, in excellent agreement with the DFT predictions for the bidentate bridging and monodentate bisulfate complexes (Table 2.2).

Parfitt and Smart [6] investigated the adsorption of sulfate on several air-dried and evacuated Fe-(hydr)oxide minerals and proposed that sulfate formed a bidentate bridging complex (Table 2.7). Upon evacuation, the IR-active vibrational modes exhibited relatively minor shifts (mean differences for the individual samples were 14 – 20 cm^{-1}, with the exception of α-FeOOH). When compared to the DFT-predicted IR-active vibrational frequencies (Table 2.2), bisulfate (and sulfate) probably formed under their experimental conditions (i.e., IR-active vibrational mode ≥ 1200 cm^{-1}), similar to the results published by Turner and Kramer [8], Hug [10], and Persson and Lovgen [30]. It should be noted that the formation of bisulfate was apparently independent of the type of Fe-(hydr)oxide mineral (Table 2.7). To be brief, *ex situ* IR spectroscopic measurements provide clear evidence that bisulfate forms on Fe-(hydr)oxide minerals as a result of dehydration.

Table 2.7 Experimental IR vibrational modes (cm^{-1}) of sulfate adsorbed on α-Fe_2O_3, α-FeOOH, akaganeite (β-FeOOH), and lepidocrocite (γ-FeOOH)[a]. Values correspond to air-dried and evacuated (in parentheses) samples.

α-Fe_2O_3	**α-FeOOH**	**β-FeOOH**	**γ-FeOOH**
1200 (1245)	1254 (1282)	1200 (1215)	1250 (1275)
1128 (1131)	1141 (1150)	1120 (1123)	1133 (1140)
1040 (1030)	1040 (955)	1060 (1035)	* *
970 (950)	965 (909)	970 (950)	965 (955)

[a]Parfitt and Smart [6]. *Reported as obscured.

2.6 Conclusions

In this study, DFT calculations were performed to investigate the effect of hydration on sulfate adsorption and speciation at the Fe-(hydr)oxide-H_2O interface. Though this study did not unequivocally elucidate the effect of hydration on sulfate adsorption and speciation, DFT frequency calculations and a QMD simulation proved valuable. The DFT frequency calculations suggest that sulfate forms a bidentate bridging or monodentate complex at the Fe-(hydr)oxide-H_2O interface. Furthermore, the DFT frequency calculations provide evidence that dehydration results in the formation of bisulfate (i.e., a speciation change). A QMD simulation of a monodentate bisulfate complex at the (101) α-FeOOH-H_2O interface, however, suggests that a speciation change is probably reversible as a function of rehydration.

The DFT-predicted IR-active vibrational frequencies were compared to several previously published experimental IR studies. In previous studies, the IR-active vibrational modes of sulfate were assigned from a point group symmetry analysis. Unfortunately, the point group symmetry analyses were restricted to sulfate complexes, and thus, a speciation change (i.e., formation of bisulfate) resulting from dehydration was overlooked. When point group symmetry analyses are coupled with DFT calculations, however, a more fundamental understanding of the role of hydration on sulfate adsorption is readily achieved.

2.7 References

1. Mortland, M. M.; Raman, K. V., Surface Acidity of Smectites in Relation to Hydration, Exchangeable Cation, and Structure. *Clays and Clay Minerals* **1968,** *16*, (5), 393-398.

2. Bartlett, R.; James, B., Studying Dried, Stored Soil Samples - Some Pitfalls. *Soil Science Society of America Journal* **1980,** *44*, (4), 721-724.

3. Ross, D. S.; Hales, H. C.; Shea-McCarthy, G. C.; Lanzirotti, A., Sensitivity of Soil Manganese Oxides: Drying and Storage Cause Reduction. *Soil Science Society of America Journal* **2001,** *65*, (3), 736-743.

4. Kennedy, C.; Smith, D. S.; Warren, L. A., Surface Chemistry and Relative Ni Sorptive Capacities of Synthetic Hydrous Mn Oxyhydroxides Under Variable Wetting and Drying Regimes. *Geochimica Et Cosmochimica Acta* **2004,** *68*, (3), 443-454.

5. Parfitt, R. L.; Smart, R. S. C., Infrared Spectra from Binuclear Bridging Complexes of Sulfate Adsorbed on Goethite (α-FeOOH). *Journal of the Chemical Society-Faraday Transactions I* **1977,** *73*, 796-802.

6. Parfitt, R. L.; Smart, R. S. C., The Mechanism of Sulfate Adsorption on Iron Oxides. *Soil Science Society of America Journal* **1978,** *42*, (1), 48-50.

7. Harrison, J. B.; Berkheiser, V. E., Anion Interactions with Freshly Prepared Hydrous Iron Oxides. *Clays and Clay Minerals* **1982,** *30*, (2), 97-102.

8. Turner, L. J.; Kramer, J. R., Sulfate Ion Binding on Goethite and Hematite. *Soil Science* **1991,** *152*, (3), 226-230.

9. Peak, D.; Ford, R. G.; Sparks, D. L., An *In Situ* ATR-FTIR Investigation of Sulfate Bonding Mechanisms on Goethite. *Journal of Colloid and Interface Science* **1999,** *218*, (1), 289-299.

10. Hug, S. J., *In Situ* Fourier Transform Infrared Measurements of Sulfate Adsorption on Hematite in Aqueous Solutions. *Journal of Colloid and Interface Science* **1997,** *188*, (2), 415-422.

11. Wijnja, H.; Schulthess, C. P., Vibrational Spectroscopy Study of Selenate and Sulfate Adsorption Mechanisms on Fe and Al (hydr)oxide Surfaces. *Journal of Colloid and Interface Science* **2000,** *229*, (1), 286-297.

12. Baltrusaitis, J.; Jensen, J. H.; Grassian, V. H., FTIR Spectroscopy Combined with Isotope Labeling and Quantum Chemical Calculations to Investigate Adsorbed Bicarbonate Formation Following Reaction of Carbon Dioxide with Surface Hydroxyl Groups on Fe_2O_3 and Al_2O_3. *Journal of Physical Chemistry B* **2006,** *110*, (24), 12005-12016.

13. Bargar, J. R.; Kubicki, J. D.; Reitmeyer, R.; Davis, J. A., ATR-FTIR Spectroscopic Characterization of Coexisting Carbonate Surface Complexes on Hematite. *Geochimica Et Cosmochimica Acta* **2005,** *69*, (6), 1527-1542.

14. Kwon, K. D.; Kubicki, J. D., Molecular Orbital Theory Study on Surface Complex Structures of Phosphates to Iron Hydroxides: Calculation of Vibrational Frequencies and Adsorption Energies. *Langmuir* **2004,** *20*, (21), 9249-9254.

15. Omoike, A.; Chorover, J.; Kwon, K. D.; Kubicki, J. D., Adhesion of Bacterial Exopolymers to α-FeOOH: Inner-Sphere Complexation of Phosphodiester Groups. *Langmuir* **2004,** *20*, (25), 11108-11114.

16. Tribe, L.; Kwon, K. D.; Trout, C. C.; Kubicki, J. D., Molecular Orbital Theory Study on Surface Complex Structures of Glyphosate on Goethite: Calculation of Vibrational Frequencies. *Environmental Science and Technology* **2006,** *40*, (12), 3836-3841.

17. Schwertmann, U.; Cornell, R. M., *Iron Oxides in the Laboratory: Preparation and Characterization*. VCH: Weinheim; New York, 1991.

18. Sainz-Diaz, C. I.; Timon, V.; Botella, V.; Hernandez-Laguna, A., Isomorphous Substitution Effect on the Vibration Frequencies of Hydroxyl Groups in Molecular Cluster Models of the Clay Octahedral Sheet. *American Mineralogist* **2000,** *85*, (7-8), 1038-1045.

19. Sposito, G., On Points of Zero Charge. *Environmental Science and Technology* **1998,** *32*, (19), 2815-2819.

20. Myneni, S. C. B.; Traina, S. J.; Waychunas, G. A.; Logan, T. J., Experimental and Theoretical Vibrational Spectroscopic Evaluation of Arsenate Coordination in Aqueous Solutions, Solids, and at Mineral-Water Interfaces. *Geochimica Et Cosmochimica Acta* **1998,** *62*, (19-20), 3285-3300.

21. Ladeira, A. C. Q.; Ciminelli, V. S. T.; Duarte, H. A.; Alves, M. C. M.; Ramos, A. Y., Mechanism of Anion Retention from EXAFS and Density Functional

Calculations: Arsenic (V) Adsorbed on Gibbsite. *Geochimica Et Cosmochimica Acta* **2001,** *65*, (8), 1211-1217.

22. Sherman, D. M.; Randall, S. R., Surface Complexation of Arsenic (V) to Iron (III) (hydr)oxides: Structural Mechanism from *Ab Initio* Molecular Geometries and EXAFS Spectroscopy. *Geochimica Et Cosmochimica Acta* **2003,** *67*, (22), 4223-4230.

23. Zhang, N. L.; Blowers, P.; Farrell, J., Evaluation of Density Functional Theory Methods for Studying Chemisorption of Arsenite on Ferric Hydroxides. *Environmental Science and Technology* **2005,** *39*, (13), 4816-4822.

24. Persson, P.; Axe, K., Adsorption of Oxalate and Malonate at the Water-Goethite Interface: Molecular Surface Speciation from IR Spectroscopy. *Geochimica Et Cosmochimica Acta* **2005,** *69*, (3), 541-552.

25. Yoon, T. H.; Johnson, S. B.; Musgrave, C. B.; Brown, G. E., Adsorption of Organic Matter at Mineral/Water Interfaces: I. ATR-FTIR Spectroscopic and Quantum Chemical Study of Oxalate Adsorbed at Boehmite/Water and Corundum/Water Interfaces. *Geochimica Et Cosmochimica Acta* **2004,** *68*, (22), 4505-4518.

26. Frisch, M. J., Trucks, G. W., Schlegel, H. B., Scuseria, G. E., Robb, M. A., Cheeseman, J. R., Montgomery, Jr., J. A., Vreven, T., Kudin, K. N., Burant, J. C., Millam, J. M., Iyengar, S. S., Tomasi, J., Barone, V., Mennucci, B., Cossi, M., Scalmani, G., Rega, N., Petersson, G. A., Nakatsuji, H., Hada, M., Ehara, M., Toyota, K., Fukuda, R., Hasegawa, J., Ishida, M., Nakajima, T., Honda, Y., Kitao, O., Nakai, H., Klene, M., Li, X., Knox, J. E., Hratchian, H. P., Cross, J. B., Bakken, V., Adamo, C., Jaramillo, J., Gomperts, R., Stratmann, R. E., Yazyev, O., Austin, A. J., Cammi, R., Pomelli, C., Ochterski, J. W., Ayala, P. Y., Morokuma, K., Voth, G. A., Salvador, P., Dannenberg, J. J., Zakrzewski, V. G., Dapprich, S., Daniels, A. D., Strain, M. C., Farkas, O., Malick, D. K., Rabuck, A. D., Raghavachari, K., Foresman, J. B., Ortiz, J. V., Cui, Q., Baboul, A. G., Clifford, S., Cioslowski, J., Stefanov, B. B., Liu, G., Liashenko, A., Piskorz, P., Komaromi, I., Martin, R. L., Fox, D. J., Keith, T., Al-Laham, M. A., Peng, C. Y., Nanayakkara, A., Challacombe, M., Gill, P. M. W., Johnson, B., Chen, W., Wong, M. W., Gonzalez, C., and Pople, J. A. *Gaussian 03, revision B.05; Gaussian, Inc.;*, Wallingford CT, 2004.

27. Stephens, P. J.; Devlin, F. J.; Chabalowski, C. F.; Frisch, M. J., Ab-Initio Calculation of Vibrational Absorption and Circular-Dichroism Spectra Using Density-Functional Force-Fields. *Journal of Physical Chemistry* **1994,** *98*, (45), 11623-11627.

28. Becke, A. D., Density-Functional Thermochemistry 3. The Role of Exact Exchange. *Journal of Chemical Physics* **1993,** *98*, (7), 5648-5652.

29. Lee, C. T.; Yang, W. T.; Parr, R. G., Development of the Colle-Salvetti Correlation-Energy Formula into a Functional of the Electron-Density. *Physical Review B* **1988,** *37*, (2), 785-789.

30. Persson, P.; Lovgren, L., Potentiometric and Spectroscopic Studies of Sulfate Complexation at the Goethite-Water Interface. *Geochimica Et Cosmochimica Acta* **1996,** *60*, (15), 2789-2799.

Chapter 3

SULFATE ADSORPTION AT THE ALUMINUM AND IRON OXIDE-WATER INTERFACE – ESTIMATION OF ADSORPTION ENERGIES

3.1 Abstract

In this study, density functional theory calculations were used to estimate the energies of potential sulfate adsorption pathways at the Al- and Fe-(hydr)oxide-H_2O interface. Variably-charged Al- and Fe-(hydr)oxides were modeled with static configurations of edge-sharing dioctahedral Al^{3+} and Fe^{3+} clusters. The inner-sphere bidentate bridging and monodentate sulfate adsorption pathways were predicted to be exergonic on positively-charged Al^{3+} and Fe^{3+} clusters (-19 to -124 kJ mol^{-1}). However, both the inner-sphere and outer-sphere adsorption pathways were predicted to be endergonic on neutral Al^{3+} and Fe^{3+} clusters (+5 to +61 kJ mol^{-1}). The most exergonic pathways corresponded to bidentate bridging adsorption on the +2 charged Al^{3+} and Fe^{3+} clusters. For pathways involving the +1 charged Al^{3+} cluster, the energies of bidentate bridging and monodentate sulfate adsorption were equivalent. For pathways involving the +1 charged Fe^{3+} cluster, however, the energy of monodentate sulfate adsorption was slightly more exergonic. The predicted energies of bidentate bridging and monodentate sulfate adsorption on the +1 charged Fe^{3+} cluster (i.e., H^+/SO_4^{2-} exchange stoichiometry, χ, equal to 1) qualitatively agreed with published experimental results for sulfate adsorption on goethite (α-FeOOH)

(predicted values -34 and -52 kJ mol^{-1}, respectively, and experimental range -36 to -30 kJ mol^{-1}). This agreement was encouraging, as investigators have reported that χ ranges from approximately 0.98 to 1.28 for sulfate adsorption on α-FeOOH.

3.2 Introduction

The transport and bioavailability of sulfate in soils are significantly affected by adsorption reactions with variably-charged Al- and Fe-(hydr)oxides and 1:1 clay minerals (e.g. kaolinite). Sulfur is an essential plant nutrient, but its availability is dependent upon the adsorption of sulfate by soil minerals (i.e., sulfate is the bioavailable form of S). The transport of sulfate in forest soils has been extensively studied because sulfate leaching can enhance the transport of base cation nutrients. Consequently, sulfate is considered as an indirect conserver of base cations. The leaching of base cations, for example Ca^{2+} and Mg^{2+}, is important in forest soils affected by acid rain because the base cations can be replaced by Al^{3+} [1] (Al^{3+} ions are toxic to many organisms).

The transport and bioavailability of sulfate are also of significance in aquatic systems affected by acid mine drainage (AMD). In AMD, unusually high concentrations of sulfate are commonly measured. In excess of 250 mg L^{-1} sulfate is a potential contaminant [2]. Fortunately, the high concentrations of sulfate can be diminished by sorption with amorphous Fe-(hydr)oxides. However, alkalinity treatment methods (e.g. application of $CaCO_3(s)$) are typically used to precipitate and immobilize toxic metals in AMD. Unfortunately, alkalinity treatment methods can inadvertently enhance the transport of sulfate to aquatic resources [3]. To be brief, therefore, a fundamental understanding of the mechanisms of sulfate sorption is of primary importance in soil and aquatic chemistry.

Sposito [4] has suggested that sulfate exhibits intermediate ligand exchange reactivity, in which it can form both inner-sphere and outer-sphere complexes on variably-charged Al- and Fe-(hydr)oxides. The adsorption of sulfate is influenced, to a varying extent, by pH, ionic strength, hydration, and the structure and composition of mineral surfaces. Numerous studies have used infrared (IR) vibrational spectroscopic methods in an attempt to identify the binding geometries of equilibrium sulfate complexes on hydrated and dehydrated samples of Al- and Fe-(hydr)oxides [5-19]. Unfortunately, interpretations of the experimental results have varied significantly, possibly a reflection of the intermediate ligand exchange reactivity of sulfate. Monodentate, bidentate bridging, and tridentate sulfate complexes have been proposed. Furthermore, experimental results have suggested that inner-sphere and outer-sphere sulfate complexes can coexist, and that sulfate and bisulfate may also coexist under dehydrated conditions.

Although numerous studies have investigated the molecular-scale adsorption of sulfate on variably-charged Al- and Fe-(hydr)oxides [5-19], the mechanisms of sulfate adsorption remain inadequately understood. In particular, the reaction pathways, activation barriers, and potential intermediates of sulfate adsorption have not been fully elucidated. Unfortunately, the initial adsorption of sulfate can reach steady-state rapidly (e.g. < 1ms for biphasic kinetics), sooner than most high-resolution spectroscopic measurements can be performed. To complicate matters, several potential pathways could exist for sulfate adsorption [20]. For example, three pathways have been proposed for bidentate bridging and outer-sphere sulfate adsorption as a function of pH [20]. An understanding of the mechanisms of sulfate adsorption is crucial to the improvement of surface complexation models, which can be used to simulate its transport in soils and aquatic systems.

The principal objective of this study was to use density functional theory (DFT) to estimate the energies of potential sulfate adsorption pathways on variably-charged Al- and Fe-(hydr)oxides. The DFT calculations were performed with static configurations of edge-sharing dioctahedral Al^{3+} and Fe^{3+} clusters. The sulfate adsorption pathways modeled in this study correspond to pathways suggested by previous investigators (e.g. [20]) and were compared to experimental results available in the literature [21]. The ultimate goals of this research endeavor are: (1) predict the activation barriers and rate constants of sulfate adsorption pathways, and (2) predict the energies of competing nutrient adsorption pathways (e.g. sulfate and phosphate) in order to advance our understanding of their equilibrium distribution in soils. DFT predictions of the activation barriers and rate constants would be particularly valuable when experimental measurements may not be feasible.

3.3 Methods

In this study, the energies of several potential bidentate bridging, monodentate, and outer-sphere sulfate adsorption pathways on variably-charged Al- and Fe-(hydr)oxides were estimated with DFT calculations. Recent studies have used similar DFT methods to investigate the adsorption of nutrients and contaminants on Al- and Fe-(hydr)oxide clusters, and successfully compared the DFT predictions with experimental measurements [11, 22-27]. The overall charges of the edge-sharing dioctahedral Al^{3+} and Fe^{3+} reactant clusters ranged from +2 to neutral. As a result, the adsorption of sulfate was modeled for reactions occurring on surfaces at or below their pH_{pzc} (i.e., $pH \leq pH_{pzc}$, where pH_{pzc} is defined as the pH at which the net surface charge density equals zero [28]).

The DFT calculations were performed with Gaussian 03 [29]. In this study, the Becke 3-parameter non-local exchange functional [30, 31] and the gradient-corrected correlation functional of Lee *et al.* [32], denoted B3LYP, were chosen. Unrestricted B3LYP calculations were performed for the cluster models containing Fe atoms. The high-spin state of Fe^{3+} was specified for each Fe atom. Conversely, restricted open-shell B3LYP calculations were performed for the cluster models not containing Fe atoms. The all-electron 6-31+G(d,p) basis set was used for the S, O, and H atoms, while the CEP-121G relativistic effective core potential (RECP) basis set [33] was used for the Fe atoms. For one bidentate bridging sulfate adsorption pathway that involved Fe^{3+} cluster models, a comparison of the RECP and all-electron basis set methods was performed to ensure consistent results (Table 3.6). The use of RECP basis sets in Hartree-Fock calculations of Fe^{3+}-aqua ions was shown to reduce basis set superposition error [34] and reduces the computational workload.

To estimate the energies of the sulfate adsorption pathways, each reactant and product cluster was first geometry-optimized in the gas-phase without symmetry or geometrical constraints. Frequency calculations were subsequently performed to determine whether the geometry optimizations had successfully located potential energy minima (i.e., no imaginary frequencies). It is important to note, however, that only one static configuration was geometry-optimized for each reactant and product cluster. Therefore, the potential energy minima did not likely correspond to the global minima for these configurations. The frequency calculations were also performed to estimate the thermal correction to the Gibbs free energy (scaling not taken into account). The thermal correction to the Gibbs free energy includes the effects of molecular translation, rotation, and vibration at 298.15 K and 1.0 atm., as well as the zero-point vibrational energy [35].

Single-point B3LYP/6-311++G(df,pd) energy calculations were performed for each geometry-optimized gas-phase reactant and product cluster, using the Integral Equation Formalism Polarized Continuum Model (IEFPCM) method [36]. Note that the CEP-121G basis set was used for the Fe atoms. The application of a larger basis set in the single-point IEFPCM energy calculations ensured a more accurate estimation of the reactant and product cluster energies [35]. The single-point

IEFPCM energy calculations provided an estimate of the total free energy in solution, including non-electrostatic terms, for each geometry-optimized reactant and product cluster. The dielectric constant of bulk water ($\varepsilon = 78.4$) was specified in the single-point IEFPCM energy calculations, and therefore both explicit and implicit solvation were considered.

For one bidentate bridging sulfate adsorption pathway, each reactant and product cluster was geometry-optimized with the IEFPCM method (Tables 3.3 and 3.4). The starting configurations for the IEFPCM geometry optimizations corresponded to the energy-minimized gas-phase reactant and product clusters (Table 3.1). The geometry optimizations and frequency calculations were both performed with the IEFPCM method to compare with the corresponding gas-phase prediction and to determine any potential differences. Note that the IEFPCM geometry optimizations were followed by single-point IEFPCM energy calculations (B3LYP/6-311++G(df,pd) method). Although it would have been preferable to perform all of the geometry optimizations and frequency calculations with the IEFPCM method, such a task was computationally prohibitive.

3.4 Results and Discussion

The adsorption of an inner-sphere sulfate complex can be described by a ligand exchange mechanism that involves singly coordinated OH_2 and/or OH functional groups, and is primarily a function of pH and surface charge (i.e., H^+

composition). He *et al.* [20] and Rajan [37], for example, proposed a bidentate bridging ligand exchange mechanism for sulfate adsorption wherein the various pathways are pH-dependent. At low pH, He *et al.* [20] and Rajan [37] proposed that the ligand exchange mechanism for sulfate adsorption involves two singly coordinated OH_2 functional groups. At intermediate pH, the ligand exchange mechanism for sulfate adsorption involves one singly coordinated OH_2 and one OH functional group. Near the pH_{pzc}, the ligand exchange mechanism for sulfate adsorption involves two singly coordinated OH functional groups [20]. In other words, a particular sulfate adsorption pathway is indirectly affected by the solution pH, which directly affects the mineral surface charge.

Sulfate adsorption at the mineral-H_2O interface generally results in an increase in solution pH. An increase in solution pH can be macroscopically described as resulting from the ligand exchange of singly coordinated OH functional groups. However, an increase in solution pH can also result from the coadsorption of H^+ at the mineral surface (i.e., $>FeOH + H_3O^+ \rightarrow >FeOH_2^+ + H_2O$) in conjunction with sulfate adsorption. Experimentally, the increase in solution pH can be measured with a back titration, which determines the mole ratio of OH^- released (and/or H^+ consumed) per molecule of adsorbed SO_4^{2-}. The OH^-/SO_4^{2-} (or H^+/SO_4^{2-}) exchange stoichiometry, designated as χ, ranges from 0 to 2. Unfortunately, a back titration measurement of χ cannot differentiate between exchanged OH functional groups or the coadsorption of H^+ at the mineral surface.

In this study, χ was assumed to be equivalent to the H^+/SO_4^{2-} exchange stoichiometry. In other words, OH^- release was assumed to result from the coadsorption of H^+ at the mineral surface in conjunction with sulfate adsorption (i.e., χ was not defined by the ratio of OH functional groups released per molecule of adsorbed SO_4^{2-}). This assumption of χ is supported by the fact that OH_2 functional groups are substantially better leaving groups than OH functional groups. It is important to note, however, that the experimental definitions of the OH^-/SO_4^{2-} and H^+/SO_4^{2-} exchange stoichiometries may not be entirely separable (e.g. see bidentate bridging adsorption pathways in Tables 3.2 and 3.6 for $\chi = 1$). Furthermore, both definitions of the OH^-/SO_4^{2-} and H^+/SO_4^{2-} exchange stoichiometries neglect the population of OH_2 functional groups that exist at $pH < pH_{pzc}$. In short, therefore, any current definition of χ will inevitably involve some simplifications.

The H^+/SO_4^{2-} definition of χ used in this study is in accordance with recent surface complexation modeling investigations performed by Sverjensky and coworkers [38, 39]. For example, Sverjensky and coworkers [38, 39] represented the adsorption of bidentate bridging sulfate ($\chi = 2$) by the following reaction equation:

$$2{>}FeOH + 2H^+ + SO_4^{2-} \rightarrow ({>}FeO)_2SO_2 + 2H_2O \qquad (1)$$

In this study, the qualitatively equivalent adsorption pathway was represented as:

$$[Fe_2(OH)_4(OH_2)_6\cdot(H_2O)_6]^{2+} + SO_4^{2-}(H_2O)_9 \rightarrow Fe_2(OH)_4(OH_2)_4SO_4\cdot(H_2O)_6 + 1.1(H_2O)_{10} \qquad (2)$$

The reactants 2>FeOH + 2H^+ in equation (1) [38, 39] are equivalent to the $[Fe_2(OH)_4(OH_2)_6{\cdot}(H_2O)_6]^{2+}$ reactant cluster in equation (2), whereby two singly coordinated OH functional groups were protonated resulting in an overall charge of +2. By defining χ to be equivalent to the H^+/SO_4^{2-} stoichiometry, the overall charge of each Al^{3+} and Fe^{3+} reactant cluster was equal to χ (e.g. see Tables 3.2 and 3.6).

Excluding the effects of ionic strength and competing adsorption reactions, the dependence of sulfate adsorption on pH, surface structure, and surface charge alone creates a complex network of potential adsorption pathways. These complexities motivated the current study to explore the application of DFT in estimating the energies of potential sulfate adsorption pathways on variably-charged Al^{3+} and Fe^{3+} clusters. The objective was to compare the energies of potential sulfate adsorption pathways to better understand their relative thermodynamic favorability. The ultimate goal will be to predict the activation barriers and rate constants of the most viable sulfate adsorption pathways. Potential sulfate adsorption pathways involving the variably-charged Al^{3+} reactant clusters will be discussed first.

Table 3.1 lists the DFT-calculated energies for each reactant and product cluster model. The energies corresponding to the potential sulfate adsorption pathways on edge-sharing dioctahedral Al^{3+} cluster models are listed in Table 3.2. Although the DFT calculations described in the Methods included components of the reaction enthalpy and entropy (i.e., terms embedded within the thermal correction to the Gibbs free energy), the configurational entropy was neglected. In particular, only one configuration was geometry-optimized for each reactant and product cluster model. Therefore, conformational analyses of the potential energy surfaces were not performed. As a result, the absolute values of the DFT-calculated energies for the potential sulfate adsorption pathways should be interpreted cautiously as the magnitude of their error is currently unknown. Although these DFT calculations cannot account for pH explicitly, the pH-dependent surface charge can be modeled by adjusting the number of H^+ in the clusters to approximately simulate the surface charge at $pH \leq pH_{pzc}$. In this study, values of χ ranged from 0 – 2 to approximate the range of values that could be measured experimentally [20, 37].

Table 3.1 DFT-calculated energies for each reactant and product cluster contained in the sulfate adsorption pathways listed in Table 3.2. The energies are in Hartrees/molecule.

	E_{Gas}[a]	$E_{Thermal}$[b]	E_{IEFPCM}[c]
Reactants			
$SO_4^{2-}\cdot(H_2O)_9$	-1387.222	0.189	-1387.788
$[Al_2(OH)_4(OH_2)_6\cdot(H_2O)_6]^{2+}$	-1705.496	0.304	-1706.210
$[Al_2(OH)_5(OH_2)_5\cdot(H_2O)_6]^{+}$	-1705.199	0.291	-1705.746
$Al_2(OH)_6(OH_2)_4\cdot(H_2O)_6$	-1704.810	0.288	-1705.295
Products			
$(H_2O)_{10}$	-764.493	0.201	-764.762
$OH^-\cdot(H_2O)_9$	-763.959	0.190	-764.276
$OH^-\cdot(H_2O)_{10}$	-840.413	0.214	-840.751
$(OH^-)_2\cdot(H_2O)_9$	-839.767	0.199	-840.269
Bidentate Bridging Complex			
$Al_2(OH)_4(OH_2)_4SO_4\cdot(H_2O)_6$	-2252.225	0.273	-2252.809
Monodentate Complexes			
$[Al_2(OH)_5(OH_2)_4SO_4\cdot(H_2O)_6]^{-}$[†]	-2328.152	0.286	-2328.798
$[Al_2(OH)_5(OH_2)_4SO_4\cdot(H_2O)_6]^{-}$[‡]	-2328.141	0.286	-2328.787
Outer-Sphere Complex			
$Al_2(OH)_4(OH_2)_6SO_4\cdot(H_2O)_9$	-2634.475	0.391	-2635.186

[a] Gas-phase electronic energy of geometry-optimized reactants and products (B3LYP/6-31+G(d,p)). [b] Thermal correction to the Gibbs free energy derived from the frequency calculations. [c] Total free energy in solution, including all non-electrostatic terms, derived from single-point IEFPCM energy calculations (B3LYP/6-311++G(df,pd)). [†] Monodentate sulfate complex H-bonded to an adjacent singly coordinated OH_2 functional group. [‡] Monodentate sulfate complex H-bonded to an adjacent singly coordinated OH functional group.

Table 3.2 DFT-calculated energies of the sulfate adsorption pathways on variably-charged edge-sharing dioctahedral Al^{3+} cluster models, using the reactant and product energies listed in Table 3.1. The energies are in kJ mol^{-1} (1 Hartree = 2625.5 kJ mol^{-1}).

Pathways

Bidentate Bridging Adsorption

$\chi = 2$ – $SO_4^{2-}(H_2O)_9 + [Al_2(OH)_4(OH_2)_6 \cdot (H_2O)_6]^{2+} \rightarrow Al_2(OH)_4(OH_2)_4SO_4 \cdot (H_2O)_6 + 1.1(H_2O)_{10}$
ΔG = -124.0
$\chi = 1$ – $SO_4^{2-}(H_2O)_9 + [Al_2(OH)_5(OH_2)_5 \cdot (H_2O)_6]^{+} \rightarrow Al_2(OH)_4(OH_2)_4SO_4 \cdot (H_2O)_6 + OH^{-}(H_2O)_{10}$
ΔG = -47.2
$\chi = 0$ – $SO_4^{2-}(H_2O)_9 + Al_2(OH)_6(OH_2)_4 \cdot (H_2O)_6 \rightarrow Al_2(OH)_4(OH_2)_4SO_4 \cdot (H_2O)_6 + (OH^{-})_2(H_2O)_9$
ΔG = +5.9

Monodentate Adsorption

$\chi = 1$ – $SO_4^{2-}(H_2O)_9 + [Al_2(OH)_5(OH_2)_5 \cdot (H_2O)_6]^{+} \rightarrow [Al_2(OH)_5(OH_2)_4SO_4 \cdot (H_2O)_6]^{-} + (H_2O)_{10}$
ΔG = -48.1[†]
$\chi = 1$ – $SO_4^{2-}(H_2O)_9 + [Al_2(OH)_5(OH_2)_5 \cdot (H_2O)_6]^{+} \rightarrow [Al_2(OH)_5(OH_2)_4SO_4 \cdot (H_2O)_6]^{-} + (H_2O)_{10}$
ΔG = -18.8[‡]
$\chi = 0$ – $SO_4^{2-}(H_2O)_9 + Al_2(OH)_6(OH_2)_4 \cdot (H_2O)_6 \rightarrow [Al_2(OH)_5(OH_2)_4SO_4 \cdot (H_2O)_6]^{-} + OH^{-}(H_2O)_9$
ΔG = +22.2[†]
$\chi = 0$ – $SO_4^{2-}(H_2O)_9 + Al_2(OH)_6(OH_2)_4 \cdot (H_2O)_6 \rightarrow [Al_2(OH)_5(OH_2)_4SO_4 \cdot (H_2O)_6]^{-} + OH^{-}(H_2O)_9$
ΔG = +51.5[‡]

Outer-Sphere Adsorption

$\chi = 2$ – $SO_4^{2-}(H_2O)_9 + [Al_2(OH)_4(OH_2)_6 \cdot (H_2O)_6]^{2+} \rightarrow Al_2(OH)_4(OH_2)_6SO_4 \cdot (H_2O)_9 + 6/10(H_2O)_{10}$
ΔG = -68.8
$\chi = 1$ – $SO_4^{2-}(H_2O)_9 + [Al_2(OH)_5(OH_2)_5 \cdot (H_2O)_6]^{+} + 10H_2O \rightarrow Al_2(OH)_4(OH_2)_6SO_4 \cdot (H_2O)_9 +$
$6/10[10H_2O] + OH^{-}(H_2O)_9$
ΔG = -7.8
$\chi = 0$ – $SO_4^{2-}(H_2O)_9 + Al_2(OH)_6(OH_2)_4 \cdot (H_2O)_6 + 1.1[10H_2O] \rightarrow Al_2(OH)_4(OH_2)_6SO_4 \cdot (H_2O)_9 +$
$6/10[10H_2O] + (OH^{-})_2(H_2O)_9$
ΔG = +61.2

[†] Monodentate sulfate complex H-bonded to an adjacent singly coordinated OH_2 functional group.

[‡] Monodentate sulfate complex H-bonded to an adjacent singly coordinated OH functional group.

By way of illustration, Figures 3.1 and 3.2 display the bidentate bridging and monodentate sulfate adsorption pathways corresponding to $\chi = 1$, respectively. The DFT-calculated energies for these particular sulfate adsorption pathways were approximately -47 and -48 kJ mol^{-1}, respectively (Table 3.2). The bidentate bridging sulfate adsorption pathways were predicted to be exergonic (-124 to -47 kJ mol^{-1}) on the positively-charged Al^{3+} clusters ($\chi = 2$ and 1) (Table 3.2). However, the bidentate bridging sulfate adsorption pathway was predicted to be endergonic (+6 kJ mol^{-1}) on the neutral Al^{3+} cluster ($\chi = 0$) (Table 3.2). Consequently, the DFT-calculated sulfate adsorption energies were directly related to the lability of the exchanged functional groups (i.e., OH_2 versus OH).

In a single test, the energy of the bidentate bridging sulfate adsorption pathway corresponding to $\chi = 2$ was estimated with the IEFPCM method. Table 3.3 lists the IEFPCM-calculated energies of each reactant and product cluster model. The energy of the corresponding bidentate bridging adsorption pathway is listed in Table 3.4. Interestingly, the energy of the IEFPCM-calculated sulfate adsorption pathway was approximately 20% less exergonic (-124 versus -98 kJ mol^{-1}). As a result, for this particular test, the strict application of gas-phase geometry-optimized cluster models leads to a slight overestimation of the exergonicity of the sulfate adsorption pathway. This potential difference should be considered in future studies, computational resources permitting.

$SO_4^{2-}(H_2O)_9 + [Al_2(OH)_5(OH_2)_5\cdot(H_2O)_6]^+ \rightarrow Al_2(OH)_4(OH_2)_4SO_4\cdot(H_2O)_6 + OH^-(H_2O)_{10}$

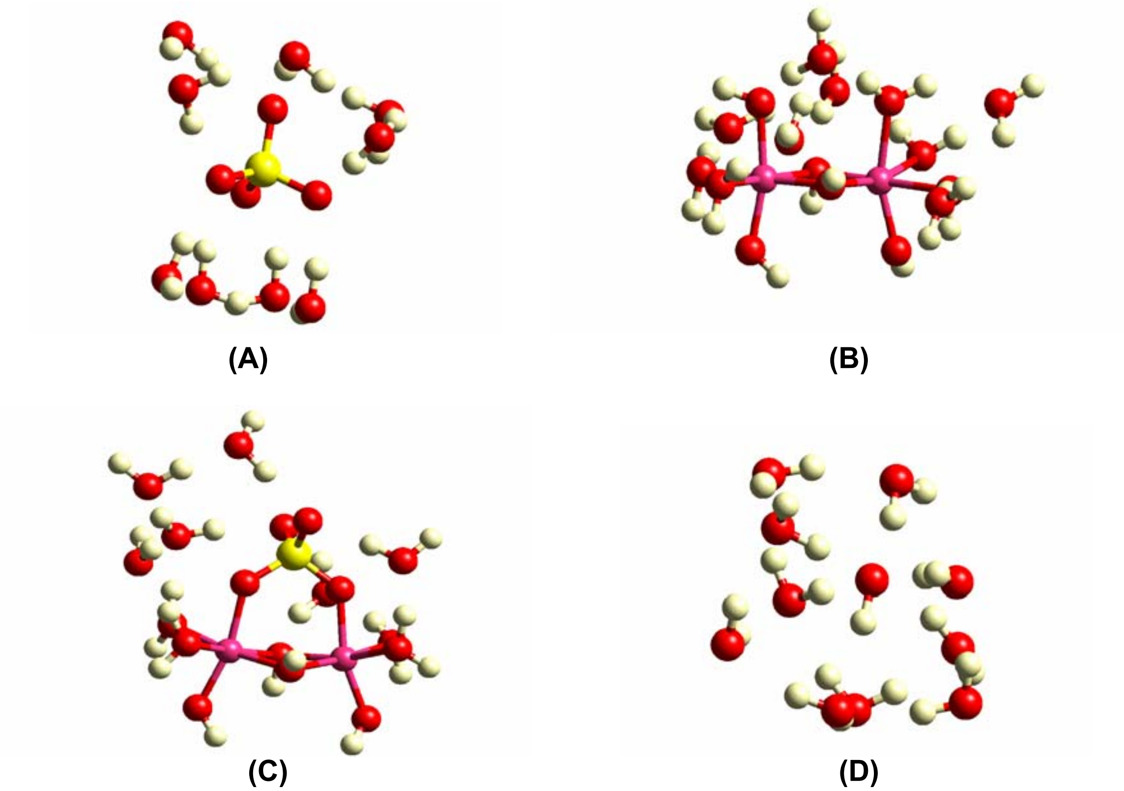

(A) (B)

(C) (D)

Figure 3.1 Bidentate bridging sulfate adsorption pathway corresponding to $\chi = 1$. The adsorption pathway is characterized by SO_4^{2-} exchanging with one singly coordinated OH_2 and one OH functional group. (A) $SO_4^{2-}(H_2O)_9$ reactant. (B) $[Al_2(OH)_5(OH_2)_5\cdot(H_2O)_6]^+$ reactant. (C) $Al_2(OH)_4(OH_2)_4SO_4\cdot(H_2O)_6$ product. (D) $OH^-(H_2O)_{10}$ product. Red, oxygen; white, hydrogen; yellow, sulfur; and pink, aluminum.

$$SO_4^{2-}(H_2O)_9 + [Al_2(OH_5)(OH_2)_5{\cdot}(H_2O)_6]^+ \rightarrow [Al_2(OH_5)(OH_2)_4SO_4{\cdot}(H_2O)_6]^- + (H_2O)_{10}$$

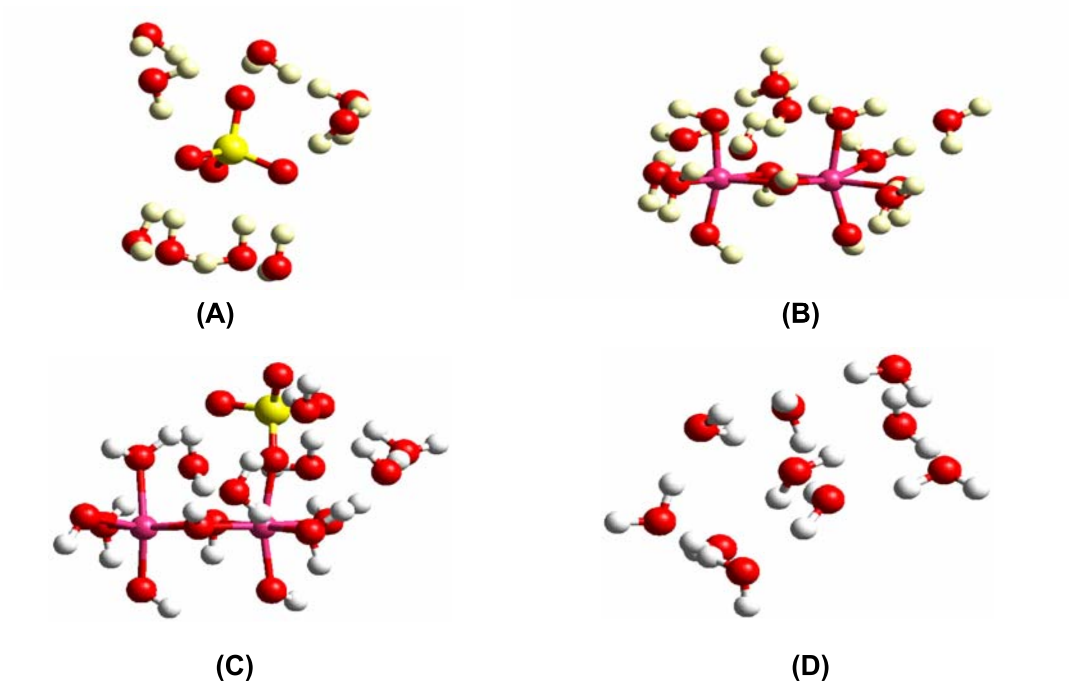

(A) (B)

(C) (D)

Figure 3.2 Monodentate sulfate adsorption pathway corresponding to $\chi = 1$. The adsorption pathway is characterized by SO_4^{2-} replacing one singly coordinated OH_2 functional group. (A) $SO_4^{2-}(H_2O)_9$ reactant. (B) $[Al_2(OH)_5(OH_2)_5{\cdot}(H_2O)_6]^+$ reactant. (C) $Al_2(OH)_5(OH_2)_4SO_4{\cdot}(H_2O)_6$ product. (D) $(H_2O)_{10}$ product. Red, oxygen; white, hydrogen; yellow, sulfur; and pink, aluminum.

Table 3.3 Energies of each reactant and product cluster contained in the bidentate bridging sulfate adsorption pathway ($\chi = 2$) listed in Table 3.4, calculated using the IEFPCM method. The energies are in Hartrees/molecule.

	E_{Total}[a]	$E_{Thermal}$[b]	E_{IEFPCM}[c]
Reactants			
$SO_4^{2-}\cdot(H_2O)_9$	-1387.424	0.177	-1387.795
$[Al_2(OH)_4(OH_2)_6\cdot(H_2O)_6]^{2+}$	-1705.767	0.287	-1706.218
Products			
$(H_2O)_{10}$	-764.514	0.194	-764.769
$Al_2(OH)_4(OH_2)_4SO_4\cdot(H_2O)_6$	-2252.273	0.260	-2252.813

[a]Total free energy in solution, including all non-electrostatic terms, from an IEFPCM geometry optimization (B3LYP/6-31+G(d,p)). [b]Thermal correction to the Gibbs free energy derived from an IEFPCM frequency calculation. [c]Total free energy in solution, including all non-electrostatic terms, derived from single-point IEFPCM energy calculations performed on the IEFPCM geometry-optimized clusters (B3LYP/6-311++G(df,pd)).

Table 3.4 DFT-calculated energies for the bidentate bridging sulfate adsorption pathway corresponding to $\chi = 2$, using the reactant and product energies listed in Tables 3.1 and 3.3. The energies are in kJ mol^{-1} (1 Hartree = 2625.5 kJ mol^{-1}).

Pathways

$\boldsymbol{\chi = 2}$ **–** $SO_4^{2-}(H_2O)_9 + [Al_2(OH)_4(OH_2)_6\cdot(H_2O)_6]^{2+} \rightarrow Al_2(OH)_4(OH_2)_4SO_4\cdot(H_2O)_6 + 1.1(H_2O)_{10}$

$\boldsymbol{\Delta G = -124.0}$[a]

$\boldsymbol{\chi = 2}$ **–** $SO_4^{2-}(H_2O)_9 + [Al_2(OH)_4(OH_2)_6\cdot(H_2O)_6]^{2+} \rightarrow Al_2(OH)_4(OH_2)_4SO_4\cdot(H_2O)_6 + 1.1(H_2O)_{10}$

$\boldsymbol{\Delta G = -98.0}$[b]

[a]Estimated adsorption energy based upon the gas-phase geometry-optimized clusters (Tables 3.1 and 3.2). [b]Estimated adsorption energy based upon the IEFPCM geometry-optimized clusters (Table 3.3). Single-point IEFPCM energy calculations (B3LYP/6-311++G(df,pd) were performed for the cluster models in both [a] and [b].

Similar to bidentate bridging sulfate adsorption, the monodentate sulfate adsorption pathways were predicted to be exergonic (-48 to -19 kJ mol^{-1}) on the positively-charged Al^{3+} cluster ($\chi = 1$) (Table 3.2). However, the monodentate sulfate adsorption pathways were predicted to be endergonic (+22 to +52 kJ mol^{-1}) on the neutral Al^{3+} cluster ($\chi = 0$) (Table 3.2). Therefore, similar to bidentate bridging sulfate adsorption, the DFT-calculated monodentate sulfate adsorption energies were directly related to the lability of the exchanged functional group (i.e., OH_2 versus OH). At present, it is unknown how inner-sphere sulfate complexes interact, at the molecular-scale, with the different types of hydroxyl functional groups that occupy mineral surfaces. Furthermore, the effect that these H-bonding interactions may have on the energies of sulfate adsorption has not been previously considered.

To improve our understanding of these H-bonding interactions, monodentate sulfate adsorption energies were estimated for pathways in which sulfate H-bonded to an adjacent OH_2 or OH functional group. The adsorption energies estimated for sulfate H-bonded to an adjacent OH functional group were significantly less exergonic (< 30 kJ mol^{-1}), in comparison with sulfate H-bonded to an adjacent OH_2 functional group (Table 3.2). Consequently, the electrostatic attraction to the adjacent functional group affected the adsorption energy of monodentate sulfate. For example, the adsorption energy was approximately -48 kJ mol^{-1} when sulfate H-bonded to the positively-charged OH_2 adsorption site ($\chi = 1$). Conversely, the adsorption energy was approximately -19 kJ mol^{-1} when sulfate H-bonded to the neutrally-charged OH adsorption site ($\chi = 1$) (Table 3.2). In Chapter 5, quantum molecular dynamics (QMD) simulations are used to explore the H-bonding of inner-sphere sulfate and phosphate complexes with hydroxyl functional groups of the (101) surface of α-FeOOH.

He *et al.* [20] proposed that the adsorption of outer-sphere sulfate could be described by three pH-dependent pathways. In this study, the energies of these three outer-sphere sulfate adsorption pathways were estimated (Table 3.2). The configuration of the outer-sphere sulfate complex was qualitatively similar to a configuration proposed by He *et al.* [20]. In Figure 3.3, the configuration of the outer-sphere sulfate complex is displayed. The outer-sphere sulfate adsorption pathways were predicted to be exergonic (-69 to -8 kJ mol^{-1}) on the positively-charged Al^{3+} clusters ($\chi = 2$ and 1). However, the outer-sphere sulfate adsorption pathway was predicted to be endergonic (+61 kJ mol^{-1}) on the neutral Al^{3+} cluster ($\chi = 0$) (Table 3.2). Accordingly, the DFT-calculated outer-sphere sulfate adsorption energies were significantly affected by the electrostatic attraction between the positively-charged OH_2 adsorption sites and the negatively-charged sulfate anion. In brief, the energies of the inner-sphere and outer-sphere sulfate adsorption pathways were related to the lability of the exchanged functional groups or the degree of electrostatic attraction, respectively, as reflected by the values of χ.

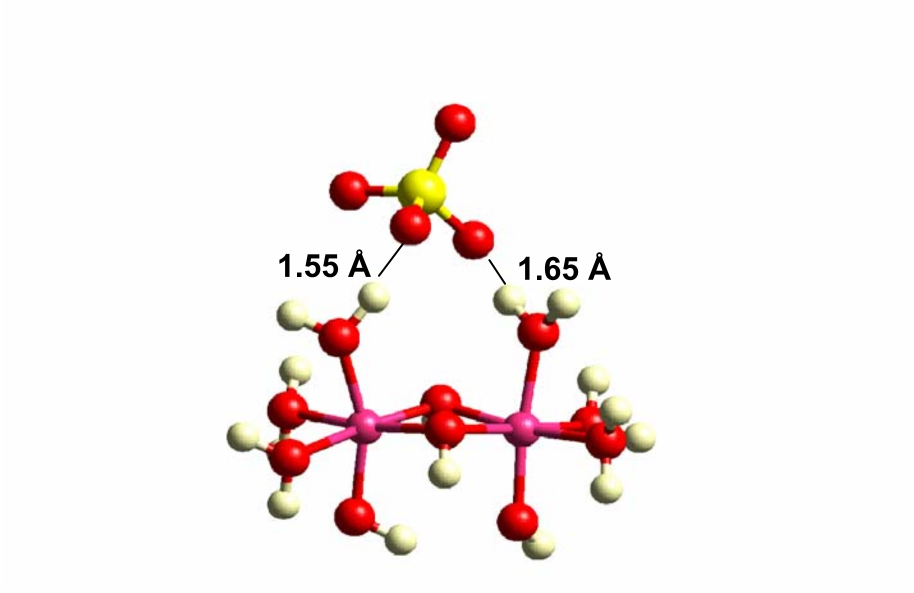

Figure 3.3 Outer-sphere sulfate complex, $Al_2(OH)_4(OH_2)_6SO_4 \cdot (H_2O)_9$. The nine explicit H_2O molecules are omitted to simplify the figure and highlight the H-bonding interactions with singly coordinated OH_2 functional groups. Red, oxygen; white, hydrogen; yellow, sulfur; and pink, aluminum.

In Figure 3.4, the DFT-calculated energies for the sulfate adsorption pathways on the variably-charged Al^{3+} and Fe^{3+} clusters are summarized (energies are listed in Tables 3.2 and 3.6). A few general observations will be noted, momentarily focusing on the adsorption pathways involving the variably-charged Al^{3+} clusters. The most exergonic pathway corresponded to the $\chi = 2$ bidentate bridging sulfate adsorption pathway. This pathway was significantly more exergonic than the $\chi = 2$ outer-sphere and $\chi = 1$ monodentate sulfate adsorption pathways. The $\chi = 2$ bidentate bridging sulfate adsorption pathway can be characterized as entropy-driven, which is probably reflected in its comparatively favorable adsorption energy. Interestingly, however, the energies of the bidentate bridging and monodentate sulfate adsorption pathways on the +1 charged Al^{3+} cluster ($\chi = 1$) were indistinguishable (monodentate sulfate complex H- bonded to an adjacent OH_2 functional group). Although the bidentate bridging sulfate adsorption pathway for $\chi = 1$ is also entropy-driven, a significant energy penalty is probably paid due to exchange with an OH functional group. Note that all of the sulfate adsorption pathways on the neutral Al^{3+} cluster were estimated to be thermodynamically unfavorable (i.e., endergonic).

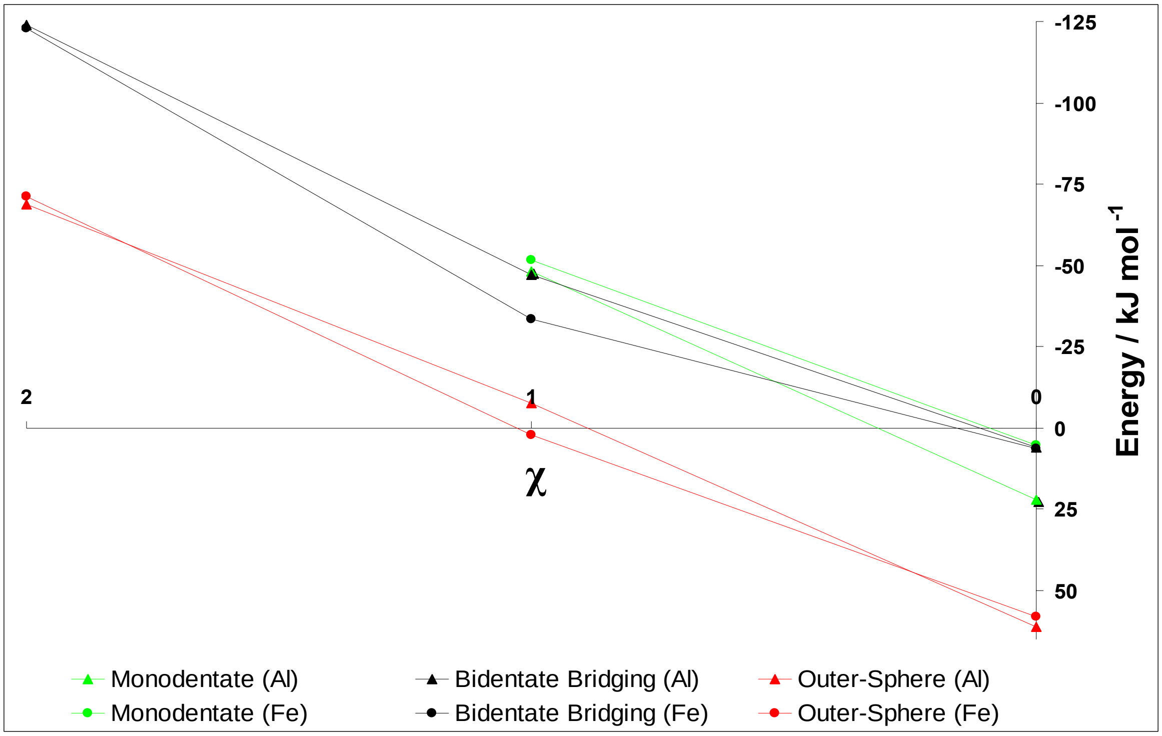

Figure 3.4 DFT-calculated energies for the sulfate adsorption pathways on variably-charged Al^{3+} and Fe^{3+} clusters. The energies are listed in Tables 3.2 and 3.6. For monodentate sulfate, the energies are plotted for pathways in which the sulfate complex was H-bonded to an adjacent singly coordinated OH_2 functional group.

The equilibrium adsorption of sulfate on Al-(hydr)oxides has been extensively studied experimentally, but the mechanisms of sulfate adsorption remain debatable. Based upon surface-charge measurements, for example, Rajan [37] proposed a bidentate bridging sulfate adsorption mechanism on hydrous alumina. A bidentate bridging mechanism is in qualitative agreement with the relatively favorable DFT-calculated adsorption energy for the $\chi = 2$ bidentate bridging sulfate pathway (-124 versus -48 and -69 kJ mol^{-1} for the monodentate and outer-sphere sulfate adsorption pathways at $\chi = 1$ and $\chi = 2$, respectively, Table 3.2). Rajan [37] performed the sulfate adsorption experiments at pH 5, substantially below the reported pH_{pzc} of 9.3 for the hydrous alumina. Thus, the hydrous alumina possessed significant positive surface-charge density, which may be qualitatively comparable to the $\chi = 2$ bidentate bridging sulfate adsorption pathway modeled in this study.

It is important to note, however, that investigators have also proposed that the adsorption of sulfate on Al-(hydr)oxides can be characterized by an outer-sphere mechanism [13, 17]. Furthermore, based upon IR spectroscopic measurements, the adsorption and speciation of sulfate on Al-(hydr)oxides has been shown to be sensitive to hydration [13]. Determining the effects of hydration on the DFT-calculated sulfate adsorption energies was beyond the scope of the present study. Note from Figure 3.4, however, that both inner-sphere and outer-sphere sulfate adsorption pathways were predicted to be exergonic for reactions characterized by $\chi = 2$ and 1. Therefore, at $pH < pH_{pzc}$, both inner-sphere and outer-sphere adsorption complexes could coexist, which was previously suggested by Wijnja and Schulthess [17]. Unfortunately, to the best of our knowledge, the energies of sulfate adsorption on common soil Al-(hydr)oxides have not been measured. Such measurements are critically needed to make significant progress with respect to elucidating the mechanisms of sulfate adsorption on Al-(hydr)oxides.

An acknowledged characteristic of sulfate adsorption on variably-charged Al- and Fe-(hydr)oxides is the relationship between surface loading and solution pH. Numerous macroscopic and spectroscopic studies have shown that an increase in solution pH causes a significant decrease in the surface loading of sulfate (e.g. [8, 12, 20, 40-50]). The inverse relationship between surface loading and solution pH is attributed to a reduction in the positive surface charge density, and increased competition with OH^- adsorption, as pH increases. The DFT calculations presented in this study are in qualitative agreement with this experimental observation. Experimentally, the surface loading of sulfate is insignificant at pH values greater than the bulk pH_{pzc} of a mineral (net charge, averaged over all the surfaces, equal to zero). The DFT calculations are in qualitative agreement with this observation wherein the sulfate adsorption pathways were predicted to be endergonic on neutral Al^{3+} and Fe^{3+} reactant clusters ($\chi = 0$, Figure 3.4). As the positive surface charge density increases (i.e., pH decreases) the thermodynamic favorability of sulfate adsorption also increases, which is expressed experimentally by the Gibbs free energy [21].

Table 3.5 lists the DFT-calculated energies for each reactant and product cluster used to estimate the energies of the sulfate adsorption pathways on edge-sharing dioctahedral Fe^{3+} cluster models (Table 3.6). Note from Table 3.6 that two DFT-calculated energies are listed for the $\chi = 2$ bidentate bridging sulfate adsorption pathway, namely, -122.8 and -121.7 kJ mol^{-1}. These two energies correspond to DFT calculations performed with or without the use of an RECP basis set for the Fe atoms, respectively. The two DFT-calculated adsorption energies were indistinguishable (i.e., equivalent optimized-geometries) and therefore an RECP basis set was used for the Fe atoms to minimize the computational workload, relative to an all-electron basis set. To facilitate the comparison between DFT-calculated energies for sulfate adsorption pathways on Al^{3+} and Fe^{3+} clusters, identical pathways were modeled (Tables 3.2 and 3.6). An exception was the monodentate sulfate adsorption pathways, in which the monodentate sulfate complex was H-bonded with an adjacent singly coordinated OH_2 functional group.

In general, the DFT-calculated energies of the sulfate adsorption pathways involving Al^{3+} and Fe^{3+} cluster models were qualitatively similar, as exemplified by Figure 3.4. It is important to note, however, that the energies of sulfate adsorption are probably affected by the unique structures and compositions of periodic Al- and Fe-(hydr)oxide surfaces. In brief, the DFT-calculated sulfate adsorption energies were dictated by the lability of the exchanged functional groups (inner-sphere sulfate adsorption) and electrostatic forces (outer-sphere sulfate adsorption).

Table 3.5 DFT-calculated energies for each reactant and product cluster contained in the sulfate adsorption pathways listed in Table 3.6. The energies are in Hartrees/molecule. Some of the reactant and product clusters, and their corresponding energies, are listed in Table 3.1.

	E_{Gas}[a]	$E_{Thermal}$[b]	E_{IEFPCM}[c]
Reactants			
$[Fe_2(OH)_4(OH_2)_6\cdot(H_2O)_6]^{2+\dagger}$	-3747.639	0.287	-3748.461
$[Fe_2(OH)_4(OH_2)_6\cdot(H_2O)_6]^{2+\ddagger}$	-1467.088	0.287	-1467.753
$[Fe_2(OH)_5(OH_2)_5\cdot(H_2O)_6]^{+}$	-1466.788	0.276	-1467.296
$Fe_2(OH)_6(OH_2)_4\cdot(H_2O)_6$	-1466.393	0.272	-1466.840
Products			
Bidentate Bridging Complex			
$Fe_2(OH)_4(OH_2)_4SO_4\cdot(H_2O)_6^{\dagger}$	-4294.358	0.257	-4295.060
$Fe_2(OH)_4(OH_2)_4SO_4\cdot(H_2O)_6^{\ddagger}$	-2013.803	0.258	-2014.353
Monodentate Complexes			
$[Fe_2(OH)_5(OH_2)_4SO_4\cdot(H_2O)_6]^{-\S}$	-2089.741	0.273	-2090.351
Outer-Sphere Complex			
$Fe_2(OH)_4(OH_2)_6SO_4\cdot(H_2O)_9$	-2396.047	0.375	-2396.731

[a] Gas-phase electronic energy of geometry-optimized reactants and products (B3LYP/6-31+G(d,p)). [b] Thermal correction to the Gibbs free energy derived from the frequency calculations. [c] Total free energy in solution, including all non-electrostatic terms, derived from single-point IEFPCM energy calculations (B3LYP/6-311++G(df,pd)). Note that the CEP-121G basis set was used for the Fe atoms in all of the DFT calculations except where noted. [†] DFT calculations performed without the CEP-121G relativistic effective core potential basis set for the Fe atoms (B3LYP/6-31+G(d,p)). [‡] DFT calculations performed with the CEP-121G relativistic effective core potential basis set for the Fe atoms (B3LYP/CEP-121G//6-31+G(d,p)). [§] Monodentate sulfate complex H-bonded to a singly coordinated OH_2 functional group.

Table 3.6 DFT-calculated energies of the sulfate adsorption pathways on variably-charged edge-sharing dioctahedral Fe^{3+} cluster models, using the reactant and product energies listed in Table 3.5. The energies are in kJ mol^{-1} (1 Hartree = 2625.5 kJ mol^{-1}).

Pathways

Bidentate Bridging Adsorption

χ = 2 – $SO_4^{2-}(H_2O)_9 + [Fe_2(OH)_4(OH_2)_6{\cdot}(H_2O)_6]^{2+} \rightarrow Fe_2(OH)_4(OH_2)_4SO_4{\cdot}(H_2O)_6 + 1.1(H_2O)_{10}$
ΔG = -121.7[†]
χ = 2 – $SO_4^{2-}(H_2O)_9 + [Fe_2(OH)_4(OH_2)_6{\cdot}(H_2O)_6]^{2+} \rightarrow Fe_2(OH)_4(OH_2)_4SO_4{\cdot}(H_2O)_6 + 1.1(H_2O)_{10}$
ΔG = -122.8[‡]
χ = 1 – $SO_4^{2-}(H_2O)_9 + [Fe_2(OH)_5(OH_2)_5{\cdot}(H_2O)_6]^{+} \rightarrow Fe_2(OH)_4(OH_2)_4SO_4{\cdot}(H_2O)_6 + OH^{-}(H_2O)_{10}$
ΔG = -33.6
χ = 0 – $SO_4^{2-}(H_2O)_9 + Fe_2(OH)_6(OH_2)_4{\cdot}(H_2O)_6 \rightarrow Fe_2(OH)_4(OH_2)_4SO_4{\cdot}(H_2O)_6 + (OH^{-})_2(H_2O)_9$
ΔG = +6.3

Monodentate Adsorption

χ = 1 – $SO_4^{2-}(H_2O)_9 + [Fe_2(OH)_5(OH_2)_5{\cdot}(H_2O)_6]^{+} \rightarrow [Fe_2(OH)_5(OH_2)_4SO_4{\cdot}(H_2O)_6]^{-} + (H_2O)_{10}$
ΔG = -51.7
χ = 0 – $SO_4^{2-}(H_2O)_9 + Fe_2(OH)_6(OH_2)_4{\cdot}(H_2O)_6 \rightarrow [Fe_2(OH)_5(OH_2)_4SO_4{\cdot}(H_2O)_6]^{-} + OH^{-}(H_2O)_9$
ΔG = +5.3

Outer-Sphere Adsorption

χ = 2 – $SO_4^{2-}(H_2O)_9 + [Fe_2(OH)_4(OH_2)_6{\cdot}(H_2O)_6]^{2+} \rightarrow Fe_2(OH)_4(OH_2)_6SO_4{\cdot}(H_2O)_9 + 6/10(H_2O)_{10}$
ΔG = -71.3
χ = 1 – $SO_4^{2-}(H_2O)_9 + [Fe_2(OH)_5(OH_2)_5{\cdot}(H_2O)_6]^{+} + 10H_2O \rightarrow Fe_2(OH)_4(OH_2)_6SO_4{\cdot}(H_2O)_9 + 6/10[10H_2O] + OH^{-}(H_2O)_9$
ΔG = +2.3
χ = 0 – $SO_4^{2-}(H_2O)_9 + Fe_2(OH)_6(OH_2)_4{\cdot}(H_2O)_6 + 1.1[10H_2O] \rightarrow Fe_2(OH)_4(OH_2)_6SO_4{\cdot}(H_2O)_9 + 6/10[10H_2O] + (OH^{-})_2(H_2O)_9$
ΔG = +57.9

[†] DFT calculations performed without the CEP-121G relativistic effective core potential basis set for the Fe atoms (B3LYP/6-31+G(d,p)). [‡] DFT calculations performed with the CEP-121G relativistic effective core potential basis set for the Fe atoms (B3LYP/CEP-121G//6-31+G(d,p)).

Aylmore *et al.* [51] measured the adsorption and desorption isotherms for sulfate reacted with hematite (α-Fe_2O_3) and pseudoboehmite (AlOOH) and observed that the isotherms were nearly identical. As a result, the mechanisms (and energies) of sulfate adsorption on α-Fe_2O_3 and AlOOH were probably similar. In addition, Aylmore *et al.* [51] observed significant hysteresis (i.e., irreversibility) between the adsorption and desorption pathways. Compared to monodentate and outer-sphere sulfate desorption, bidentate bridging sulfate desorption probably exhibits the highest degree of hysteresis (i.e., breaking of two (S)O-Fe bonds).

The adsorption and desorption isotherms reported by Aylmore *et al.* [51] were measured at pH 4.6. Consequently, the bulk α-Fe_2O_3 and AlOOH samples probably had significant positive surface-charge density (pH_{pzc} values not reported), similar to the experimental conditions of Rajan [37] for hydrous alumina. In this study, the energies of the $\chi = 2$ bidentate bridging sulfate adsorption pathways on the Al^{3+} and Fe^{3+} clusters were estimated to be equivalent. Furthermore, the DFT-calculated bidentate bridging sulfate adsorption energies were significantly more exergonic than the monodentate and outer-sphere sulfate adsorption energies (Tables 3.2 and 3.6). These findings are in qualitative agreement with the macroscopic observations reported by Aylmore *et al.* [51]. Unfortunately, however, neither χ nor the sulfate adsorption energies were measured by Aylmore *et al.* [51]. It should be noted that Turner and Kramer [18] reported that χ was approximately equal to 2.36 for natural α-Fe_2O_3 (though χ was less for synthetic α-Fe_2O_3).

To the best of our knowledge, only a single experimental study has measured the free energy of sulfate adsorption on a common soil mineral. Hansmann and Anderson [21] estimated the free energy of sulfate adsorption on α-FeOOH, by analyzing electrophoretic measurements within the framework of a Stern theory-based statistical model. The Stern theory-based statistical model adopted by Hansmann and Anderson [21] differed from surface complexation models because it was not constrained by *a priori* knowledge of the adsorption mechanism or reaction stoichiometry. Between pH 4 and 6, the net free energy of sulfate adsorption ranged from -36 to -30 kJ mol^{-1} ($\Delta G_{net} = \Delta G_{intrinsic} + \Delta G_{electrostatic}$). This experimental range agrees reasonably well with the DFT-calculated energies for the $\chi = 1$ monodentate and bidentate bridging sulfate adsorption pathways (Table 3.6, -52 and -34 kJ mol^{-1}, respectively). Of these two pathways, the monodentate sulfate adsorption pathway was more energetically favorable. Furthermore, it may be possible that the $\chi = 1$ bidentate bridging sulfate adsorption pathway is not entirely viable because a singly coordinated OH functional group is a poor leaving group.

The reasonable agreement between the experimental and DFT-calculated sulfate adsorption energies for the $\chi = 1$ pathways was encouraging and may have not been fortuitous. Specifically, Turner and Kramer [18] measured the H^+/SO_4^{2-} mole ratio for sulfate adsorption on α-FeOOH between pH 3 and 5 and reported values that ranged from 0.98 to 1.28 (i.e., $\chi \approx 1$). Furthermore, *in situ* IR vibrational spectroscopic [12, 17] and recent surface complexation modeling [38, 39] studies of sulfate adsorption on α-FeOOH have proposed monodentate adsorption mechanisms. However, several *ex situ* IR vibrational spectroscopic studies of sulfate adsorption on α-FeOOH have also proposed bidentate bridging adsorption mechanisms [9, 10, 18]. Regardless of the discrepancy between monodentate and bidentate bridging sulfate adsorption mechanisms, the complementary role of the DFT calculations is promising.

3.5 Conclusions

In this study, DFT calculations were performed to estimate the energies of potential inner-sphere and outer-sphere sulfate adsorption pathways on Al^{3+} and Fe^{3+} cluster models. For the inner-sphere sulfate adsorption pathways, the DFT-calculated adsorption energies were directly related to the lability of the exchanged functional groups (i.e., OH_2 versus OH). For the outer-sphere sulfate adsorption pathways, the DFT-calculated sulfate adsorption energies were directly related to the electrostatic attraction between the positively-charged OH_2 adsorption sites and the negatively-charged sulfate anion. The DFT-calculated energies for the sulfate adsorption pathways on Fe^{3+} cluster models were compared to experimental results available in the literature. Unfortunately, however, the literature is sorely lacking with respect to the measurement of sulfate adsorption energies on common soil minerals.

In a recent study, Kabengi *et al.* [52] performed flow-adsorption calorimetric measurements of arsenate sorption on amorphous Al-(hydr)oxide. Unfortunately, flow-adsorption calorimetry is underutilized, despite its potential to complement spectroscopic measurements and DFT calculations. Flow-adsorption calorimetric measurements would be especially helpful for testing the DFT-calculated adsorption energies presented in this study. Flow-adsorption calorimetric measurements would also be informative regarding the use of clusters for estimating the energies of sulfate adsorption pathways on Al- and Fe-(hydr)oxides.

For the DFT calculations presented in this study, three principal limitations should be stated. First, static configurations of cluster models were used to predict the energies of sulfate adsorption pathways. Unfortunately, reliable empirical force fields have not been developed for these types of systems. Empirical force fields would allow classical molecular dynamics or Monte Carlo simulations to be performed, wherein the configuration space could be adequately sampled. Second, the edge-sharing dioctahedral Al^{3+} and Fe^{3+} cluster models approximately simulate the local adsorption of sulfate. Periodic surfaces of Al- and Fe-(hydr)oxides have unique structures and compositions. Furthermore, sulfate adsorption at surface defect sites such as kinks and steps may be important. Third, the IEFPCM method applies a uniform dielectric medium that surrounds each cluster. In addition, the dielectric constant of water near a mineral surface is significantly different than that of bulk water. Further development of these methods should consider such limitations.

3.5 References

1. Brady, N. C.; Weil, R. R., *The Nature and Properties of Soils*. 12th ed.; Prentice Hall: Upper Saddle River, N.J., 1999.

2. Freeze, R. A.; Cherry, J. A., What Has Gone Wrong. *Ground Water* **1989,** *27*, (4), 458-464.

3. Rose, S.; Elliott, W. C., The Effects of pH Regulation Upon the Release of Sulfate from Ferric Precipitates Formed in Acid Mine Drainage. *Applied Geochemistry* **2000,** *15*, (1), 27-34.

4. Sposito, G., *The Surface Chemistry of Soils.* Oxford University Press: New York, 1984.

5. Eggleston, C. M.; Hug, S.; Stumm, W.; Sulzberger, B.; Afonso, M. D., Surface Complexation of Sulfate by Hematite Surfaces: FTIR and STM Observations. *Geochimica Et Cosmochimica Acta* **1998,** *62*, (4), 585-593.

6. Gessa, C.; Decherchi, M. L.; Melis, P.; Micera, G.; Erre, L. S., Anion-Induced Metal-Binding in Amorphous Aluminum Hydroxide. *Colloids and Surfaces* **1984,** *11*, (1-2), 109-117.

7. Harrison, J. B.; Berkheiser, V. E., Anion Interactions with Freshly Prepared Hydrous Iron Oxides. *Clays and Clay Minerals* **1982,** *30*, (2), 97-102.

8. Hug, S. J., *In Situ* Fourier Transform Infrared Measurements of Sulfate Adsorption on Hematite in Aqueous Solutions. *Journal of Colloid and Interface Science* **1997,** *188*, (2), 415-422.

9. Parfitt, R. L.; Smart, R. S. C., Infrared Spectra from Binuclear Bridging Complexes of Sulfate Adsorbed on Goethite (α-FeOOH). *Journal of the Chemical Society-Faraday Transactions I* **1977,** *73*, 796-802.

10. Parfitt, R. L.; Smart, R. S. C., The Mechanism of Sulfate Adsorption on Iron Oxides. *Soil Science Society of America Journal* **1978,** *42*, (1), 48-50.

11. Paul, K. W.; Borda, M. J.; Kubicki, J. D.; Sparks, D. L., Effect of Dehydration on Sulfate Coordination and Speciation at the Fe-(hydr)oxide-Water Interface: A Molecular Orbital/Density Functional Theory and Fourier Transform Infrared Spectroscopic Investigation. *Langmuir* **2005,** *21*, (24), 11071-11078.

12. Peak, D.; Ford, R. G.; Sparks, D. L., An *In Situ* ATR-FTIR Investigation of Sulfate Bonding Mechanisms on Goethite. *Journal of Colloid and Interface Science* **1999,** *218*, (1), 289-299.

13. Serna, C. J.; White, J. L.; Hem, S. L., Anion-Aluminum Hydroxide Gel Interactions. *Soil Science Society of America Journal* **1977,** *41*, (5), 1009-1013.

14. Spielbauer, D., Implementation of the Scanning Multichannel Technique in Raman-Spectroscopy and the Application for the Characterization of Oxides. *Applied Spectroscopy* **1995,** *49*, (5), 650-654.

15. Turner, L. J.; Kramer, J. R., Irreversibility of Sulfate Sorption on Goethite and Hematite. *Water Air and Soil Pollution* **1992,** *63*, (1-2), 23-32.

16. Watanabe, H.; Gutleben, C. D.; Seto, J., Sulfate-Ions on the Surface of Maghemite and Hematite. *Solid State Ionics* **1994,** *69*, (1), 29-35.

17. Wijnja, H.; Schulthess, C. P., Vibrational Spectroscopy Study of Selenate and Sulfate Adsorption Mechanisms on Fe and Al (hydr)oxide Surfaces. *Journal of Colloid and Interface Science* **2000,** *229*, (1), 286-297.

18. Turner, L. J.; Kramer, J. R., Sulfate Ion Binding on Goethite and Hematite. *Soil Science* **1991,** *152*, (3), 226-230.

19. Persson, P.; Lovgren, L., Potentiometric and Spectroscopic Studies of Sulfate Complexation at the Goethite-Water Interface. *Geochimica Et Cosmochimica Acta* **1996,** *60*, (15), 2789-2799.

20. He, L. M.; Zelazny, L. W.; Baligar, V. C.; Ritchey, K. D.; Martens, D. C., Hydroxyl-Sulfate Exchange Stoichiometry on γ-Al_2O_3 and Kaolinite. *Soil Science Society of America Journal* **1996,** *60*, (2), 442-452.

21. Hansmann, D. D.; Anderson, M. A., Using Electrophoresis in Modeling Sulfate, Selenite, and Phosphate Adsorption onto Goethite. *Environmental Science & Technology* **1985,** *19*, (6), 544-551.

22. Bargar, J. R.; Kubicki, J. D.; Reitmeyer, R.; Davis, J. A., ATR-FTIR Spectroscopic Characterization of Coexisting Carbonate Surface Complexes on Hematite. *Geochimica Et Cosmochimica Acta* **2005,** *69*, (6), 1527-1542.

23. Kwon, K. D.; Kubicki, J. D., Molecular Orbital Theory Study on Surface Complex Structures of Phosphates to Iron Hydroxides: Calculation of Vibrational Frequencies and Adsorption Energies. *Langmuir* **2004,** *20*, (21), 9249-9254.

24. Ladeira, A. C. Q.; Ciminelli, V. S. T.; Duarte, H. A.; Alves, M. C. M.; Ramos, A. Y., Mechanism of Anion Retention from EXAFS and Density Functional

Calculations: Arsenic (V) Adsorbed on Gibbsite. *Geochimica Et Cosmochimica Acta* **2001,** *65*, (8), 1211-1217.

25. Sherman, D. M.; Randall, S. R., Surface Complexation of Arsenic (V) to Iron (III) (hydr)oxides: Structural Mechanism from *Ab Initio* Molecular Geometries and EXAFS Spectroscopy. *Geochimica Et Cosmochimica Acta* **2003,** *67*, (22), 4223-4230.

26. Zhang, N. L.; Blowers, P.; Farrell, J., Evaluation of Density Functional Theory Methods for Studying Chemisorption of Arsenite on Ferric Hydroxides. *Environmental Science and Technology* **2005,** *39*, (13), 4816-4822.

27. Tribe, L.; Kwon, K. D.; Trout, C. C.; Kubicki, J. D., Molecular Orbital Theory Study on Surface Complex Structures of Glyphosate on Goethite: Calculation of Vibrational Frequencies. *Environmental Science and Technology* **2006,** *40*, (12), 3836-3841.

28. Sposito, G., On Points of Zero Charge. *Environmental Science and Technology* **1998,** *32*, (19), 2815-2819.

29. Frisch, M. J., Trucks, G. W., Schlegel, H. B., Scuseria, G. E., Robb, M. A., Cheeseman, J. R., Montgomery, Jr., J. A., Vreven, T., Kudin, K. N., Burant, J. C., Millam, J. M., Iyengar, S. S., Tomasi, J., Barone, V., Mennucci, B., Cossi, M., Scalmani, G., Rega, N., Petersson, G. A., Nakatsuji, H., Hada, M., Ehara, M., Toyota, K., Fukuda, R., Hasegawa, J., Ishida, M., Nakajima, T., Honda, Y., Kitao, O., Nakai, H., Klene, M., Li, X., Knox, J. E., Hratchian, H. P., Cross, J. B., Bakken, V., Adamo, C., Jaramillo, J., Gomperts, R., Stratmann, R. E., Yazyev, O., Austin, A. J., Cammi, R., Pomelli, C., Ochterski, J. W., Ayala, P. Y., Morokuma, K., Voth, G. A., Salvador, P., Dannenberg, J. J., Zakrzewski, V. G., Dapprich, S., Daniels, A. D., Strain, M. C., Farkas, O., Malick, D. K., Rabuck, A. D., Raghavachari, K., Foresman, J. B., Ortiz, J. V., Cui, Q., Baboul, A. G., Clifford, S., Cioslowski, J., Stefanov, B. B., Liu, G., Liashenko, A., Piskorz, P., Komaromi, I., Martin, R. L., Fox, D. J., Keith, T., Al-Laham, M. A., Peng, C. Y., Nanayakkara, A., Challacombe, M., Gill, P. M. W., Johnson, B., Chen, W., Wong, M. W., Gonzalez, C., and Pople, J. A. *Gaussian 03, revision B.05; Gaussian, Inc.;*, Wallingford CT, 2004.

30. Stephens, P. J.; Devlin, F. J.; Chabalowski, C. F.; Frisch, M. J., Ab-Initio Calculation of Vibrational Absorption and Circular-Dichroism Spectra Using Density-Functional Force-Fields. *Journal of Physical Chemistry* **1994,** *98*, (45), 11623-11627.

31. Becke, A. D., Density-Functional Thermochemistry 3. The Role of Exact Exchange. *Journal of Chemical Physics* **1993,** *98*, (7), 5648-5652.

32. Lee, C. T.; Yang, W. T.; Parr, R. G., Development of the Colle-Salvetti Correlation-Energy Formula into a Functional of the Electron-Density. *Physical Review B* **1988,** *37*, (2), 785-789.

33. Stevens, W. J.; Krauss, M.; Basch, H.; Jasien, P. G., Relativistic Compact Effective Potentials and Efficient, Shared-Exponent Basis-Sets for the 3rd-Row, 4th-Row, and 5th-Row Atoms. *Canadian Journal of Chemistry-Revue Canadienne De Chimie* **1992,** *70*, (2), 612-630.

34. Rotzinger, F. P., Performance of Molecular Orbital Methods and Density Functional Theory in the Computation of Geometries and Energies of Metal Aqua Ions. *Journal of Physical Chemistry B* **2005,** *109*, (4), 1510-1527.

35. Foresman, J. B.; Frisch, A., *Exploring Chemistry with Electronic Structure Methods.* 2nd ed.; Gaussian, Inc.: Pittsburgh, P.A., 1996.

36. Cances, E.; Mennucci, B.; Tomasi, J., A New Integral Equation Formalism for the Polarizable Continuum Model: Theoretical Background and Applications to Isotropic and Anisotropic Dielectrics. *Journal of Chemical Physics* **1997,** *107*, (8), 3032-3041.

37. Rajan, S. S. S., Sulfate Adsorbed on Hydrous Alumina, Ligands Displaced, and Changes in Surface-Charge. *Soil Science Society of America Journal* **1978,** *42*, (1), 39-44.

38. Fukushi, K.; Sverjensky, D. A., A Surface Complexation Model for Sulfate and Selenate on Iron Oxides Consistent with Spectroscopic and Theoretical Molecular Evidence. *Geochimica et Cosmochimica Acta* **2007,** *71*, (1), 1-24.

39. Sverjensky, D. A.; Fukushi, K., Anion Adsorption on Oxide Surfaces: Inclusion of the Water Dipole in Modeling the Electrostatics of Ligand Exchange. *Environ. Sci. Technol.* **2006,** *40*, (1), 263-271.

40. Ali, M. A.; Dzombak, D. A., Competitive Sorption of Simple Organic Acids and Sulfate on Goethite. *Environmental Science & Technology* **1996,** *30*, (4), 1061-1071.

41. Courchesne, F., Electrolyte Concentration and Composition Effects on Sulfate Sorption by 2 Spodosols. *Soil Science Society of America Journal* **1991,** *55*, (6), 1576-1581.

42. Geelhoed, J. S.; Hiemstra, T.; VanRiemsdijk, W. H., Phosphate and Sulfate Adsorption on Goethite: Single Anion and Competitive Adsorption. *Geochimica Et Cosmochimica Acta* **1997,** *61*, (12), 2389-2396.

43. Gobran, G. R.; Selim, H. M.; Hultberg, H.; Andersson, I., Sulfate Adsorption-Desorption in a Swedish Forest Soil. *Water Air and Soil Pollution* **1998,** *108*, (3-4), 411-424.

44. Gustafsson, J. P., Modeling pH-Dependent Sulfate Adsorption in the Bs Horizons of Podzolized Soils. *Journal of Environmental Quality* **1995,** *24*, (5), 882-888.

45. Marsh, K. B.; Tillman, R. W.; Syers, J. K., Charge Relationships of Sulfate Sorption by Soils. *Soil Science Society of America Journal* **1987,** *51*, (2), 318-323.

46. Martin, R. R.; Smart, R. S., X-Ray Photoelectron Studies of Anion Adsorption on Goethite. *Soil Science Society of America Journal* **1987,** *51*, (1), 54-56.

47. Rose, S.; Ghazi, A. M., Release of Sorbed Sulfate From Iron Oxyhydroxides Precipitated From Acid Mine Drainage Associated with Coal Mining. *Environmental Science & Technology* **1997,** *31*, (7), 2136-2140.

48. Sigg, L.; Stumm, W., The Interaction of Anions and Weak Acids with the Hydrous Goethite (α-FeOOH) Surface. *Colloids and Surfaces* **1981,** *2*, (2), 101-117.

49. Singh, B. R., Sulfate Sorption by Acid Forest Soils 3. Desorption of Sulfate from Adsorbed Surfaces as a Function of Time, Desorbing Ion, pH, and Amount of Adsorption. *Soil Science* **1984,** *138*, (5), 346-353.

50. Zhang, P. C.; Sparks, D. L., Kinetics and Mechanisms of Sulfate Adsorption Desorption on Goethite Using Pressure-Jump Relaxation. *Soil Science Society of America Journal* **1990,** *54*, (5), 1266-1273.

51. Aylmore, L. A. G.; Karim, M.; Quirk, J. P., Adsorption and Desorption of Sulfate Ions by Soil Constituents. *Soil Science* **1967,** *103*, (1), 10-15.

52. Kabengi, N. J.; Daroub, S. H.; Rhue, R. D., Energetics of Arsenate Sorption on Amorphous Aluminum Hydroxides Studied Using Flow Adsorption Calorimetry. *Journal of Colloid and Interface Science* **2006,** *297*, (1), 86-94.

Chapter 4

SULFATE ADSORPTION AT THE IRON OXIDE-WATER INTERFACE – COMPARISON OF CLUSTER AND PERIODIC SLAB DFT PREDICTIONS

4.1 Abstract

The transport and bioavailability of sulfate in soils are significantly affected by adsorption reactions at the mineral-H_2O interface. Therefore, an understanding of the mechanisms and kinetics of sulfate adsorption is of fundamental importance in soil chemistry. In this investigation, the binding geometries of bidentate bridging and monodentate sulfate complexes at the Fe-(hydr)oxide-H_2O interface were predicted, using static cluster and periodic slab density functional theory (DFT) calculations. The cluster calculations were performed with edge-sharing dioctahedral Fe^{3+} models, using the unrestricted PBE0 exchange-correlation functional and a combination of effective core potential (LanL2DZ – Fe atoms) and all-electron (6-311+G(d,p) or 6-311+G(3df,p) – S, O, and H atoms) basis sets. The periodic slab calculations were performed with a (3 x 2) supercell of the (100) α-FeOOH surface, using the projector-augmented wave method and a plane-wave basis set. For the periodic slab calculations, the spin-polarized (SP) PBE exchange-correlation functional, with and without explicit consideration of an on-site Coulomb interaction parameter (i.e., SP-PBE and SP-PBE+U methods), was used. Despite the lack of long-range order, cluster model predictions of the interatomic distances and angles of

bidentate bridging and monodentate sulfate were in good agreement with the periodic slab model predictions. Quantitative analysis of the cluster and periodic slab DFT predictions is expected to result from theoretical fitting of extended X-ray absorption fine structure measurements. The application of computational chemistry methods to soil chemistry research is anticipated to provide novel insight into the mechanisms and kinetics of ion sorption.

4.2 Introduction

The transport and bioavailability of sulfate in soils are significantly affected by adsorption reactions with metal oxides and clay minerals. In tropical soils that possess appreciable anion exchange capacity (AEC), for example, variably-charged Al- and Fe-(hydr)oxides and 1:1 clay minerals (e.g. kaolinite) can retain plant-available sulfate through adsorption. In soils that do not possess appreciable AEC, however, sulfate can become unavailable for plant uptake due to leaching through the soil profile [1]. Therefore, an understanding of the mechanisms and kinetics of sulfate adsorption is of fundamental importance in soil chemistry. In particular, determining the mechanisms of sulfate adsorption will help to constrain empirical surface complexation models, which are used to simulate the reactive transport of chemical species in soils.

Spectroscopic measurements can provide valuable molecular-scale information with respect to the mechanisms and kinetics of sulfate adsorption.

Unfortunately, the initial adsorption reactions of sulfate, and other oxyanions such as phosphate and arsenate, can reach steady-state rapidly (e.g. < 1 ms) [1]. As a result, it is challenging to perform high-resolution spectroscopic measurements necessary to identify reaction intermediates and to determine the kinetics of a reaction [2]. In addition, spectroscopic studies often use inconsistent experimental designs and data analysis protocols, which can lead to conflicting interpretations. Consequently, it remains difficult to systematically test and support proposed reaction mechanisms based upon spectroscopic measurements. In this respect, computational chemistry methods can provide novel insight into the mechanisms and kinetics of adsorption reactions. For example, computational chemistry methods can be used to interpret spectroscopic measurements, predict rate constants and activation barriers, and to estimate the energies of adsorption reactions.

Computational chemistry methods have been recently used to investigate the adsorption of oxyanions and organic acids on Al- and Fe-(hydr)oxides, particularly to interpret extended X-ray absorption fine structure (EXAFS) and Fourier transform infrared (FTIR) spectroscopic measurements [3-13]. In general, density functional theory (DFT) calculations were performed with edge-sharing dioctahedral Al^{3+} or Fe^{3+} cluster models (exceptions included [9, 10, 13]). For example, Sherman and Randall [6] investigated the adsorption of arsenate (As(V)) on Fe-(hydr)oxides, using a combination of EXAFS spectroscopy and DFT cluster model calculations. Previous EXAFS studies had proposed conflicting interpretations for As(V) adsorption on Fe-

(hydr)oxides, including bidentate bridging, bidentate chelating, and monodentate adsorption ([6] and references therein). The DFT cluster model calculations predicted that the most thermodynamically favorable adsorption product was a bidentate bridging As(V) complex. An EXAFS measurement of the As(V)–Fe interatomic distance agreed well with the bidentate bridging As(V) cluster model and corroborated the thermodynamic DFT prediction [6].

As another example, Paul *et al.* [5] investigated the effect of hydration on sulfate adsorption and speciation at the Fe-(hydr)oxide-H_2O interface, using a combination of attenuated total reflectance (ATR) FTIR spectroscopy and DFT cluster model calculations. DFT calculations of IR vibrational frequencies predicted that sulfate formed a bidentate bridging or monodentate complex at the Fe-(hydr)oxide-H_2O interface. Under dehydrated conditions, however, the DFT calculations predicted that a speciation change would occur. Specifically, sulfate probably accepts a proton to form a bidentate bridging or monodentate bisulfate complex. The results reported by the investigation of Paul *et al.* [5] were important because the moisture content of soils constantly fluctuates. Fluctuations in soil moisture content may affect nutrient transport and bioavailability, but unfortunately our understanding of this natural process remains limited.

DFT cluster model calculations of oxyanion and organic acid complexes have been valuable for predicting and interpreting EXAFS and FTIR spectroscopic measurements. However, previous DFT studies have generally relied on edge-sharing dioctahedral Al^{3+} and Fe^{3+} cluster models to simulate the surfaces of Al- and Fe-(hydr)oxide minerals. It is reasonable to assume that edge-sharing dioctahedral cluster models cannot accurately predict the binding geometries of oxyanion and organic acid complexes on every surface of a soil mineral. Common soil minerals, for example goethite (α-FeOOH), possess several surfaces with unique structures and compositions (e.g. the (101) and (001) α-FeOOH surfaces [14]). Consequently, complications may arise if the geometry-optimized structures of edge-sharing dioctahedral cluster models inaccurately predict binding geometries (e.g. interatomic distances). An alternative approach is to model a soil mineral surface as a periodic slab (i.e., 2-dimensional periodic surface constrained by boundary conditions). Unfortunately, few studies have used periodic slab models to investigate the adsorption of nutrients at the mineral-H_2O interface.

The objective of this investigation was to compare the binding geometries of inner-sphere sulfate complexes predicted by static cluster and by periodic slab DFT calculations. The DFT cluster calculations were performed with edge-sharing dioctahedral Fe^{3+} models. The periodic slab DFT calculations were performed with a (3 x 2) supercell of the (100) α-FeOOH surface. Goethite is the most abundant Fe-oxyhydroxide in soils. Furthermore, the (100) α-FeOOH surface possesses a similar structure and composition to the edge-sharing dioctahedral Fe^{3+} cluster models. The periodic slab DFT calculations realistically account for long-range order and should therefore predict accurate binding geometries. This investigation is also part of an ongoing research effort to analyze how well DFT models of sulfate complexes fit experimental EXAFS measurements. This investigation will demonstrate that DFT cluster models of inner-sphere sulfate complexes compare reasonably well with similar periodic slab DFT models, despite their lack of long-range order.

4.3 Methods

4.3.1 Cluster Model Calculations

The local coordination geometries of inner-sphere sulfate complexes were predicted with the use of static edge-sharing dioctahedral Fe^{3+} cluster models. Edge-sharing dioctahedral cluster models of metal cations, for example Al^{3+} and Mg^{2+}, have been shown to accurately reproduce the main geometrical features of metal oxides and clay minerals [15]. Similar cluster models have also been used to analyze the local coordination geometries of inner-sphere As(V) complexes on gibbsite [4] and Fe-(hydr)oxide minerals [6], as well as inner-sphere arsenite (As(III)) complexes on goethite [7, 16], based upon EXAFS measurements. In this investigation, bidentate bridging and monodentate sulfate complexes were modeled. Bidentate bridging and monodentate sulfate are the most common inner-sphere complexes proposed by spectroscopic studies [5, 17-24].

The overall charge of the edge-sharing dioctahedral Fe^{3+}-sulfate cluster models was neutral (i.e., +2 charged edge-sharing dioctahedral Fe^{3+} cluster and -2 charged sulfate). Therefore, the cluster model calculations simulated adsorption below the pH_{pzc} (i.e., $pH \leq pH_{pzc}$, where pH_{pzc} is defined as the pH at which the net surface charge density equals zero [25]). To simulate a hydrated environment, several explicit H_2O molecules (i.e., H_2O molecules included in the geometry optimization) were H-bonded to the sulfate complexes. Experimental studies have shown that hydration significantly influences the IR-active vibrational modes of oxyanion complexes [18, 26]. For bidentate bridging sulfate, cluster model calculations were performed with four or 10 explicit H_2O molecules (see Figures 4.1 and 4.4). For monodentate sulfate, cluster model calculations were performed with six or 10 explicit H_2O molecules (see Figures 4.1 and 4.4). In addition, the bidentate bridging sulfate cluster model containing four explicit H_2O molecules was geometry optimized with the Integral Equation Formalism Polarized Continuum Model (IEFPCM) method [27]. For the IEFPCM calculation, the dielectric constant of bulk water ($\varepsilon = 78.4$) was specified, and therefore both explicit and implicit solvation were considered.

The DFT cluster model calculations were performed with Gaussian 03 [28]. The DFT calculations were performed with the unrestricted, hybrid exchange-correlation functional of Perdew *et al.* [29], denoted UPBE0. The LanL2DZ effective core potential (ECP) basis set [30] was used for the Fe atoms. The high-spin state of Fe^{3+} was specified for each Fe atom. The 6-311+G(d,p) or 6-311+G(3df,p) all-electron basis sets were used for the S, O, and H atoms. It should be noted that several additional exchange-correlation functionals and basis sets were evaluated. For the purposes of this investigation, however, only the UPBE0 predictions are reported because of their comparatively closer agreement with the periodic slab DFT predictions. Numerous DFT investigations have used similar cluster model calculations of oxyanion and organic acid complexes on Al or Fe-(hydr)oxides, and successfully compared the predictions with experimental measurements [3-13, 31].

The starting configurations for the bidentate bridging (four explicit H_2O molecules) and monodentate (six explicit H_2O molecules) sulfate complexes corresponded to energy-minimized cluster models from a previous investigation [31]. The cluster models were geometry optimized without symmetry or geometrical constraints. Frequency calculations were subsequently performed to determine if the geometry optimization had successfully located a potential energy minimum (i.e., no imaginary frequencies). It should be noted, however, that only one static configuration was geometry-optimized for each cluster model. Therefore, the potential energy minima unlikely corresponded to the global minima for these configurations. Conformational analysis of the potential energy surfaces was not performed.

4.3.2 Periodic Slab Model Calculations

The unit cell of bulk α-FeOOH (*Pnma* space group) was constructed in Cerius^2 (Accelrys Inc., San Diego, California) according to the experimental lattice parameters and atomic coordinates reported by Szytula *et al.* [32]. The unit cell of bulk α-FeOOH was cleaved through the (100) plane ((010) plane in *Pbnm* space group [33]), corresponding to a depth of one unit cell. The (100) surface is a stable lowindex surface of α-FeOOH [34]. A slab model of the (100) α-FeOOH surface was constructed, corresponding to a quasi-cubic supercell with lattice vectors a=9.03, b=9.24, and c=8.89 Å (i.e., a (3 x 2) supercell). The (100) α-FeOOH surface was exposed equivalently on both sides of the slab. Periodic images of the supercell perpendicular to the (100) α-FeOOH surface (i.e., a-b plane) were separated by a vacuum space of approximately 10 Å (c=18.89 Å).

Cleavage of bulk α-FeOOH through the (100) plane resulted in surface Fe atoms with 5-fold coordination. The surface Fe atoms were terminated with singly coordinated OH_2 functional groups. The overall charge of the (100) α-FeOOH supercell was stoichiometrically neutral ($Fe_{24}O_{60}H_{48}$). The vacuum space was subsequently filled with explicit H_2O molecules, including the one or two singly coordinated OH_2 functional groups replaced by SO_4^{2-}, corresponding to a density of approximately 0.95 g cm^{-3}. One Ca^{2+} cation was also added to simulate the presence of a counterion and to maintain a neutrally-charged simulation cell. Starting configurations for the inner-sphere sulfate complexes at the (100) α-FeOOH-H_2O interface (e.g. bond distances and angles) were approximately equal to the energy-minimized configurations predicted by the DFT cluster model calculations.

The static periodic slab DFT calculations were performed with the Vienna *ab initio* simulation package (VASP) [35, 36]. VASP is a DFT electronic structure program that solves the Kohn-Sham equations [37], using pseudopotentials or the projector-augmented wave method and a plane-wave basis set. The exchange-correlation functional chosen was the spin-polarized generalized gradient approximation (SP-GGA) functional of Perdew *et al.* [29], denoted SP-PBE. The Kohn-Sham equations were solved by minimizing the norm of the residual vector to each eigenstate [38, 39], based upon efficient mixing of the charge density.

The electron-ion interactions were described by the projector-augmented wave method of Blöchl [40], as implemented by Kresse and Joubert [41]. The number of valence electrons treated explicitly for each heavy element was as follows: Fe, $3p^6 3d^7 4s^1$; O, $2s^2 2p^4$; S, $3s^2 3p^4$. Brillouin zone sampling was performed automatically through implementation of the Monkhorst-Pack scheme [42]. The reciprocal space of the Brillouin zone was subdivided into a 2 x 2 x 1 mesh, which resulted in two *k*-points that sampled the irreducible part of the Brillouin zone. The plane-wave kinetic energy cutoff was set to 400 eV. The atomic positions were relaxed using a conjugate-gradient algorithm. The geometry optimizations were considered completed when the Hellmann-Feynman forces acting on the atoms were less than 0.02 eV $Å^{-1}$ and the error in total energy was less than 10^{-4} eV. All of the atomic positions were allowed to relax, but the shape and size of the simulation cell were conserved. The geometry optimizations were performed with a first-order Gaussian smearing coefficient, σ, of 0.10 eV [43].

At room temperature, α-FeOOH is known to be an antiferromagnetic mineral. In this investigation, the number of unpaired valence electrons initially specified for each Fe atom corresponded to five (i.e., high-spin state of Fe^{3+}).

Unfortunately, SP-GGA methods can fail to correctly describe the strong electronic correlations of valence electrons in transition metal atoms. Therefore, the static periodic slab DFT calculations were performed with both the SP-GGA and SP-GGA+U methods. In both cases, the GGA functional corresponded to the SP-PBE exchange-correlation functional.

The SP-GGA+U method explicitly considers the on-site Coulomb repulsion for strongly correlated d- and f-electrons. In the SP-GGA+U method, a Hubbard term describing the on-site Coulomb and exchange interactions is added to the DFT Hamiltonian. Explicit consideration of the on-site Coulomb repulsion has been shown to significantly improve predictions of the local magnetic moments of Fe atoms, band gaps, and band energies for bulk hematite (α-Fe_2O_3) [44]. For a description of the SP-GGA+U method applied to the closely related α-Fe_2O_3 system, refer to Rollmann *et al.* [44]. In addition, refer to Rohrbach *et al.* [45] for implementation of the GGA+U method in VASP. Dudarev's rotationally-invariant approach to the SP-GGA+U method was used in this investigation [46]. The effective on-site Coulomb and exchange interaction parameters for each Fe atom were set to 4 eV and 1 eV, respectively, as recommended by Rollmann *et al.* [44].

4.4 Results and Discussion

The adsorption of sulfate at the Al- and Fe-(hydr)oxide-H_2O interface has received significant attention in the literature. In particular, several studies have published results from *in situ* ATR-FTIR spectroscopic measurements [5, 18-20, 47]. For example, Hug [18] performed ATR-FTIR spectroscopic measurements of sulfate adsorbed at the α-Fe_2O_3-H_2O interface as a function of pH and hydration. Interestingly, a diagnostic IR-active vibrational mode $\geq 1200\ cm^{-1}$ was only observed when the ATR-FTIR measurements were performed with dehydrated samples (i.e., *ex situ*). The diagnostic IR-active vibrational mode was also observed with sulfate solutions acidified below pH 2 (i.e., less than the pK_a of HSO_4^-). Hug [18] proposed that sample dehydration may alter the coordination or speciation of an inner-sphere sulfate complex. Paul *et al.* [5] subsequently showed with DFT cluster model calculations that sample dehydration probably results in bisulfate formation (i.e., a change in sulfate speciation).

The application of *in situ* ATR-FTIR spectroscopy to the investigation of oxyanion adsorption at the mineral-H_2O interface is not without its limitations. One principal limitation is that a point group symmetry analysis of the IR-active vibrational modes is generally performed to determine the binding geometry of a complex (e.g. monodentate or bidentate). Hence, IR spectroscopy has been referred to as an “indirect structural” method [48]. Unfortunately, the IR-active vibrational modes of an oxyanion complex are usually broad and overlapping. Consequently, identifying the exact number of IR-active vibrational modes remains challenging and interpretations can be inconclusive. For example, Paul *et al.* [5] found that the DFT-predicted υ_1 and υ_3 IR-active vibrational frequencies of monodentate and bidentate bridging sulfate had relatively similar energies. Assuming that the correct number of measured IR-active vibrational modes was identified, it was reasonable to propose a monodentate or bidentate bridging sulfate complex [5, 18]. Furthermore, although bisulfate probably formed on α-Fe_2O_3 as a function of dehydration, differentiating between the monodentate and bidentate bridging bisulfate complexes proved impossible (predicted IR-active vibrational frequencies were indistinguishable).

EXAFS is an alternative *in situ* spectroscopic method often used to investigate oxyanion adsorption at the mineral-H_2O interface. However, in contrast to IR spectroscopy, EXAFS is a "direct structural" method [48]. An EXAFS analysis typically provides the interatomic distances between a central absorbing atom and its next-nearest neighbors (e.g. first and second shells). Furthermore, the coordination numbers of the first and second shells can be estimated. In principle, EXAFS spectroscopy is capable of differentiating between monodentate and bidentate bridging complexes, assuming their second shell interatomic distances and coordination numbers are sufficiently different (e.g. [49]). To determine the binding geometry of an oxyanion complex at the mineral-H_2O interface, EXAFS analyses typically use standard reference compounds as structural models for EXAFS fitting. A promising alternative is to derive structural models from DFT cluster calculations (e.g. [9]). DFT-predicted structural models of oxyanion complexes can be used to calculate photoelectron scattering amplitudes and phase shifts necessary for EXAFS fitting.

Recently, we initiated an investigation into the adsorption of sulfate at the Fe-(hydr)oxide-H_2O interface, using a combination of S K-edge EXAFS spectroscopy and DFT model calculations. A primary goal of this research effort is to fit the EXAFS measurements with DFT-predicted structural models of sulfate complexes. In this respect, it is particularly worthwhile to quantify the potential differences between cluster and periodic slab DFT predictions. Several researchers have used DFT-predicted cluster models of adsorption complexes to interpret bulk EXAFS measurements [4, 6, 7, 9]. In addition, a growing number of metal and oxyanion adsorption studies are being performed with single-crystal mineral surfaces, using grazing incidence (GI) EXAFS and crystal truncation rod (CTR) diffraction measurements (e.g. [48, 50, 51]. For these adsorption experiments, DFT-predicted periodic slab models are anticipated to be especially valuable.

In Tables 4.1 and 4.2, selected interatomic distances and angles are listed for the bidentate bridging and monodentate sulfate complexes as predicted by the cluster and periodic slab DFT calculations, respectively. The geometry-optimized cluster and periodic slab DFT models are displayed in Figures 4.1 – 4.3. It should be noted that the periodic slab SP-PBE and SP-PBE+U calculations did not result in significant differences regarding the predicted interatomic distances and angles of the sulfate complexes (Table 4.2). As expected, however, differences were predicted for the average local magnetic moments of the individual Fe atoms. The average local magnetic moment was 3.65 μ_B/Fe atom (±0.03 μ_B) and 4.09 μ_B/Fe atom (±0.01 μ_B) for the SP-PBE and SP-PBE+U geometry-optimized static configurations, respectively. Nevertheless, differences in the average local magnetic moments of the individual Fe atoms did not significantly affect the geometries of the sulfate complexes.

The binding geometry of the bidentate bridging sulfate complex will be discussed first. Overall, the cluster and periodic slab DFT predictions of the interatomic distances and angles were in good agreement, with only a few notable exceptions (Tables 4.1 and 4.2). In EXAFS analysis, a diagnostic feature of the binding geometry of an oxyanion complex is its second shell interatomic distance (e.g. the S–Fe interatomic distance). The average S–Fe interatomic distance predicted by the cluster (3.25 Å, LanL2DZ/6-311+G(3df,p)) and periodic slab (3.29 Å) DFT calculations agreed to within 0.04 Å, approximately equal to experimental error [2] (Tables 4.1 and 4.2). The predicted average S–O and S–O(Fe) bond distances (i.e., first shell bond distances of S) were also in good agreement. The average S–O bond distance predicted by the cluster and periodic slab DFT calculations was 1.46 and 1.49 Å, respectively. Likewise, the average S–O(Fe) bond distance predicted by both the cluster and periodic slab DFT calculations was 1.49 Å (Tables 4.1 and 4.2).

Table 4.1 Geometry-optimized bidentate bridging and monodentate sulfate complexes on an edge-sharing dioctahedral Fe^{3+} cluster model. Interatomic distances are reported in angstroms (Å) and bond angles in degrees. * denotes interatomic distances and angles within the Fe-O-Fe-O ring between the two edge-sharing Fe^{3+} octahedra coordinated to sulfate.

	Bidentate SO_4^{2-} $Fe_2(OH)_4(OH_2)_4SO_4 \cdot (H_2O)_4$		**Monodentate SO_4^{2-} $Fe_2(OH)_4(OH_2)_5SO_4 \cdot (H_2O)_6$**	
	LanL2DZ/ 6-311+G(d,p)	LanL2DZ/ 6-311+G(3df,p)	LanL2DZ/ 6-311+G(d,p)	LanL2DZ/ 6-311+G(3df,p)
<u>Distance / Å</u>				
S – Fe	3.27	3.25	3.46	3.49
S – O	1.48	1.46	1.50 (±0.02)	1.48 (±0.02)
S – O(Fe)	1.51	1.49	1.51	1.49
(S)O – Fe	2.03	2.03	2.12	2.14
Fe – Fe*[a]	3.08	3.02	3.00	2.95
Fe – O*[b]	2.03 (±0.04)	2.01 (±0.03)	1.98 (±0.05)	1.96 (±0.05)
<u>Angle / degrees</u>				
S – O – Fe	134.5	134.1	144.7	147.3
O – Fe – O*	78.8	80.3	81.2	82.6
Fe – O – Fe*	98.9	97.4	98.8	97.4

[a] Experimental bulk Fe-Fe interatomic distances in Fe-(hydr)oxides along single, edge-sharing dioctahedral chains range from approximately 2.96 – 3.07 Å.

[b] Experimental bulk Fe-O and Fe-O(H) bonds bridging two Fe^{3+} octahedra range from approximately 1.89 – 2.12 Å [52].

Table 4.2 Geometry-optimized bidentate bridging and monodentate sulfate complexes on a hydrated (100) α-FeOOH surface slab. Interatomic distances are reported in angstroms (Å) and bond angles in degrees. * denotes local interatomic distances and angles within the Fe-O-Fe-O ring between 2 edge-sharing Fe^{3+} octahedra coordinated to sulfate (monodentate values are averaged from two pairs of adjacent edge-sharing Fe^{3+} octahedra).

	Bidentate SO_4^{2-}		**Monodentate SO_4^{2-}**	
	SP-PBE	SP-PBE+U	SP-PBE	SP-PBE+U
Distance / Å				
S – Fe	3.29	3.29	3.48	3.47
S – O	1.49	1.49	1.50 (± 0.01)	1.50 (± 0.01)
S – O(Fe)	1.49	1.49	1.48	1.48
(S)O – Fe	2.16	2.15	2.18	2.16
Fe – Fe*, [a]	2.99	2.99	3.02	3.02
Fe – O*, [b]	2.03 (± 0.05)	2.03 (± 0.04)	2.04 (± 0.06)	2.04 (± 0.05)
Angle / degrees				
S – O – Fe	127.5	128.0	142.9	143.5
O – Fe – O*	84.7	85.0	83.7 (± 0.3)	84.1 (± 0.4)
Fe – O – Fe*	95.2	95.1	95.9 (± 3.6)	95.7 (± 3.1)

[a] Experimental bulk Fe-Fe interatomic distances in Fe-(hydr)oxides along single, edge-sharing dioctahedral chains range from approximately 2.96 – 3.07 Å.

[b] Experimental bulk Fe-O and Fe-O(H) bonds bridging two Fe^{3+} octahedra range from approximately 1.89 – 2.12 Å [52].

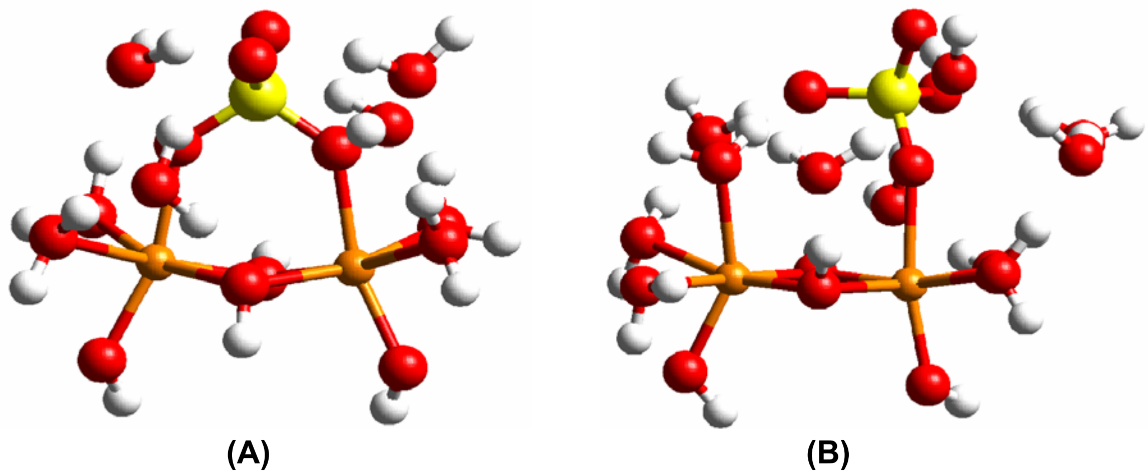

Figure 4.1 Geometry-optimized inner-sphere sulfate complexes on edge-sharing dioctahedral Fe^{3+} cluster models: (A) bidentate bridging sulfate ($Fe_2(OH)_4(OH_2)_4SO_4\cdot(H_2O)_4$) and (B) monodentate sulfate ($Fe_2(OH)_4(OH_2)_5SO_4\cdot(H_2O)_6$). Explicit H_2O molecules are H-bonded to the sulfate complexes. Red, oxygen; white, hydrogen; yellow, sulfur; orange, iron.

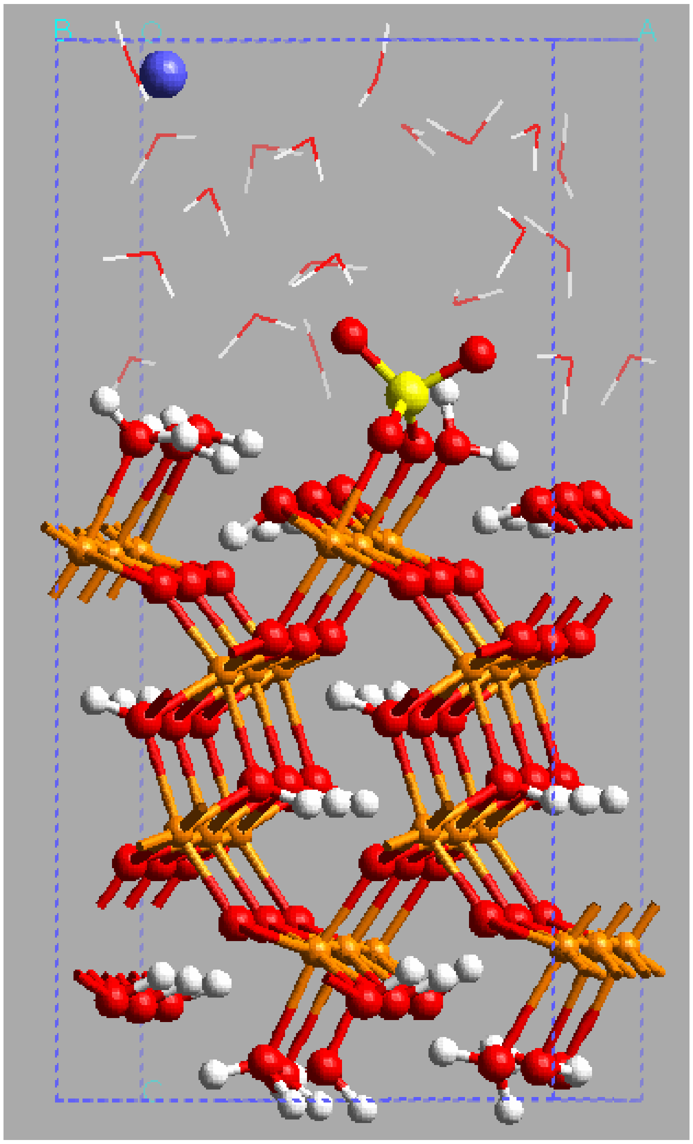

Figure 4.2 Geometry-optimized inner-sphere bidentate bridging sulfate complex on a hydrated (100) α-FeOOH surface slab. Red, oxygen; white, hydrogen; yellow, sulfur; orange, iron; blue, calcium. Explicit H_2O molecules are represented in stick form.

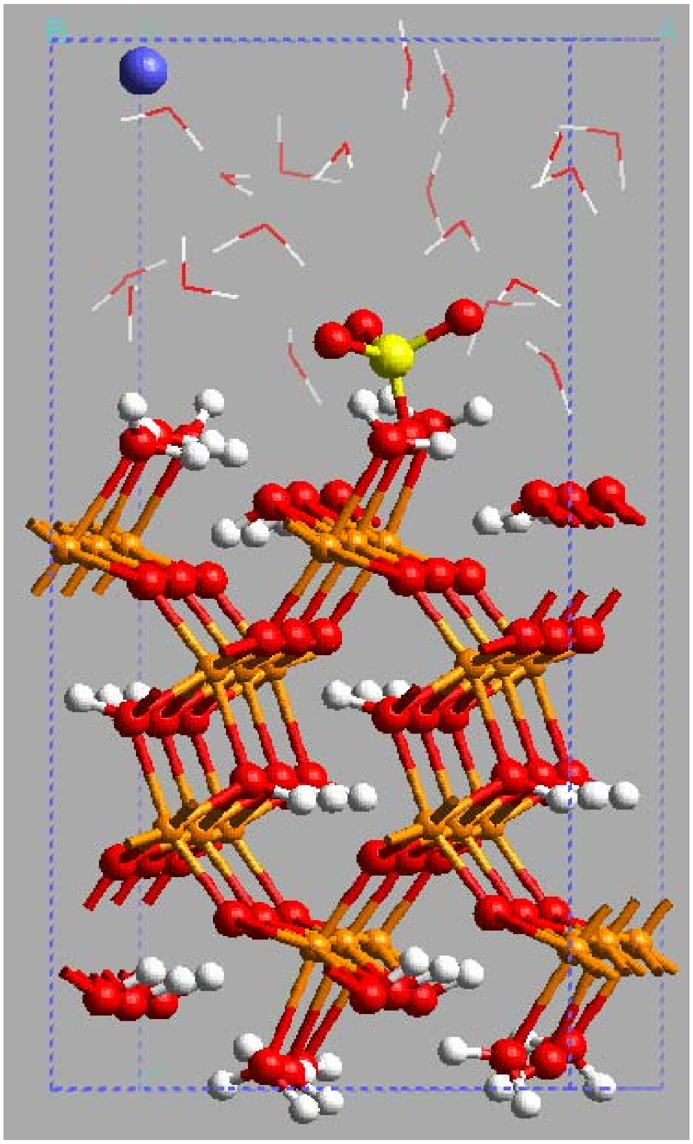

Figure 4.3 Geometry-optimized inner-sphere monodentate sulfate complex on a hydrated (100) α-FeOOH surface slab. Red, oxygen; white, hydrogen; yellow, sulfur; orange, iron; blue, calcium. Explicit H_2O molecules are represented in stick form.

One notable discrepancy between the cluster and periodic slab DFT predictions was the average (S)O–Fe bond distance of bidentate bridging sulfate. The average (S)O–Fe bond distance predicted by the edge-sharing dioctahedral Fe^{3+}

cluster model was 2.03 Å (Table 4.1). On the other hand, the average (S)O–Fe bond distance predicted by the periodic (100) α-FeOOH slab model was 2.15 – 2.16 Å (Table 4.2). This significant disagreement was probably related to differences in the treatment of hydration. For the geometry optimization of bidentate bridging sulfate on the edge-sharing dioctahedral Fe^{3+} cluster model (Figure 4.1(A)), only four explicit H_2O molecules were included. Conversely, 20 explicit H_2O molecules were included in the (100) α-FeOOH slab model, corresponding to a density of approximately 0.95 g cm^{-3} (Figure 4.2). In the latter model, the sulfate complex was completely hydrated. The effects of explicit and implicit solvation on the DFT-predicted (S)O–Fe bond distances of bidentate bridging sulfate will be discussed shortly.

Tables 4.1 and 4.2 also list the predicted interatomic distances and angles within the Fe–O–Fe–O ring between two edge-sharing Fe^{3+} octahedra, which are qualitatively comparable to bulk EXAFS and X-ray diffraction measurements. Measurements of Fe–Fe interatomic distances in Fe-(hydr)oxide minerals are generally associated with dioctahedral Fe^{3+} chains (and single octahedral Fe^{3+} chains) along, across, and between the neighboring chains [52]. The Fe–Fe interatomic distance measured along a dioctahedral Fe^{3+} chain ranges from approximately 2.96 to 3.07 Å, while the Fe–Fe interatomic distance measured across a dioctahedral Fe^{3+} chain ranges from approximately 3.29 to 3.31 Å [52]. The Fe–Fe interatomic distance measured between neighboring dioctahedral Fe^{3+} chains ranges from approximately 3.36 to 4.00 Å (e.g. corner-sharing Fe^{3+} octahedra). The Fe–O and Fe–O(H) bonds bridging two Fe^{3+} octahedra range from approximately 1.89 to 2.12 Å (exceptions include β-FeOOH and ferrihydrite) [52].

As previously mentioned, the average Fe–O* bond and Fe–Fe* interatomic distances predicted by the edge-sharing dioctahedral Fe^{3+} cluster models (Table 4.1) are qualitatively comparable to bulk EXAFS and X-ray diffraction measurements [52]. For example, the predicted average Fe–O* bond distance for the bidentate bridging sulfate complex was 2.01 – 2.03 Å (Table 4.1), within the experimentally measured range of approximately 1.89 – 2.12 Å. Likewise, the predicted Fe–Fe* interatomic distance was 3.02 – 3.08 Å (Table 4.1), within and slightly outside the upper limit of the experimentally measured range of approximately 2.96 – 3.07 Å, respectively.

The slightly longer predicted Fe–Fe* interatomic distance of 3.08 Å (Table 4.1, LanL2DZ/6-311+G(d,p)) was probably related to the coordination of bidentate bridging sulfate and the size of the basis set. To test the effect of basis set size on the predicted Fe–Fe* interatomic distance, the bidentate bridging sulfate cluster model was also geometry-optimized with the LanL2DZ/6-311+G(3df,p) basis set combination (two additional d-polarization functions and one f-polarization function added to the S and O atoms). Geometry optimization of the bidentate bridging sulfate cluster model using the LanL2DZ/6-311+G(3df,p) basis set combination indeed reduced the Fe–Fe* interatomic distance by 0.06 Å (Table 4.1), within the experimentally measured range of approximately 2.96 – 3.07 Å. It is important to note, however, that the LanL2DZ/6-311+G(3df,p) basis set combination did not significantly affect the predicted first shell (S–O and S–O(Fe)), second shell (S–Fe), and (S)O–Fe bond and interatomic distances. Recall that the second shell interatomic distance is an important diagnostic feature of the binding geometry of an oxyanion complex, as determined from an EXAFS measurement.

The average local Fe–O* bond and Fe–Fe* interatomic distances predicted by the (100) α-FeOOH slab model (Table 4.2) for bidentate bridging sulfate also agreed with experimentally measured values [52]. The predicted average Fe–O* bond and Fe–Fe* interatomic distances were 2.03 and 2.99 Å, within the experimentally measured ranges of approximately 1.89 – 2.12 Å and 2.96 – 3.07 Å, respectively (Table 4.2). Furthermore, the cluster (Table 4.1, LanL2DZ/6-311+G(3df,p)) and periodic slab (Table 4.2) DFT predictions of the average Fe–O* bond and Fe–Fe* interatomic distances were also in good agreement (differences < 0.03 Å). The predicted average Fe–O–Fe* and O–Fe–O* bond angles for the cluster and periodic slab DFT calculations agreed to within approximately 2.5 – 6º (Tables 4.1 and 4.2).

Overall, the cluster and periodic slab DFT predictions of the interatomic distances and angles of monodentate sulfate were in good agreement. For example, the predicted second shell S–Fe interatomic distances agreed to within 0.02 Å (Tables 4.1 and 4.2). In addition, the predicted first shell S–O and S–O(Fe) bond distances agreed to within 0.02 – 0.03 Å (Tables 4.1 and 4.2). Similar to bidentate bridging sulfate, the (S)O–Fe bond distances predicted by the DFT cluster models were slightly shorter than those predicted by the periodic slab DFT models. It should be noted, however, that the (S)O–Fe bond distance predicted by the LanL2DZ/6-311+G(3df,p) basis set combination (2.14 Å, Table 4.1) was only 0.02 Å shorter than the (S)O–Fe bond distance predicted by the SP-PBE+U calculation (2.16 Å, Table 4.2).

The average Fe–O* bond and Fe–Fe* interatomic distances predicted by the edge-sharing dioctahedral Fe^{3+} cluster and periodic (100) α-FeOOH slab models for monodentate sulfate were in reasonable agreement and generally within experimentally measured ranges (Tables 4.1 and 4.2). The predicted average Fe–O* bond distances agreed to within 0.06 – 0.08 Å (Tables 4.1 and 4.2), and were within the experimentally measured range of approximately 1.89 – 2.12 Å [52]. The predicted Fe–Fe* interatomic distances agreed to within 0.02 – 0.07 Å (Tables 4.1 and 4.2). Interestingly, the Fe–Fe* interatomic distance predicted by the LanL2DZ/6-311+G(3df,p) DFT cluster model calculation (2.95 Å, Table 4.1) was 0.01 Å shorter than the lower limit of the experimentally measured range of approximately 2.96 – 3.07 Å. This may suggest that the slightly longer Fe–Fe* interatomic distance discussed for bidentate bridging sulfate was related to both the coordination of the adsorption complex and the basis set size. The predicted average O–Fe–O* and Fe–O–Fe* bond angles for the cluster and periodic slab DFT models agreed to within 2.9° and 3.1°, respectively (Tables 4.1 and 4.2).

A particularly noteworthy characteristic of the geometry-optimized monodentate sulfate complex was its S–O–Fe bond angle. The S–O–Fe bond angle was predicted to be significantly less than 180° by both the cluster and periodic slab DFT calculations (Tables 4.1 and 4.2). A monodentate sulfate complex is generally assumed to adopt C_{3v} point group symmetry. In principle, therefore, monodentate sulfate ought to exhibit three IR-active vibrational modes: one ν_1 symmetric stretching mode and two ν_3 asymmetric stretching modes ([53] and references therein). The assumption of a C_{3v} point group restricts the S–O–Fe bond angle to 180°. However, the cluster and periodic slab DFT predictions indicated that monodentate sulfate could form S–O–Fe bond angles less than 180°, thereby adopting lower point group symmetry (within the constraints of a static configuration). P–O–Fe bond angles significantly less than 180° have also been predicted for monodentate phosphate complexes, using DFT cluster model calculations [3]. It is quite possible, however, that a monodentate sulfate complex freely rotates about its (S)O–Fe bond at room temperature and approximately maintains C_{3v} point group symmetry.

The effect of hydration on the predicted interatomic distances and bond angles of bidentate bridging and monodentate sulfate was tested by performing DFT cluster model calculations that included 10 explicit H_2O molecules (Table 4.3, LanL2DZ/6-311+G(d,p)). The corresponding geometry-optimized cluster models are displayed in Figure 4.4. In addition, the bidentate bridging sulfate cluster model displayed in Figure 4.1(A) (four explicit H_2O molecules) was geometry-optimized with the IEFPCM method (Table 4.3). For this particular cluster model, therefore, both explicit and implicit solvation was considered. The predicted average bidentate bridging sulfate (S)O–Fe bond distance increased from 2.03 Å (four explicit H_2O molecules) to 2.09 Å when the geometry optimization was performed with 10 explicit H_2O molecules (Tables 4.1 and 4.3). The predicted average bidentate bridging sulfate (S)O–Fe bond distance of 2.09 Å was significantly closer to the values predicted by the periodic slab DFT calculations (2.15 –2.16 Å, Table 4.2).

Interestingly, the identical effect was also observed when the geometry optimization included four explicit H_2O molecules and implicit solvation with the IEFPCM method (Table 4.3). Hence, the number of explicit H_2O molecules and/or inclusion of implicit solvation significantly influenced the predicted average (S)O–Fe bond distance. It should be noted, however, that the remaining predicted interatomic distances and bond angles of bidentate bridging sulfate were not significantly affected by an increase in the number of explicit H_2O molecules and/or inclusion of implicit solvation. In a previous investigation, the predicted (Si)O–Fe bond distances of bidentate bridging $H_2SiO_4^{2-}$ on an edge-sharing dioctahedral Fe^{3+} cluster model were also shown to be sensitive to the number of explicit H_2O molecules [54].

Table 4.3 Explicit and implicit solvation effects on the interatomic distances and bond angles of geometry-optimized bidentate bridging and monodentate sulfate complexes on edge-sharing dioctahedral Fe^{3+} cluster models. Interatomic distances are reported in angstroms (Å) and bond angles in degrees. * denotes interatomic distances and angles within the Fe-O-Fe-O ring between the two edge-sharing Fe^{3+} octahedra coordinated to sulfate.

	Bidentate SO_4^{2-}		**Monodentate SO_4^{2-}**
	10 Explicit H_2O Molecules	IEFPCM[c]	10 Explicit H_2O Molecules
Distance / Å			
S – Fe	3.30	3.32	3.40
S – O	1.50	1.49	1.50
S – O(Fe)	1.50	1.51	1.50
(S)O – Fe	2.09	2.09	2.11
Fe – Fe*, [a]	3.08	3.08	2.96
Fe – O*, [b]	2.03 (± 0.04)	2.02 (± 0.04)	1.99 (± 0.03)
Angle / degrees			
S – O – Fe	133.2	133.6	140.3
O – Fe – O*	80.0	79.0	82.0
Fe – O – Fe*	98.8	99.7	96.2

[a] Experimental bulk Fe-Fe interatomic distances in Fe-(hydr)oxides along single, edge-sharing dioctahedral chains range from approximately 2.96 – 3.07 Å.

[b] Experimental bulk Fe-O and Fe-O(H) bonds bridging two Fe^{3+} octahedra range from approximately 1.89 – 2.12 Å [52].

[c] Cluster model from Figure 4.1(A) geometry-optimized with the IEFPCM method.

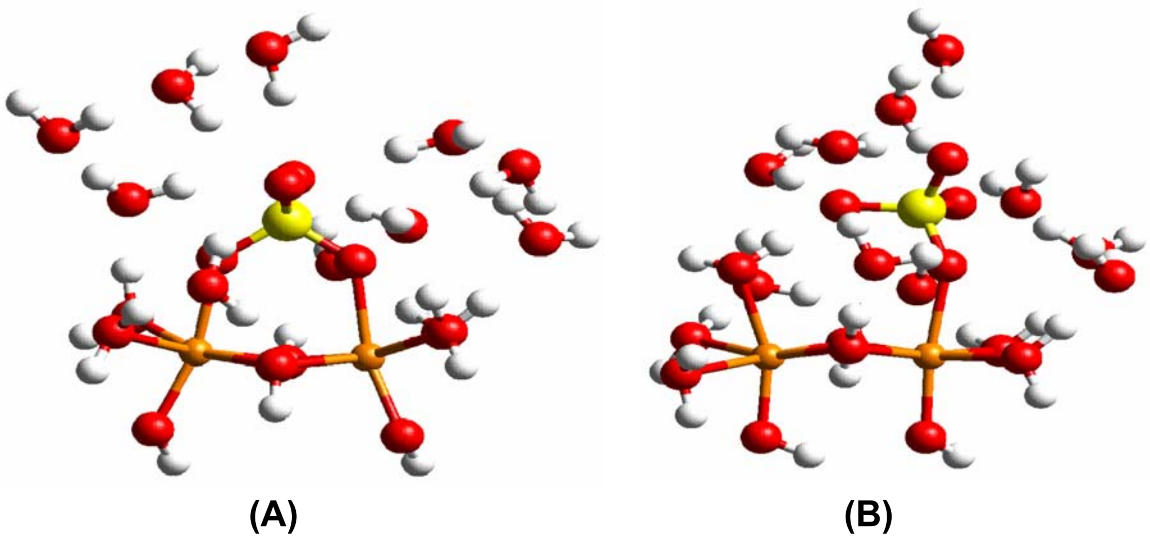

Figure 4.4 Geometry-optimized inner-sphere sulfate complexes on edge-sharing dioctahedral Fe^{3+} cluster models: (A) bidentate bridging sulfate ($Fe_2(OH)_4(OH_2)_4SO_4{\cdot}(H_2O)_{10}$) and (B) monodentate sulfate ($Fe_2(OH)_4(OH_2)_5SO_4{\cdot}(H_2O)_{10}$). Explicit H_2O molecules are H-bonded to the sulfate complexes. Red, oxygen; white, hydrogen; yellow, sulfur; orange, iron.

A few differences were noted when the monodentate sulfate complex was geometry-optimized with six versus 10 explicit H_2O molecules (Tables 4.1 and 4.3). The predicted monodentate sulfate (S)O–Fe bond distance was actually unaffected by an increase in the number of explicit H_2O molecules, in contrast to the bidentate bridging complex (Tables 4.1 and 4.3). Including six explicit H_2O molecules in the DFT geometry optimization may have been sufficient to describe the (S)O–Fe bond distance of monodentate sulfate. On the other hand, the predicted monodentate sulfate S–Fe interatomic distance and S–O–Fe bond angle were affected by an increase in the number of explicit H_2O molecules. The S–Fe interatomic distance and S–O–Fe bond angle decreased from 3.46 to 3.40 Å and 144.7 to 140.3º, respectively, when increasing the number of explicit H_2O molecules by four (Tables 4.1 and 4.3). It is reasonable to assume that the monodentate sulfate S–Fe interatomic distance and S–O–Fe bond angle exhibit significant variability due to the rotational flexibility of monodentate complexes.

4.5 Conclusions

Static DFT calculations were performed with edge-sharing dioctahedral Fe^{3+} cluster models and a periodic slab model of the (100) α-FeOOH surface to predict the binding geometries of monodentate and bidentate bridging sulfate complexes. The edge-sharing dioctahedral Fe^{3+} cluster models closely resembled the local structure and composition of the (100) α-FeOOH surface. Interatomic distances and bond angles predicted by the cluster and periodic slab DFT calculations exhibited good agreement, despite the lack of long-range order in the cluster models. Furthermore, the second shell S–Fe interatomic distances predicted for the bidentate bridging and monodentate sulfate complexes were significantly different (ca. 0.1 – 0.2 Å). Therefore, EXAFS measurements should be able to distinguish between bidentate bridging and monodentate sulfate complexes, at least on the (100) α-FeOOH surface.

Previous studies have shown that DFT cluster model calculations of As(V) [4, 6] and As(III) [7] complexes accurately predicted first and second shell interatomic distances, as measured by EXAFS experiments. There are probably two principal explanations as to why the DFT cluster model calculations accurately predicted the first and second shell interatomic distances of As(V) and As(III) complexes. First, EXAFS spectroscopy probes the local structure of an adsorption complex and the cluster models are intrinsically local (i.e., lack long-range order). Second, as shown by this investigation, the interatomic distances and bond angles predicted by DFT cluster models agree well with similar (i.e., structure and composition) periodic slab DFT models. In other words, including long-range order may not be prerequisite to successfully modeling the binding geometries of oxyanion complexes at the mineral-H_2O interface.

An investigation is currently underway to analyze the cluster and periodic slab DFT predictions presented here, with respect to calculating theoretical photoelectron scattering phase shifts and amplitudes necessary for EXAFS fitting. It is important to restate that the predicted interatomic distances and bond angles were derived from geometry optimizations performed on static configurations. At room temperature, the predicted interatomic distances and bond angles will exhibit variability. This variability, however, can be estimated with quantum molecular dynamics (QMD) simulations. Constant temperature QMD simulations of inner-sphere sulfate complexes are currently in progress (see Chapter 5).

4.6 References

1. Sparks, D. L., *Environmental Soil Chemistry*. 2nd ed.; Academic Press: San Diego, CA, 2003.

2. Brown, G. E.; Sturchio, N. C., An Overview of Synchrotron Radiation Applications to Low Temperature Geochemistry and Environmental Science. In *Applications of Synchrotron Radiation in Low-Temperature Geochemistry and Environmental Sciences*, 2002; Vol. 49, pp 1-115.

3. Kwon, K. D.; Kubicki, J. D., Molecular Orbital Theory Study on Surface Complex Structures of Phosphates to Iron Hydroxides: Calculation of Vibrational Frequencies and Adsorption Energies. *Langmuir* **2004,** *20*, (21), 9249-9254.

4. Ladeira, A. C. Q.; Ciminelli, V. S. T.; Duarte, H. A.; Alves, M. C. M.; Ramos, A. Y., Mechanism of Anion Retention from EXAFS and Density Functional Calculations: Arsenic (V) Adsorbed on Gibbsite. *Geochimica Et Cosmochimica Acta* **2001,** *65*, (8), 1211-1217.

5. Paul, K. W.; Borda, M. J.; Kubicki, J. D.; Sparks, D. L., Effect of Dehydration on Sulfate Coordination and Speciation at the Fe-(hydr)oxide-Water Interface: A Molecular Orbital/Density Functional Theory and Fourier Transform Infrared Spectroscopic Investigation. *Langmuir* **2005,** *21*, (24), 11071-11078.

6. Sherman, D. M.; Randall, S. R., Surface Complexation of Arsenic (V) to Iron (III) (hydr)oxides: Structural Mechanism from *Ab Initio* Molecular Geometries and EXAFS Spectroscopy. *Geochimica Et Cosmochimica Acta* **2003,** *67*, (22), 4223-4230.

7. Zhang, N. L.; Blowers, P.; Farrell, J., Evaluation of Density Functional Theory Methods for Studying Chemisorption of Arsenite on Ferric Hydroxides. *Environmental Science and Technology* **2005,** *39*, (13), 4816-4822.

8. Bargar, J. R.; Kubicki, J. D.; Reitmeyer, R.; Davis, J. A., ATR-FTIR Spectroscopic Characterization of Coexisting Carbonate Surface Complexes on Hematite. *Geochimica Et Cosmochimica Acta* **2005,** *69*, (6), 1527-1542.

9. Persson, P.; Axe, K., Adsorption of Oxalate and Malonate at the Water-Goethite Interface: Molecular Surface Speciation from IR Spectroscopy. *Geochimica Et Cosmochimica Acta* **2005,** *69*, (3), 541-552.

10. Yoon, T. H.; Johnson, S. B.; Musgrave, C. B.; Brown, G. E., Adsorption of Organic Matter at Mineral/Water Interfaces: I. ATR-FTIR Spectroscopic and Quantum Chemical Study of Oxalate Adsorbed at Boehmite/Water and Corundum/Water Interfaces. *Geochimica Et Cosmochimica Acta* **2004,** *68*, (22), 4505-4518.

11. Tribe, L.; Kwon, K. D.; Trout, C. C.; Kubicki, J. D., Molecular Orbital Theory Study on Surface Complex Structures of Glyphosate on Goethite: Calculation of Vibrational Frequencies. *Environmental Science and Technology* **2006,** *40*, (12), 3836-3841.

12. Omoike, A.; Chorover, J.; Kwon, K. D.; Kubicki, J. D., Adhesion of Bacterial Exopolymers to α-FeOOH: Inner-Sphere Complexation of Phosphodiester Groups. *Langmuir* **2004,** *20*, (25), 11108-11114.

13. Baltrusaitis, J.; Jensen, J. H.; Grassian, V. H., FTIR Spectroscopy Combined with Isotope Labeling and Quantum Chemical Calculations to Investigate Adsorbed Bicarbonate Formation Following Reaction of Carbon Dioxide with Surface Hydroxyl Groups on Fe_2O_3 and Al_2O_3. *Journal of Physical Chemistry B* **2006,** *110*, (24), 12005-12016.

14. Gaboriaud, F.; Ehrhardt, J. J., Effects of Different Crystal Faces on the Surface Charge of Colloidal Goethite (α-FeOOH) Particles: An Experimental and Modeling Study. *Geochimica et Cosmochimica Acta* **2003,** *67*, 967-983.

15. Sainz-Diaz, C. I.; Timon, V.; Botella, V.; Hernandez-Laguna, A., Isomorphous Substitution Effect on the Vibration Frequencies of Hydroxyl Groups in Molecular Cluster Models of the Clay Octahedral Sheet. *American Mineralogist* **2000,** *85*, (7-8), 1038-1045.

16. Manning, B. A.; Fendorf, S. E.; Goldberg, S., Surface Structures and Stability of Arsenic(III) on Goethite: Spectroscopic Evidence for Inner-Sphere Complexes. *Environmental Science and Technology* **1998,** *32*, (16), 2383-2388.

17. Watanabe, H.; Gutleben, C. D.; Seto, J., Sulfate-Ions on the Surface of Maghemite and Hematite. *Solid State Ionics* **1994,** *69*, (1), 29-35.

18. Hug, S. J., *In Situ* Fourier Transform Infrared Measurements of Sulfate Adsorption on Hematite in Aqueous Solutions. *Journal of Colloid and Interface Science* **1997,** *188*, (2), 415-422.

19. Peak, D.; Ford, R. G.; Sparks, D. L., An *In Situ* ATR-FTIR Investigation of Sulfate Bonding Mechanisms on Goethite. *Journal of Colloid and Interface Science* **1999,** *218*, (1), 289-299.

20. Wijnja, H.; Schulthess, C. P., Vibrational Spectroscopy Study of Selenate and Sulfate Adsorption Mechanisms on Fe and Al (hydr)oxide Surfaces. *Journal of Colloid and Interface Science* **2000,** *229*, (1), 286-297.

21. Turner, L. J.; Kramer, J. R., Sulfate Ion Binding on Goethite and Hematite. *Soil Science* **1991,** *152*, (3), 226-230.

22. Parfitt, R. L.; Smart, R. S. C., The Mechanism of Sulfate Adsorption on Iron Oxides. *Soil Science Society of America Journal* **1978,** *42*, (1), 48-50.

23. Parfitt, R. L.; Smart, R. S. C., Infrared Spectra from Binuclear Bridging Complexes of Sulfate Adsorbed on Goethite (α-FeOOH). *Journal of the Chemical Society-Faraday Transactions I* **1977,** *73*, 796-802.

24. Harrison, J. B.; Berkheiser, V. E., Anion Interactions with Freshly Prepared Hydrous Iron Oxides. *Clays and Clay Minerals* **1982,** *30*, (2), 97-102.

25. Sposito, G., On Points of Zero Charge. *Environmental Science and Technology* **1998,** *32*, (19), 2815-2819.

26. Myneni, S. C. B.; Traina, S. J.; Waychunas, G. A.; Logan, T. J., Experimental and Theoretical Vibrational Spectroscopic Evaluation of Arsenate Coordination in Aqueous Solutions, Solids, and at Mineral-Water Interfaces. *Geochimica Et Cosmochimica Acta* **1998,** *62*, (19-20), 3285-3300.

27. Cances, E.; Mennucci, B.; Tomasi, J., A New Integral Equation Formalism for the Polarizable Continuum Model: Theoretical Background and Applications to Isotropic and Anisotropic Dielectrics. *Journal of Chemical Physics* **1997,** *107*, (8), 3032-3041.

28. Frisch, M. J., Trucks, G. W., Schlegel, H. B., Scuseria, G. E., Robb, M. A., Cheeseman, J. R., Montgomery, Jr., J. A., Vreven, T., Kudin, K. N., Burant, J. C., Millam, J. M., Iyengar, S. S., Tomasi, J., Barone, V., Mennucci, B., Cossi, M., Scalmani, G., Rega, N., Petersson, G. A., Nakatsuji, H., Hada, M., Ehara, M., Toyota, K., Fukuda, R., Hasegawa, J., Ishida, M., Nakajima, T., Honda, Y., Kitao, O., Nakai, H., Klene, M., Li, X., Knox, J. E., Hratchian, H. P., Cross, J. B., Bakken, V., Adamo, C., Jaramillo, J., Gomperts, R., Stratmann, R. E., Yazyev, O., Austin, A. J., Cammi, R., Pomelli, C., Ochterski, J. W., Ayala, P. Y., Morokuma, K., Voth, G. A., Salvador, P., Dannenberg, J. J., Zakrzewski, V. G., Dapprich, S., Daniels, A. D., Strain, M. C., Farkas, O., Malick, D. K., Rabuck, A. D., Raghavachari, K., Foresman, J. B., Ortiz, J. V., Cui, Q., Baboul, A. G., Clifford, S., Cioslowski, J., Stefanov, B. B., Liu, G., Liashenko, A., Piskorz, P., Komaromi, I., Martin, R. L., Fox, D. J., Keith, T., Al-Laham, M. A., Peng, C. Y., Nanayakkara, A., Challacombe, M., Gill, P. M. W., Johnson, B., Chen, W., Wong, M. W., Gonzalez, C., and Pople, J. A. *Gaussian 03, revision B.05; Gaussian, Inc.;*, Wallingford CT, 2004.

29. Perdew, J. P.; Burke, K.; Ernzerhof, M., Generalized Gradient Approximation Made Simple. *Physical Review Letters* **1996,** *77*, (18), 3865-3868.

30. Hay, P. J.; Wadt, W. R., *Ab Initio* Effective Core Potentials for Molecular Calculations - Potentials for the Transition-Metal Atoms Sc to Hg. *Journal of Chemical Physics* **1985,** *82*, (1), 270-283.

31. Paul, K. W.; Kubicki, J. D.; Sparks, D. L., Quantum Chemical Calculations of Sulfate Adsorption at the Al- and Fe-(Hydr)oxide-H_2O Interface-Estimation of Gibbs Free Energies. *Environmental Science and Technology* **2006,** *40*, (24), 7717-7724.

32. Szytula, A.; Burewicz, A.; Dimitrij.Z; Krasnick.S; Rzany, H.; Todorovi.J; Wanic, A.; Wolski, W., Neutron Diffraction Studies of Alpha-FeOOH. *Physica Status Solidi* **1968,** *26*, (2), 429-434.

33. Hahn, T., ed, *International Tables of Crystallography*. Kluwer Academic Publishers: Norwell, MA, 1996.

34. Cornell, R. M.; Posner, A. M.; Quirk, J. P., Crystal Morphology and the Dissolution of Goethite. *Journal of Inorganic and Nuclear Chemistry* **1974,** *36*, (9), 1937-1946.

35. Kresse, G.; Furthmuller, J., Efficient Iterative Schemes for *Ab Initio* Total-Energy Calculations Using a Plane-Wave Basis Set. *Physical Review B* **1996,** *54*, (16), 11169-11186.

36. Kresse, G.; Furthmuller, J., Efficiency of Ab-Initio Total Energy Calculations for Metals and Semiconductors Using a Plane-Wave Basis Set. *Computational Materials Science* **1996,** *6*, (1), 15-50.

37. Kohn, W.; Sham, L. J., Self-Consistent Equations Including Exchange and Correlation Effects. *Physical Review* **1965,** *140*, A1133-A1138.

38. Pulay, P., Convergence Acceleration of Iterative Sequences. The Case of SCF Iteration. *Chemical Physics Letters* **1980,** *73*, (2), 393-398.

39. Wood, D. M.; Zunger, A., A New Method for Diagonalising Large Matrices. *Journal of Physics A: Mathematical and General* **1985,** *18*, (9), 1343-1359.

40. Blochl, P. E., Projector Augmented-Wave Method. *Physical Review B* **1994,** *50*, (24), 17953-17979.

41. Kresse, G.; Joubert, D., From Ultrasoft Pseudopotentials to the Projector Augmented-Wave Method. *Physical Review B* **1999,** *59*, (3), 1758-1775.

42. Monkhorst, H. J.; Pack, J. D., Special Points for Brillouin-Zone Integrations. *Physical Review B* **1976,** *13*, (12), 5188-5192.

43. Methfessel, M.; Paxton, A. T., High-Precision Sampling for Brillouin-Zone Integration in Metals. *Physical Review B* **1989,** *40*, (6), 3616-3621.

44. Rollmann, G.; Rohrbach, A.; Entel, P.; Hafner, J., First-Principles Calculation of the Structure and Magnetic Phases of Hematite. *Physical Review B* **2004,** *69*, (16), 165107.

45. Rohrbach, A.; Hafner, J.; Kresse, G., Electronic Correlation Effects in Transition-Metal Sulfides. *Journal of Physics: Condensed Matter* **2003,** *15*, (6), 979.

46. Dudarev, S. L.; Botton, G. A.; Savrasov, S. Y.; Humphreys, C. J.; Sutton, A. P., Electron-Energy-Loss Spectra and the Structural Stability of Nickel Oxide: An LSDA+U Study. *Physical Review B* **1998,** *57*, (3), 1505-1509.

47. Eggleston, C. M.; Hug, S.; Stumm, W.; Sulzberger, B.; Afonso, M. D., Surface Complexation of Sulfate by Hematite Surfaces: FTIR and STM Observations. *Geochimica Et Cosmochimica Acta* **1998,** *62*, (4), 585-593.

48. Waychunas, G.; Trainor, T.; Eng, P.; Catalano, J.; Brown, G.; Davis, J.; Rogers, J.; Bargar, J., Surface Complexation Studied via Combined Grazing-Incidence EXAFS and Surface Diffraction: Arsenate an Hematite (0001) and (10-12). *Analytical and Bioanalytical Chemistry* **2005,** *383*, (1), 12-27.

49. Fendorf, S.; Eick, M. J.; Grossl, P.; Sparks, D. L., Arsenate and Chromate Retention Mechanisms on Goethite. 1. Surface Structure. *Environmental Science and Technology* **1997,** *31*, (2), 315-320.

50. Bargar, J. R.; Trainor, T. P.; Fitts, J. P.; Chambers, S. A.; Brown, G. E., *In Situ* Grazing-Incidence Extended X-ray Absorption Fine Structure Study of Pb(II) Chemisorption on Hematite (0001) and (1-102) Surfaces. *Langmuir* **2004,** *20*, (5), 1667-1673.

51. Catalano, J. G.; Trainor, T. P.; Eng, P. J.; Waychunas, G. A.; Brown, J. G. E., CTR Diffraction and Grazing-Incidence EXAFS Study of U(VI) Adsorption onto α-Al_2O_3 and α-Fe_2O_3 (1-102) Surfaces. *Geochimica et Cosmochimica Acta* **2005,** *69*, (14), 3555-3572.

52. Waychunas, G. A.; Fuller, C. C.; Rea, B. A.; Davis, J. A., Wide Angle X-ray Scattering (WAXS) Study of "Two-Line" Ferrihydrite Structure: Effect of Arsenate Sorption and Counterion Variation and Comparison with EXAFS Results. *Geochimica Et Cosmochimica Acta* **1996,** *60*, (10), 1765-1781.

53. Lefevre, G., In Situ Fourier-Transform Infrared Spectroscopy Studies of Inorganic Ions Adsorption on Metal Oxides and Hydroxides. *Advances in Colloid and Interface Science* **2004,** *107*, (2-3), 109-123.

54. Hiemstra, T.; Van Riemsdijk, W. H., On the Relationship Between Charge Distribution, Surface Hydration, and the Structure of the Interface of Metal Hydroxides. *Journal of Colloid and Interface Science* **2006,** *301*, (1), 1-18.

Chapter 5

QUANTUM MOLECULAR DYNAMICS STUDY OF INNER-SPHERE SO_4^{2-} AND HPO_4^{2-} COMPLEXES AT THE (101) GOETHITE-WATER INTERFACE

5.1 Abstract

Room temperature quantum molecular dynamics (QMD) simulations were performed to investigate the dynamical behavior of monodentate and bidentate bridging SO_4^{2-} and HPO_4^{2-} complexes at the (101) α-FeOOH-H_2O interface. At the (101) α-FeOOH-H_2O interface, the monodentate HPO_4^{2-} complex converted to a monodentate PO_4^{3-} complex, but the bidentate bridging HPO_4^{2-} complex remained stable. The monodentate PO_4^{3-} and SO_4^{2-} complexes formed several H-bonds with different OH functional groups on the (101) α-FeOOH surface. The order of H-bonds formed, from strongest to weakest, was as follows: singly coordinated OH_2, μ_3 OH, and singly coordinated OH functional groups. The bidentate bridging HPO_4^{2-} complex formed one H-bond with a μ_3 OH functional group, whereas the bidentate bridging SO_4^{2-} complex formed one H-bond with a μ OH functional group. To investigate the potential role of H^+ in the mechanisms of $H_2PO_4^-$ and HPO_4^{2-} adsorption, several bidentate bridging pathways were modeled with static density functional theory (DFT) cluster calculations. A proton-assisted ligand exchange mechanism was proposed to

explain why $H_2PO_4^-$ and HPO_4^{2-} are stronger competitors than SO_4^{2-} for adsorption sites on bulk α-FeOOH, particularly above pH 4.0.

5.2 Introduction

The biogeochemical cycles of sulfur and phosphorus are of significant environmental, agricultural, and economic importance, as both elements are essential plant nutrients. Sulfur, for example, is a constituent of enzymes that regulate photosynthesis and nitrogen fixation. Phosphorus is a constituent of adenosine triphosphate (ATP), which is the energy source for many metabolic processes in biological systems. In soils, the dominant chemical species of sulfur and phosphorus, available for uptake by plants, are the sulfate and phosphate anions. Despite their vital roles in plant physiology, however, sulfate and phosphate can be associated with severe environmental problems, such as acid mine drainage, acid precipitation, and cultural eutrophication.

The transport and bioavailability of sulfate and phosphate in soils are significantly affected by adsorption to Al-oxides, Fe-oxides, and 1:1 silicate clays (e.g. kaolinite). Accordingly, a molecular-scale understanding of the adsorption mechanisms and kinetics has long been sought. The most extensively investigated soil mineral, with respect to sulfate and phosphate adsorption, has been goethite (α-FeOOH). Goethite is the most thermodynamically stable and abundant Fe-oxyhydroxide in soils. The absolute abundance of α-FeOOH in soils is 1 – 5%.

However, due to its large surface area (approximately 50 – 200 m^2 g^{-1}), α-FeOOH can represent 50 – 70% of the total surface area of a soil [1]. The most prevalent surfaces of α-FeOOH are the (101), (001), and (210) (*Pnma* space group) [2, 3].

Numerous IR vibrational spectroscopic studies have been performed in an attempt to elucidate the binding geometries of sulfate and phosphate complexes on α-FeOOH. In general, the IR measurements were performed either *ex situ* (without H_2O present) or *in situ* (with H_2O present). Based upon *ex situ* studies of sulfate [4-6] and phosphate [7-10] adsorption on α-FeOOH, for example, investigators have proposed the formation of inner-sphere bidentate bridging complexes. Furthermore, a ligand exchange mechanism was proposed, whereby one sulfate or phosphate anion replaced two adjacent singly coordinated OH or OH_2 functional groups. Persson *et al.* [11] also investigated the adsorption of phosphate on α-FeOOH, using *ex situ* IR measurements. In contrast to previous studies, however, Persson *et al.* [11] proposed that phosphate formed diprotonated, monoprotonated, or deprotonated monodentate complexes at low, intermediate, and high pH values, respectively.

By and large, *in situ* and *ex situ* studies of sulfate and phosphate adsorption on α-FeOOH hold opposing views. For example, Peak *et al.* [12] and Wijnja and Schulthess [13] proposed that sulfate formed both outer-sphere and inner-sphere monodentate complexes at the α-FeOOH-H_2O interface. Peak *et al.* [12] proposed a novel mechanism, whereby sulfate forms a continuum of outer- and inner-sphere complexes. Tejedor-Tejedor and Anderson [14] and Luengo *et al.* [15]

investigated the adsorption of phosphate at the α-FeOOH-H_2O interface. Tejedor-Tejedor and Anderson [14] proposed that phosphate formed protonated bidentate bridging, deprotonated bidentate bridging, and deprotonated monodentate complexes, as a function of pH and phosphate concentration. Luengo *et al.* [15] investigated the kinetics of phosphate adsorption and proposed that phosphate formed protonated and deprotonated bidentate bridging complexes, as a function of pH.

Despite the advances achieved in our understanding of the binding geometries of sulfate and phosphate complexes on α-FeOOH, uncertainty remains regarding the adsorption mechanisms. In particular, the pathways of sulfate and phosphate ligand exchange reactions, as well as the competitive adsorption of sulfate and phosphate, are inadequately understood. In this respect, molecular modeling can provide valuable information. For example, Paul *et al.* [16] and Kwon and Kubicki [17] performed density functional theory (DFT) calculations for various sulfate and phosphate complexes. DFT-calculated IR vibrational frequencies were compared with published IR measurements. The DFT calculations were performed with static configurations of edge-sharing dioctahedral Fe^{3+} clusters. Unfortunately, static DFT calculations cannot provide information regarding the dynamical behavior of sulfate and phosphate complexes at the mineral-H_2O interface. Furthermore, a limited number of explicit H_2O molecules were used to simulate hydration.

To date, classical or quantum dynamical simulations of hydrated sulfate and phosphate complexes on periodic surfaces of α-FeOOH have not been performed.

Unfortunately, accurate force fields are generally unavailable to perform classical molecular dynamics (MD) or Monte Carlo simulations. Although quantum molecular dynamics (QMD) simulations are more reliable, such time-consuming simulations of environmentally-relevant systems have only become recently possible (e.g. [18]). Nevertheless, a limited number of classical MD simulations are being performed to investigate the interactions of electrolyte solutions with α-FeOOH surfaces (e.g. [19]). In addition, Aquino *et al.* [20] recently performed quantum chemical calculations of organic contaminant complexes on clusters of the (101) α-FeOOH surface.

In this study, QMD simulations were performed for monodentate and bidentate bridging SO_4^{2-} and HPO_4^{2-} complexes at the (101) α-FeOOH-H_2O interface. The principal objectives of this study were: (1) compare the binding geometries of the SO_4^{2-} and HPO_4^{2-} complexes at the (101) α-FeOOH-H_2O interface; (2) investigate the H-bonding interactions of the SO_4^{2-} and HPO_4^{2-} complexes with OH functional groups on the (101) α-FeOOH surface; (3) investigate the H-bonding interactions of the SO_4^{2-} and HPO_4^{2-} complexes with solvent H_2O molecules. The QMD simulations revealed that the SO_4^{2-} and HPO_4^{2-} complexes uniquely interacted with OH functional groups on the (101) α-FeOOH surface, as well as with solvent H_2O molecules. In this study, DFT cluster calculations were also performed to estimate the energies of potential $H_2PO_4^-$ and HPO_4^{2-} adsorption pathways. To explain why $H_2PO_4^-$ and HPO_4^{2-} are stronger competitors than SO_4^{2-} for adsorption sites on α-FeOOH, we propose a proton-assisted ligand exchange mechanism.

5.3 Computational Methods

5.3.1 Periodic Slab Models

The unit cell of α-FeOOH (*Pnma* space group) was first constructed in Cerius^2 (Accelrys Inc., San Diego, CA) according to the experimental lattice parameters and atomic coordinates published by Szytula *et al.* [21]. The unit cell of α-FeOOH was cleaved through the (101) plane ((110) plane in *Pbnm* space group [22]) to a depth equal to two unit cells. The resulting slab model of the (101) α-FeOOH surface was quasi-cubic with lattice vectors a = 10.9703, b = 9.0300, and c = 8.4896 Å (i.e., 1 x 3 slab model). The (101) α-FeOOH surface was represented equivalently on both sides of the slab model to maximize symmetry and to minimize a dipole moment in the slab.

The periodic images of the (101) α-FeOOH slab model perpendicular to the a-b plane were separated by a vacuum space of 11 Å (c = 19.4896 Å). Cleavage through the (101) plane of α-FeOOH resulted in under-coordinated surface Fe atoms and unsaturated O atoms. The under-coordinated surface Fe atoms and unsaturated O atoms were terminated with OH functional groups and H atoms, respectively. The resulting overall charge of the (101) α-FeOOH slab model was stoichiometrically neutral: $Fe_{24}O_{18}(OH)_{36}$. After the (101) α-FeOOH slab model was terminated with OH functional groups and H atoms, the vacuum space separating periodic images perpendicular to the a-b plane was approximately 10 Å.

At full bond saturation, the (101) α-FeOOH surface possesses three different types of OH functional groups bonded to Fe atoms. For a thorough description of the OH functional groups that occupy the (101) α-FeOOH surface, and their standard IUPAC nomenclature, refer to Aquino *et al.* [20]. Briefly, the OH functional groups bonded to Fe atoms on the (101) α-FeOOH surface are either singly coordinated (OH or OH_2), doubly coordinated (i.e., μ), or triply coordinated (i.e., μ_3). It is important to note, however, that only the singly coordinated OH and OH_2 functional groups are assumed to be involved in ligand exchange reactions with SO_4^{2-} and $H_2PO_4^-/HPO_4^{2-}$.

The starting configurations of the bidentate bridging and monodentate SO_4^{2-} complexes were approximately equal to energy-minimized binding geometries from previous DFT cluster calculations [16, 23]. The vacuum space was filled with explicit H_2O molecules, corresponding to a density of approximately 0.9 – 1.0 g cm^{-3}. To maintain a neutrally-charged simulation cell, two adjacent singly coordinated OH functional groups were protonated (one or two of these singly coordinated OH_2 functional groups were replaced with the monodentate and bidentate bridging SO_4^{2-} and HPO_4^{2-} complexes, respectively). Dipole moment corrections were not applied to the simulation cells. Each system was geometry-optimized prior to the QMD simulations (Section 5.3.2). After the bidentate bridging and monodentate SO_4^{2-} systems were geometry-optimized, the S atom was replaced by a P atom and one of the non-bonded PO_4^{3-} O atoms was protonated to form HPO_4^{2-} complexes. The HPO_4^{2-} systems were also geometry-optimized prior to the QMD simulations.

5.3.2 Quantum Molecular Dynamics Simulations

The QMD simulations were performed with the Vienna *ab initio* simulation package (VASP) [24, 25]. VASP is a DFT program that solves the Kohn-Sham equations [26] with the use of pseudopotentials or the projector-augmented wave method and a plane-wave basis set. To prepare the starting configurations for the QMD simulations, geometry optimizations were performed for each system. The exchange-correlation functional chosen was the spin-polarized generalized gradient approximation (SP-GGA) functional of Perdew *et al.* [27], denoted SP-PBE. The Kohn-Sham equations were solved by minimizing the norm of the residual vector to each eigenstate [28, 29], based upon efficient mixing of the charge density.

The electron-ion interactions were described by the projector-augmented wave method of Blöchl [30], as implemented by Kresse and Joubert [31]. The number of valence electrons treated explicitly for each heavy element was as follows: Fe, $3p^6 3d^7 4s^1$; O, $2s^2 2p^4$; S, $3s^2 3p^4$; P, $3s^2 3p^3$. Sampling of the Brillouin zone was performed automatically through implementation of the Monkhorst-Pack scheme [32] and was restricted to the Γ-point. The plane-wave kinetic energy cutoff was set to 400 eV. A first-order Gaussian smearing coefficient, σ, of 0.10 eV was used for the geometry optimizations [33]. The geometry optimizations were considered completed when the Hellmann-Feynman forces acting on the atoms were less than 0.02 eV Å^{-1}

and the error in total energy was less than 10^{-4} eV. All of the atomic positions were allowed to relax, but the shape and size of the simulation cell were conserved. The number of unpaired valence electrons initially specified for each individual Fe atom corresponded to five (i.e., high-spin state of Fe^{3+}).

The QMD simulations were performed with the SP-PBE exchange-correlation functional within the framework of the SP-GGA+U method. The SP-GGA+U method explicitly considers the on-site Coulomb repulsion for strongly correlated d- and f-electrons. Unfortunately, SP-GGA methods can fail to correctly describe the strong electronic correlations of valence electrons in transition metal atoms. In the SP-GGA+U method, a Hubbard term describing the on-site Coulomb repulsion and exchange interactions is added to the DFT Hamiltonian. Explicit consideration of the on-site Coulomb repulsion has been shown to significantly improve predictions of the local magnetic moments of Fe atoms, band gaps, and band energies for bulk hematite (α-Fe_2O_3) [34]. For a description of the SP-GGA+U method applied to the closely related α-Fe_2O_3 system, refer to Rollmann *et al.* [34]. Furthermore, refer to Rohrbach *et al.* [35] for implementation of the GGA+U method in VASP.

Dudarev's [36] rotationally-invariant approach to the SP-GGA+U method was used in this study. The effective on-site Coulomb and exchange interaction parameters for each Fe atom were set to 4 eV and 1 eV, respectively, as recommended by Rollmann *et al.* [34]. Constant temperature QMD simulations were performed with the *NVT* ensemble at 300 K, using the algorithm of Nosé [37]. The initial frequency of the Nosé thermostat was set to approximately 1600 cm^{-1}. A time step, Δt, of 1 fs was chosen and the simulations ranged between 19.0 and 23.5 ps. The first 7.0 – 11.5 ps were reserved for equilibration of the starting configurations. Thus, the last 12 ps were used for statistical analysis. The equilibration phase was monitored by the temporal evolution of the total energies. For the QMD simulations, the plane-wave kinetic energy cutoff was reduced to 220 eV, which allowed simulations of thousands of time steps to be practical.

5.3.3 DFT Cluster Model Calculations

To determine the potential role of H^+ in the mechanisms of $H_2PO_4^-$ and HPO_4^{2-} adsorption, DFT cluster model calculations were performed. The relative energies of several $H_2PO_4^-$ and HPO_4^{2-} adsorption pathways were estimated, using previously described DFT methods [23]. The DFT calculations were performed with Gaussian 03 [38]. The unrestricted 3-parameter exchange functional of Becke [39] and the gradient-corrected correlation functional of Lee *et al.* [40] were chosen (i.e., UB3LYP method). The CEP-121G [41] relativistic effective core potential basis set was used for the Fe atoms. The high-spin state of Fe^{3+} was specified for each Fe atom. The all-electron 6-31+G(d,p) basis set was used for the P, O, and H atoms.

To estimate the energies of the adsorption pathways, each reactant and product cluster was geometry-optimized in the gas-phase without symmetry or geometrical constraints. Frequency calculations were subsequently performed to determine whether the geometry optimization had successfully located a potential energy minimum (i.e., no imaginary frequencies). It is important to note, however, that only one static configuration was geometry-optimized for each reactant and product cluster. Therefore, the potential energy minima did not likely correspond to the global minima for these configurations. The frequency calculations were also performed to determine the thermal correction to the Gibbs free energy (scaling not taken into account).

Single-point B3LYP/6-311++G(df,pd) energy calculations were performed for each geometry-optimized gas-phase reactant and product cluster, using the Integral Equation Formalism Polarized Continuum Model (IEFPCM) [42] method. Note that the CEP-121G basis set was used for the Fe atoms. The single-point IEFPCM energy calculations provided an estimate of the total free energy in solution, including non-electrostatic terms, for each geometry-optimized reactant and product cluster. The dielectric constant of bulk water ($\varepsilon = 78.4$) was specified for the single-point IEFPCM energy calculations.

5.4 Results and Discussion

In Sections 5.4.1 and 5.4.2, the dynamical behavior of the inner-sphere SO_4^{2-} and HPO_4^{2-} complexes at the (101) α-FeOOH-H_2O interface will be discussed. In particular, the H-bonding interactions of the monodentate and bidentate bridging SO_4^{2-} and HPO_4^{2-} complexes with OH functional groups that occupy the (101) α-

FeOOH surface, as well as with solvent H_2O molecules, will be carefully examined. Note that the majority of partial pair correlation functions, g(r), and bond-angle distribution functions, $g^{(3)}(\theta)$, discussed in Sections 5.4.1 and 5.4.2 were moderately smoothed with the program Origin [43] (i.e., FFT filter smoothing option in program Origin). The monodentate SO_4^{2-} and HPO_4^{2-} complexes at the (101) α-FeOOH-H_2O interface will be discussed first.

5.4.1 Monodentate Complexes

Snapshots from the QMD simulations of the monodentate PO_4^{3-} and SO_4^{2-} complexes at the (101) α-FeOOH-H_2O interface are displayed in Figure 5.1. As discussed below, the monodentate HPO_4^{2-} complex deprotonated and formed a stable monodentate PO_4^{3-} complex. The compositions of the simulation cells, in their entirety, are displayed in Figure 5.1(A) and (C). In Figure 5.1(B) and (D), close-up views of the monodentate PO_4^{3-} and SO_4^{2-} complexes, respectively, are displayed. Selected atoms that are represented as ball-and-stick and/or labeled in Figure 5.1(B) and (D) will be discussed in detail. Specifically, the H-bonding interactions of monodentate PO_4^{3-} with a singly coordinated OH, a singly coordinated OH_2, and two μ_3 OH functional groups will be discussed (Figure 5.1(B)). Likewise, the H-bonding interactions of monodentate SO_4^{2-} with a singly coordinated OH, a singly coordinated OH_2, and one μ_3 OH functional group will be discussed (Figure 5.1(D)). The H-bonding interactions of the monodentate PO_4^{3-} and SO_4^{2-} atoms labeled O_1 – O_3 with solvent H_2O molecules will also be examined.

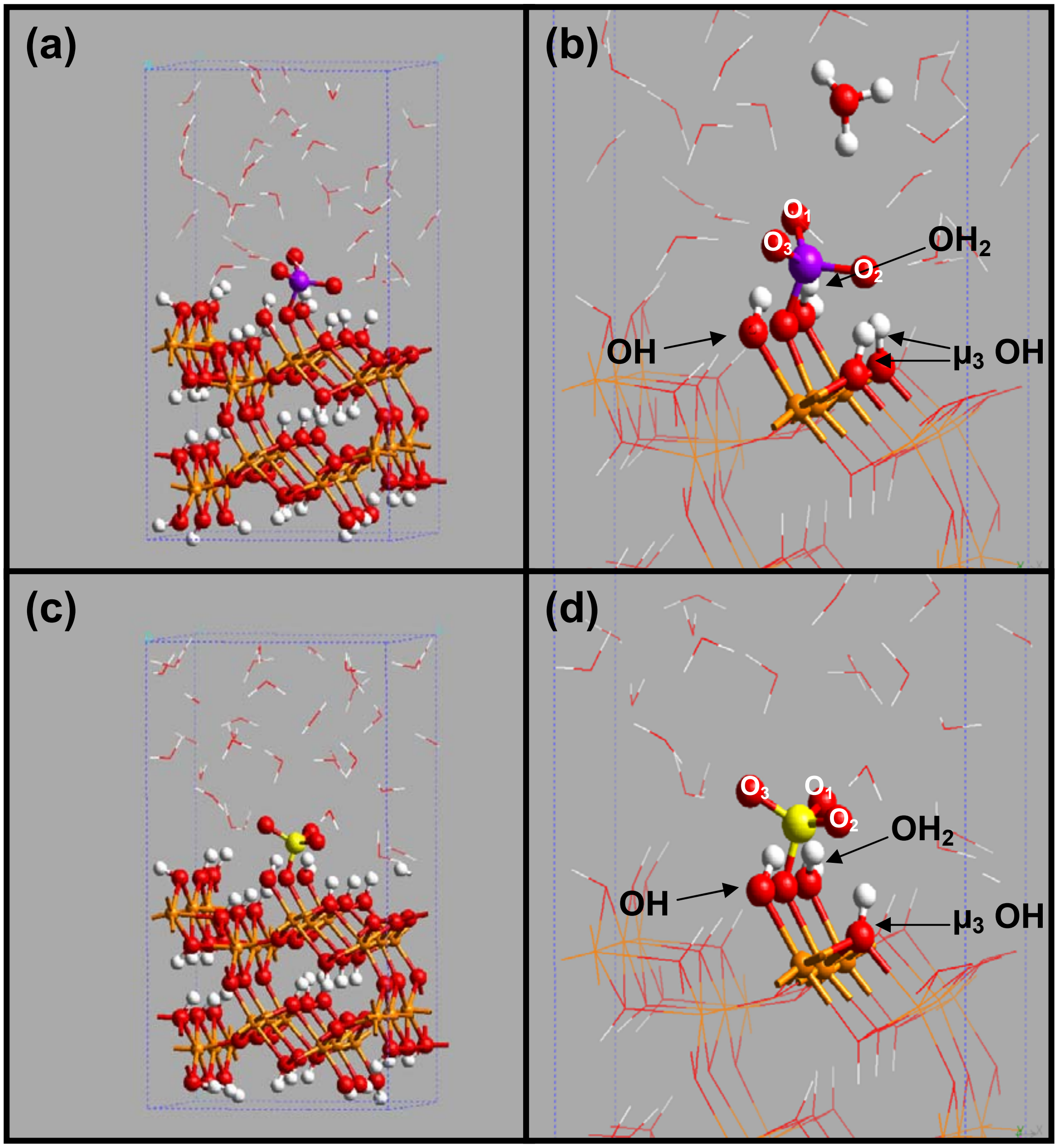

Figure 5.1 Snapshots of the monodentate PO_4^{3-} and SO_4^{2-} complexes at the (101) α-FeOOH-H_2O interface selected from the production phase of the QMD simulations. (A) and (C) display the compositions of the simulation cells for the monodentate PO_4^{3-} and SO_4^{2-} systems, respectively. (B) and (D) display close-up views of the monodentate PO_4^{3-} and SO_4^{2-} complexes, respectively. Selected atoms represented in (B) and (D) as ball-and-stick and/or labeled are discussed in Section 5.4.1. Red, oxygen; white, hydrogen; purple, phosphorus; yellow, sulfur; and orange, iron.

The monodentate HPO_4^{2-} complex participated in several H^+ transfers during the first 3000 fs of the equilibration phase. Ultimately, the monodentate HPO_4^{2-} complex converted to a monodentate PO_4^{3-} complex, which remained stable throughout the entire production phase (i.e., 12 ps). Figure 5.2(A) displays the time evolution of H^+ transfers from monodentate HPO_4^{2-} to a nearby H_2O molecule ($(P)O_2$-$H_1\cdot\cdot\cdot O_3$ – black trajectory), and vice versa (O_3-$H_1\cdot\cdot\cdot O_2(P)$ – red trajectory). Proton transfers between monodentate HPO_4^{2-} and the H_2O molecule correspond to points where the black and red trajectories intersected. All of the labels in Figure 5.2(A) and (B), except O_2 (Figure 5.1(B)), are arbitrary. Within approximately 100 fs, Figure 5.2(A) shows that monodentate HPO_4^{2-} transferred its H^+ to a nearby H_2O molecule. At approximately 500 fs, monodentate PO_4^{3-} accepted the H^+ back from the H_3O^+ molecule. From approximately 500 to 1400 fs, several H^+ transfers occurred between the monodentate HPO_4^{2-} complex and H_2O molecule. Between approximately 1400 and 1900 fs, a monodentate HPO_4^{2-} complex persisted. At approximately 2250 fs, however, the final H^+ transfer occurred from monodentate HPO_4^{2-} to a nearby H_2O molecule. Thereafter, a monodentate PO_4^{3-} complex remained stable throughout the production phase (data are displayed to 3000 fs in Figure 5.2(A) and (B)).

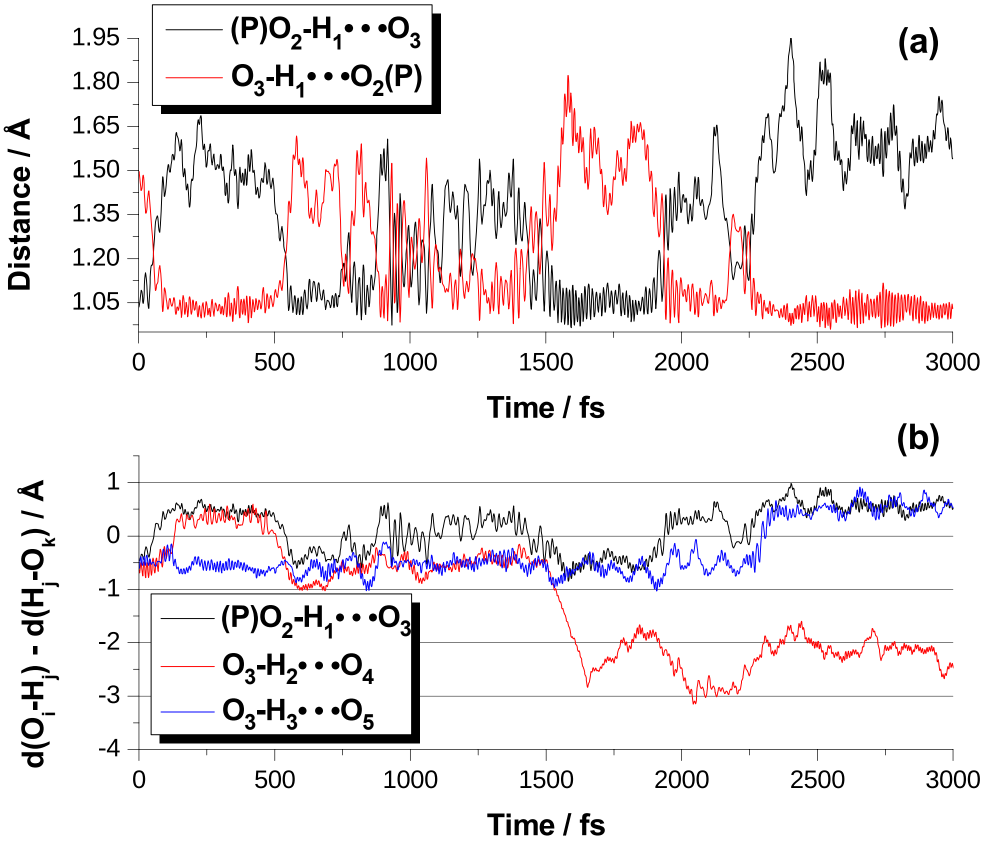

Figure 5.2 (A) Time evolution of H^+ transfers from monodentate HPO_4^{2-} to a nearby H_2O molecule ($(P)O_2$-$H_1 \cdot\cdot\cdot O_3$ – black trajectory), and vice versa (O_3-$H_1 \cdot\cdot\cdot O_2(P)$ – red trajectory). (B) H^+ transfer dynamics involving monodentate HPO_4^{2-} and a short-range network of three H_2O molecules (O_3-$H_2 \cdot\cdot\cdot O_4$ and O_3-$H_3 \cdot\cdot\cdot O_5$ – red and blue trajectories, respectively). The H^+ transfers in (B) are plotted as the difference in H-bond distances between selected pairs of atoms. The O_2 label in (A) and (B) corresponds to the O_2 atom displayed in Figure 5.1(B). The remaining labels for the solvent O and H atoms are arbitrary. The H_2 and H_3 atoms both initially resided on the O_3 atom.

Figure 5.2(A) portrays a simplified view of the H^+ transfer dynamics involving the monodentate HPO_4^{2-} complex and one H_2O molecule. In fact, however, the H^+ transfer dynamics were more complex and involved a network of seven H_2O molecules. Figure 5.2(B) displays the H^+ transfer dynamics of the monodentate HPO_4^{2-} complex and a short-range network of three H_2O molecules. In Figure 5.2(B), the H^+ transfers are plotted as the difference in H-bond distances between selected pairs of atoms. In other words, H^+ transfers correspond to points where the individual trajectories cross the x-axis at $y = 0$.

Consider first the combination of black ($(P)O_2\text{-}H_1\cdot\cdot\cdot O_3$) and red ($O_3\text{-}H_2\cdot\cdot\cdot O_4$) trajectories. At approximately 100 fs, the black trajectory crossed above $y = 0$, which corresponded to HPO_4^{2-} transferring its H^+ (H_1) to a H_2O molecule (O_3). Note from Figure 5.2(B), however, that the H_3O^+ molecule rapidly transferred a different H^+ (H_2) to another H_2O molecule (O_4). The nearly simultaneous H^+ transfer is shown by the red trajectory crossing above $y = 0$ shortly after the black trajectory crossed $y = 0$. At approximately 500 fs, both the black and red trajectories crossed below $y = 0$, which corresponded to PO_4^{3-} accepting the H^+ (H_1) back from the H_3O^+ molecule (O_3). Figure 5.2(B) also shows that after approximately 1900 fs, the black trajectory crossed above $y = 0$ and only briefly crossed below $y = 0$ at approximately 2200 fs. At approximately 2300 fs, the H_3O^+ molecule (O_3) transferred a different H^+ (H_3) to another H_2O molecule (O_5) (blue trajectory crossed above $y = 0$). Subsequent H^+ transfers only involved H_3O^+ and H_2O molecules. In other words, within the constraints of the QMD simulation, the monodentate HPO_4^{2-} complex converted to a monodentate PO_4^{3-} complex. This suggests that the geometry-optimized starting configuration of monodentate HPO_4^{2-} was an artificially stable complex as revealed by the QMD simulation.

In Figure 5.3, selected features of the monodentate PO_4^{3-} and SO_4^{2-} binding geometries at the (101) α-FeOOH-H_2O interface are displayed. For example, Figure 5.3(A) displays pair correlation functions (PCFs) of the (P)O-Fe and (S)O-Fe bond distances, and Figure 5.3(B) displays PCFs of the P-Fe and S-Fe interatomic distances. The mean (P)O-Fe bond distance, 1.99 Å, was significantly shorter than the mean (S)O-Fe bond distance, 2.10 Å (Figure 5.3(A)). Similarly, the mean P-Fe interatomic distance, 3.25 Å, was significantly shorter than the mean S-Fe interatomic distance, 3.33 Å (Figure 5.3(B)). The average deviations of the (P)O-Fe bond and P-Fe interatomic distances were also slightly smaller than the average deviations of the (S)O-Fe bond and S-Fe interatomic distances. Qualitatively, the PCFs displayed in Figure 5.3(A) and (B) provide evidence that monodentate PO_4^{3-} formed a stronger complex than monodentate SO_4^{2-} at the (101) α-FeOOH-H_2O interface.

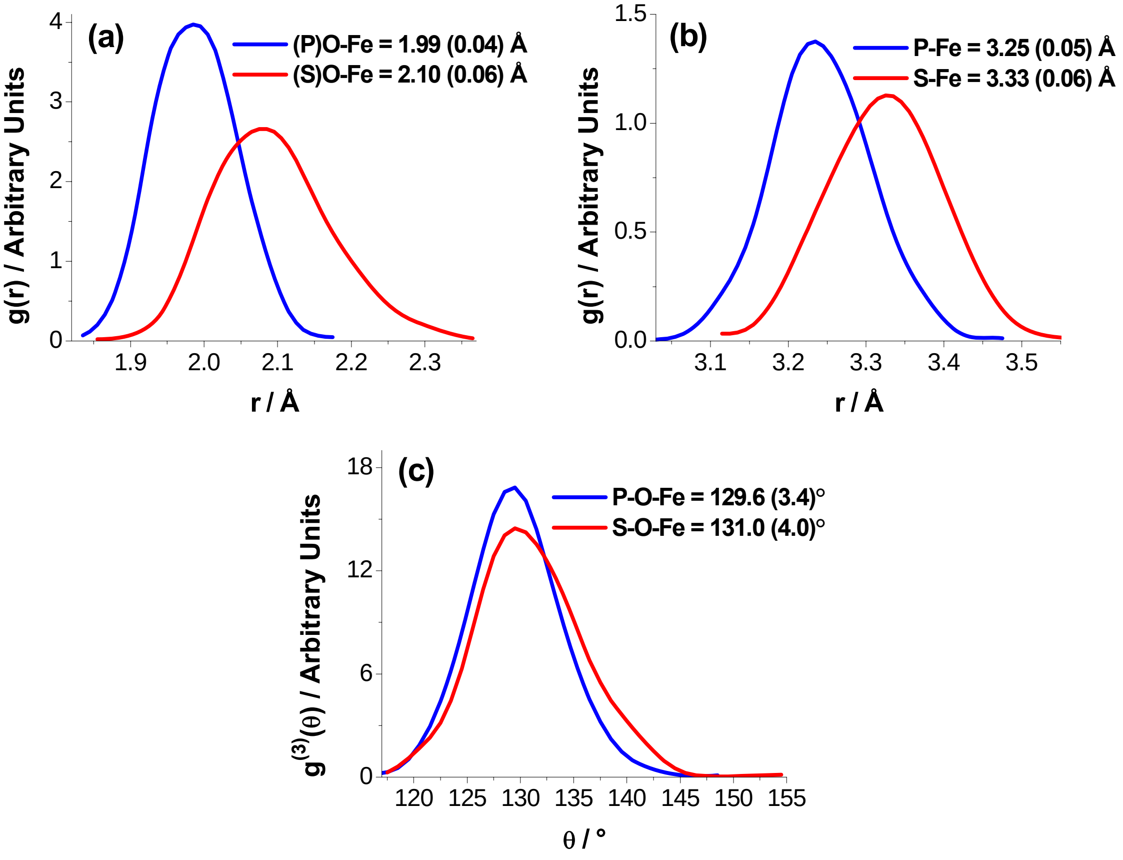

Figure 5.3 Partial pair correlation functions, g(r), of the monodentate PO_4^{3-} and SO_4^{2-} complexes corresponding to the (A) (P)O-Fe and (S)O-Fe bond distances, and the (B) P-Fe and S-Fe interatomic distances. Bond angle distribution functions, $g^{(3)}(\theta)$, correspond to the (C) P-O-Fe and S-O-Fe angles. Means and average deviations (in parentheses) are provided in the g(r) and $g^{(3)}(\theta)$ plots.

In Figure 5.3(C), the monodentate P-O-Fe and S-O-Fe bond angle distributions are displayed. The mean monodentate P-O-Fe bond angle, 129.6°, was similar to the mean monodentate S-O-Fe bond angle, 131.0°, although the former had a slightly smaller average deviation (3.4 versus 4.0°). Interestingly, the mean monodentate P-O-Fe and S-O-Fe bond angles were similar to the mean bidentate bridging P-O-Fe and S-O-Fe bond angles (see Section 5.4.2). Consequently, the mean P-Fe and S-Fe interatomic distances of the monodentate and bidentate bridging complexes were nearly indistinguishable. The unexpectedly small mean P-O-Fe and S-O-Fe bond angles of the monodentate PO_4^{3-} and SO_4^{2-} complexes were principally related to H-bonding interactions with μ_3 OH functional groups (discussed below). As shown in Figure 5.1(B), the monodentate PO_4^{3-} complex H-bonded with two μ_3 OH functional groups (O_2 atom). Likewise, Figure 5.1(D) shows that the monodentate SO_4^{2-} complex H-bonded with one μ_3 OH functional group (O_2 atom).

Figure 5.4(A) displays PCFs of the P-O and P-O(Fe) bonds of monodentate PO_4^{3-}. Likewise, Figure 5.4(B) displays PCFs of the S-O and S-O(Fe) bonds of monodentate SO_4^{2-}. The mean P-O(Fe) and S-O(Fe) bond distances (1.59 and 1.55 Å, respectively) were slightly longer than the mean P-O and S-O bond distances (1.57 and 1.50 Å, respectively), due to bonding with the (101) α-FeOOH surface Fe atoms. Qualitatively, the mean P-O and S-O bond distances were in reasonable agreement with previous studies of aqueous PO_4^{3-} and SO_4^{2-}. For example, Pye and Rudolph [44] performed MP2/6-31+G(d) calculations for $PO_4^{3-}(H_2O)_n$ clusters (n = 0 – 6). The mean P-O bond distance of the $PO_4^{3-}(H_2O)_6$ cluster was approximately 1.59 Å [44]. Recently, Vchirawongkwin *et al.* [45] performed a large-angle X-ray scattering (LAXS) and QMD study of aqueous SO_4^{2-}. The mean S-O bond distance, as derived from the LAXS measurements, was 1.495 Å and in good agreement with the mean S-O bond distance shown in Figure 5.4(B).

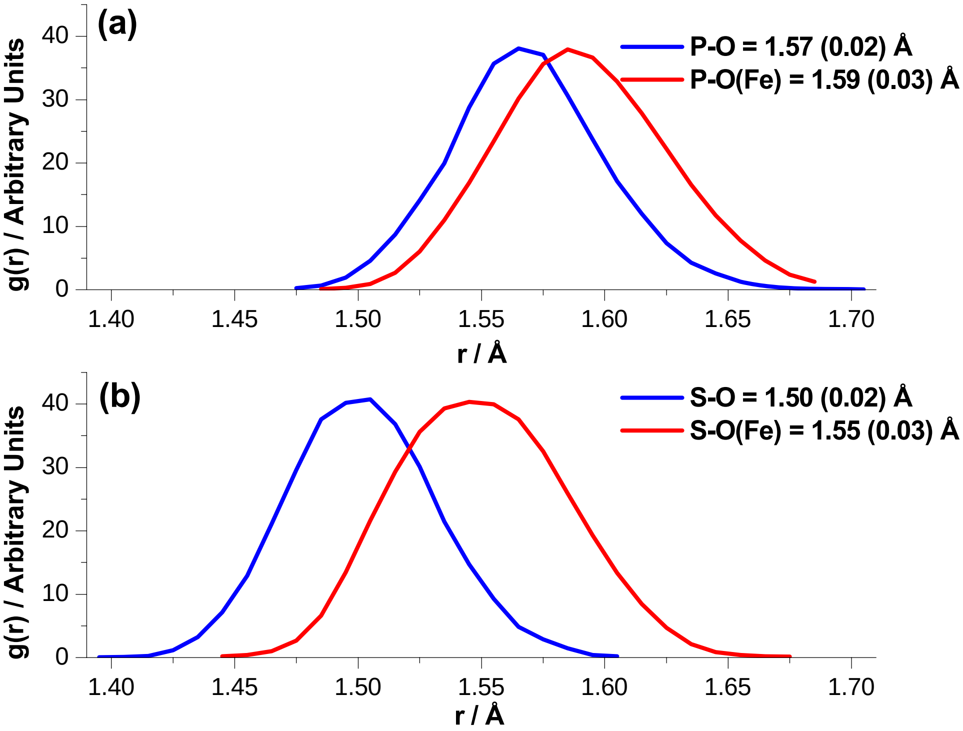

Figure 5.4 Partial pair correlation functions, g(r), of the (A) P-O and P-O(Fe) bond distances of monodentate PO_4^{3-}, and the (B) S-O and S-O(Fe) bond distances of monodentate SO_4^{2-}. Means and average deviations (in parentheses) are provided in the g(r) plots. The y-values of the P-O(Fe) and S-O(Fe) PCFs were multiplied by 3.5 and 3.8, respectively, for visual aid. The x-axes of (A) and (B) are on the same scale to highlight differences between the monodentate PO_4^{3-} and SO_4^{2-} complexes.

The (101) α-FeOOH surface possesses three different types of OH functional groups that can potentially form H-bonds with sulfate and phosphate complexes, thereby affecting their binding geometries. To complicate matters, the H^+

affinities of the OH functional groups vary significantly as a function of pH (e.g. [3]). Numerous *ex situ* and *in situ* IR vibrational spectroscopic studies (see references in Section 5.2) have advanced our understanding of the binding geometries of sulfate and phosphate complexes on α-FeOOH. However, the H-bonding interactions of sulfate and phosphate complexes with the different types of OH functional groups on α-FeOOH surfaces are not well understood. An understanding of these H-bonding interactions may provide valuable insight into the mechanisms of sulfate and phosphate adsorption, ultimately leading to improved predictions of transport and bioavailability in soils.

Figure 5.5(A) displays PCFs of the H-bonds formed by monodentate PO_4^{3-} and the following types of OH functional groups: one singly coordinated OH_2, one singly coordinated OH, and two μ_3 OH. For visual aid, these OH functional groups are labeled in Figure 5.1(B). The corresponding dynamics of the H-bonding interactions are displayed in Figure 5.5(B) – (D). The QMD simulation of monodentate PO_4^{3-} revealed novel molecular-scale insight into its H-bonding interactions at the (101) α-FeOOH-H_2O interface. For example, the relative strengths of the H-bonds (i.e., mean and average deviation of the H-bond distances) depended upon the type of OH functional group. The strongest H-bond formed was between monodentate PO_4^{3-} and the singly coordinated OH_2 functional group, which had a mean distance of 1.66 (0.12) Å (Figure 5.5(B)). The H-bonds formed with the μ_3 OH functional groups were comparatively weaker and had mean distances of 1.82 (0.13) Å

(Figure 5.5(C)) and 2.09 (0.18) Å (dynamics not shown). The weakest H-bond formed was between monodentate PO_4^{3-} and the singly coordinated OH functional group, which had a mean distance of 2.14 (0.20) Å (Figure 5.5(D)).

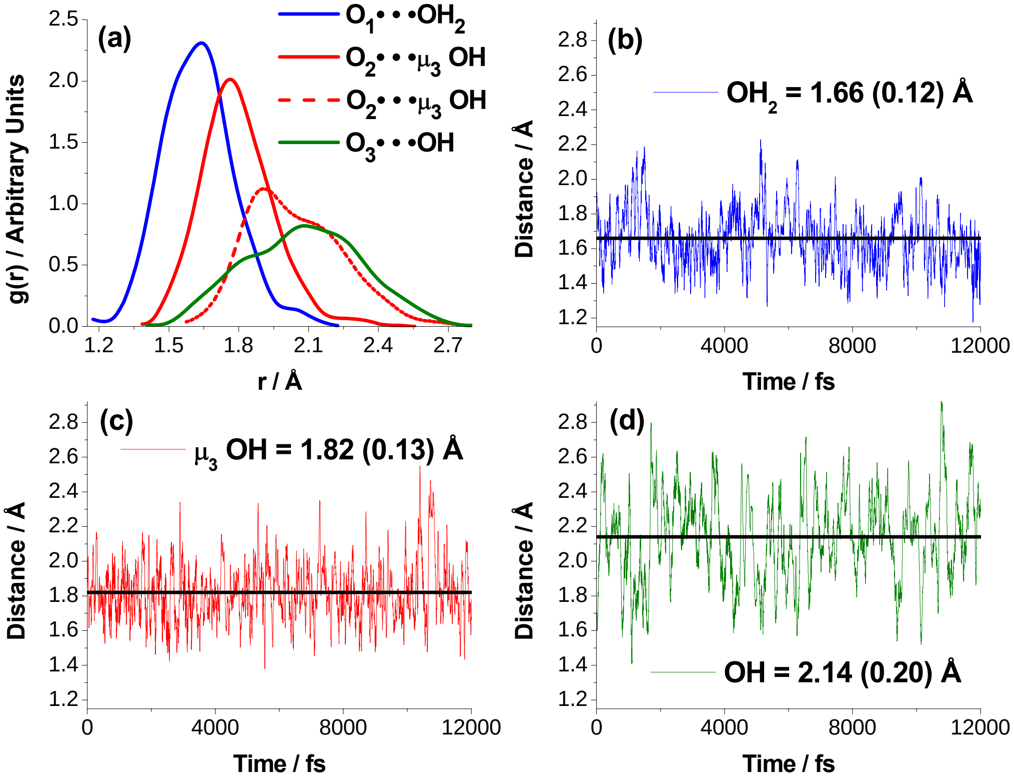

Figure 5.5 H-bonding interactions of monodentate PO_4^{3-} with OH functional groups on the (101) α-FeOOH surface, represented as ball-and-stick and labeled in Figure 5.1(B). (A) Partial pair correlation functions, g(r), of the PO_4^{3-}· · ·HO bonds. Dynamics of the H-bonding interactions of monodentate PO_4^{3-} with the (B) singly coordinated OH_2 functional group, (C) one of the μ_3 OH functional groups (shown by solid red line in (A)), and the (D) singly coordinated OH functional group. The solid black horizontal lines in (B) – (D) represent the means, provided in each panel. The average deviations are provided in parentheses. Time on the x-axis of (B) – (D) corresponds to the 12 ps production phase of the QMD simulation. The y-axes of (B) – (D) are on the same scale.

In the QMD simulation of monodentate HPO_4^{2-} at the (101) α-FeOOH-H_2O interface, the protonated O atom corresponded to the O_2 atom displayed in Figure 5.1(B). The O_2 atom formed H-bonds with two μ_3 OH functional groups. We propose that the H-bonds formed with the μ_3 OH functional groups induced the deprotonation of monodentate HPO_4^{2-}, and subsequent formation of a monodentate PO_4^{3-} complex. Tejedor-Tejedor and Anderson [14] proposed that monodentate PO_4^{3-} complexes could form at the α-FeOOH-H_2O interface. Rahnemaie *et al.* [46] performed a surface complexation modeling study of phosphate adsorption on α-FeOOH and suggested that monodentate PO_4^{3-} complexes would not form to any significant extent. On the contrary, Rahnemaie *et al.* [46] suggested that only deprotonated bidentate bridging and singly protonated monodentate phosphate complexes could form at the α-FeOOH-H_2O interface.

The QMD simulation provided evidence that monodentate HPO_4^{2-} could readily deprotonate to form a stable monodentate PO_4^{3-} complex. The deprotonation of monodentate HPO_4^{2-}, within the constraints of our model, was probably induced by H-bonds formed with μ_3 OH functional groups. It is important to note, however, that the composition of the solvent in our QMD simulations does not realistically simulate experimental conditions, although it was much more realistic than our previous DFT cluster model studies (e.g. [16, 17]). Furthermore, in the study performed by Rahnemaie *et al.* [46], the charge distribution values of the phosphate complexes were derived from static DFT cluster calculations. Unfortunately, the DFT cluster models (edge-sharing dioctahedral Fe^{3+} clusters) did not possess μ_3 OH functional groups. As a result, the H-bonding interactions between the phosphate complexes and OH functional groups on α-FeOOH were not realistically modeled. Such differences in the individual molecular modeling approaches could lead to subtle discrepancies regarding interpretations of the protonation states of phosphate complexes.

Figure 5.6(A) displays PCFs of the H-bonds formed by monodentate SO_4^{2-} and the following types of OH functional groups: one singly coordinated OH_2, one singly coordinated OH, and one μ_3 OH. For visual aid, these OH functional groups are labeled in Figure 5.1(D). The corresponding dynamics of the H-bonding interactions are displayed in Figure 5.6(B) – (D). The dynamical behavior of the monodentate SO_4^{2-} and PO_4^{3-} complexes at the (101) α-FeOOH-H_2O interface were different. The starting configurations of the monodentate HPO_4^{2-} and SO_4^{2-} complexes at the (101) α-FeOOH-H_2O interface were similar, in which the O_2 atom H-bonded with two μ_3 OH functional groups. However, during the initial stages of the equilibration phase, the monodentate SO_4^{2-} complex underwent a hindered rotation. As a result, one of the monodentate SO_4^{2-} O atoms did not interact with an OH functional group, but exclusively with solvent H_2O molecules (O_3 atom in Figure 5.1(D)). In addition, due to the hindered rotation, the monodentate SO_4^{2-} complex only interacted with one μ_3 OH functional group.

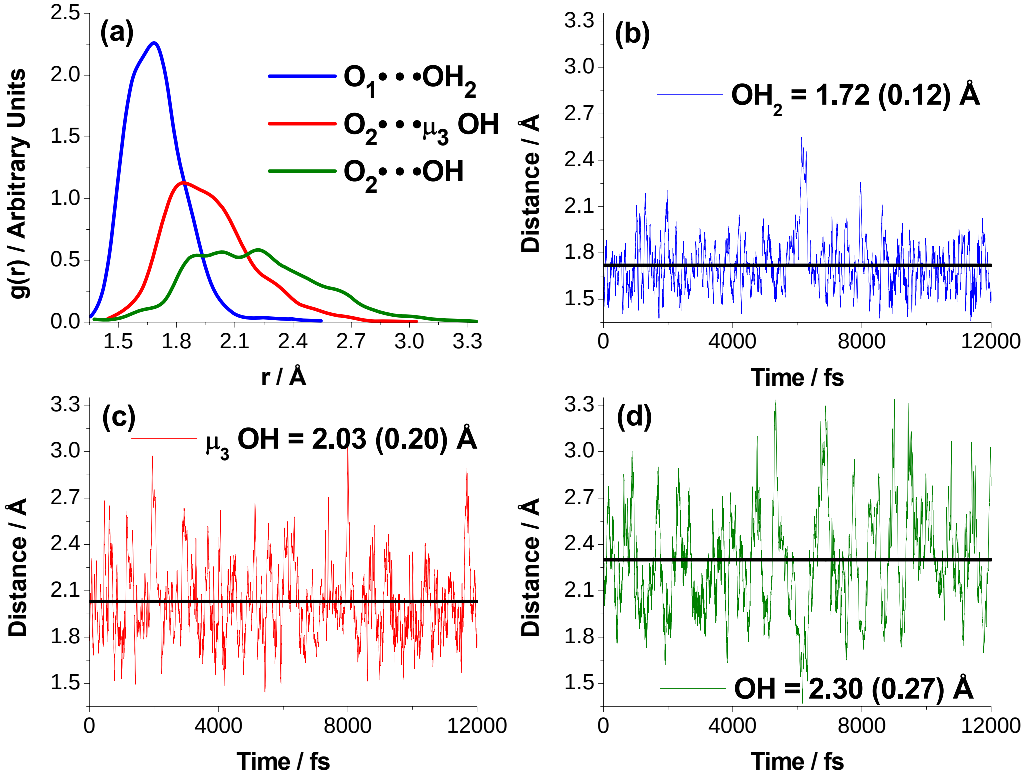

Figure 5.6 H-bonding interactions of monodentate SO_4^{2-} with OH functional groups on the (101) α-FeOOH surface, represented as ball-and-stick and labeled in Figure 5.1(D). (A) Partial pair correlation functions, g(r), of the SO_4^{2-}· · ·HO bonds. Dynamics of the H-bonding interactions of monodentate SO_4^{2-} with the (B) singly coordinated OH_2 functional group, (C) μ_3 OH functional group, and the (D) singly coordinated OH functional group. The solid black horizontal lines in (B) – (D) represent the means, provided in each panel. The average deviations are provided in parentheses. Time on the x-axis of (B) – (D) corresponds to the 12 ps production phase of the QMD simulation. The y-axes of (B) – (D) are on the same scale.

The QMD simulation of monodentate SO_4^{2-} also revealed novel molecular-scale insight into its H-bonding interactions with OH functional groups on the (101) α-FeOOH surface. For example, the strongest H-bond formed was between monodentate SO_4^{2-} and the singly coordinated OH_2 functional group, which had a mean distance of 1.72 (0.12) Å (Figure 5.6(B)). The next strongest H-bond formed was between monodentate SO_4^{2-} and the μ_3 OH functional group, which had a mean distance of 2.03 (0.20) Å (Figure 5.6(C)). Lastly, the weakest H-bond formed was between monodentate SO_4^{2-} and the singly coordinated OH functional group, which had a mean distance of 2.30 (0.27) Å (Figure 5.6(D)). The H-bonding dynamics of monodentate SO_4^{2-} with the μ_3 OH (Figure 5.6(C)) and the singly coordinated OH (Figure 5.6(D)) functional groups show a periodic trend in bond formation and breaking throughout the production phase of the QMD simulation.

The monodentate PO_4^{3-} and SO_4^{2-} O atoms labeled $O_1 – O_3$ in Figure 5.1(B) and (D), respectively, interacted to a varying extent with solvent H_2O molecules. In Figure 5.7(A) – (C), PCFs of the monodentate PO_4^{3-} $O_n\cdot\cdot\cdot O(H_2O)$ atomic pairs, where n = 1, 2, or 3, are displayed as solid red lines. Figure 5.7(A) – (C) also display the integrated PCFs (solid black curves) from which the coordination numbers, N_C, can be estimated for the first hydration shells of the monodentate PO_4^{3-} O_n atoms. The integrated PCFs in Figure 5.7(A) – (C) show that each individual monodentate PO_4^{3-} O_n atom H-bonded with two solvent H_2O molecules (i.e., $N_C = 2$ for the first hydration shell). Therefore, the monodentate PO_4^{3-} O_n atoms interacted equally with solvent H_2O molecules. The interactions of the monodentate SO_4^{2-} O_n atoms with solvent H_2O molecules were, however, markedly different.

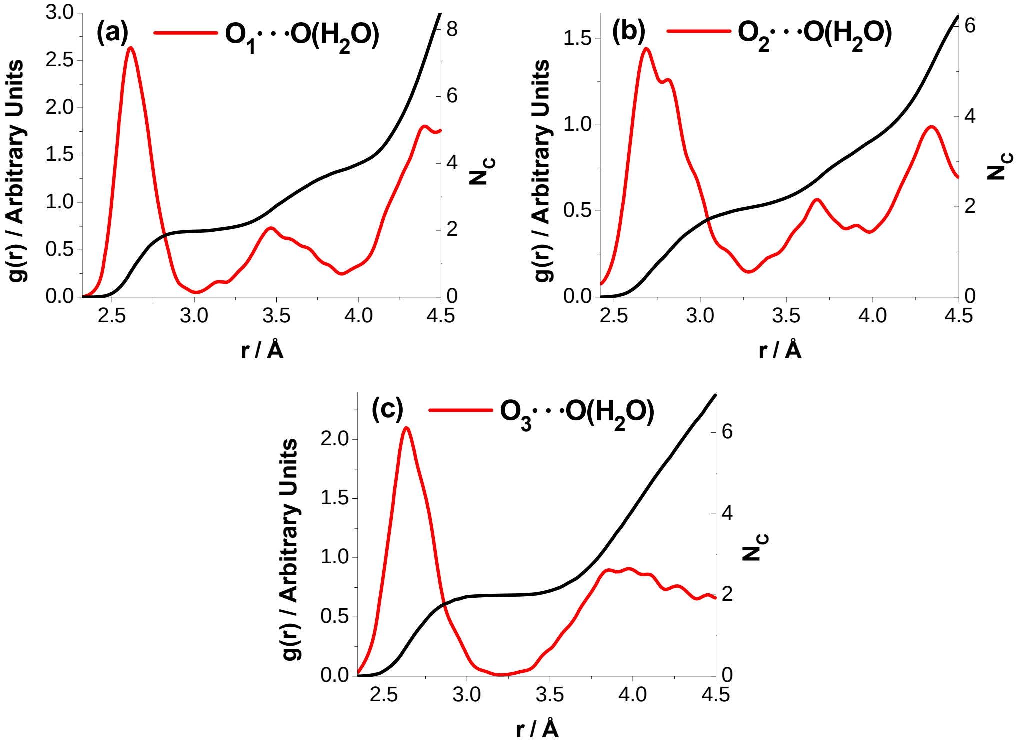

Figure 5.7 (A) – (C) Partial pair correlation functions, g(r), of the monodentate PO_4^{3-} $O_n \cdot \cdot \cdot O(H_2O)$ atomic pairs (n = 1, 2, or 3). The monodentate PO_4^{3-} O_n atoms are labeled O_1, O_2, and O_3 in Figure 5.1(B). The calculation of g(r) included all of the solvent H_2O molecules within a maximum distance of 4.5 Å (i.e., approximately half the length of the shortest simulation cell vector). The black curves represent the integrated PCFs and correspond to the coordination numbers, N_C, of the monodentate PO_4^{3-} $O_n \cdot \cdot \cdot O(H_2O)$ atomic pairs.

In Figure 5.8(A) – (C), PCFs of the monodentate SO_4^{2-} $O_n\cdot\cdot\cdot O(H_2O)$ atomic pairs, where n = 1, 2, or 3, are displayed as solid red lines. The integrated PCFs are also displayed in Figure 5.8(A) – (C) as solid black curves. The monodentate SO_4^{2-} O_1 atom (Figure 5.1(D)) was H-bonded to the singly coordinated OH_2 functional group. Interestingly, as shown by Figure 5.8(A), the O_1 atom did not clearly form a first hydration shell as the distance, r, of the first peak in the $O_1\cdot\cdot\cdot O(H_2O)$ PCF was approximately 3.4 Å. Figure 5.8(B) shows that the monodentate SO_4^{2-} O_2 atom H-bonded with only one solvent H_2O molecule (i.e., $N_C = 1$ for the first hydration shell). The monodentate SO_4^{2-} O_3 atom did not H-bond with an OH functional group on the (101) α-FeOOH surface, but only interacted with solvent H_2O molecules (Figure 5.1(D)). As shown by Figure 5.8(C), the monodentate SO_4^{2-} O_3 atom H-bonded with three solvent H_2O molecules (i.e., $N_C = 3$).

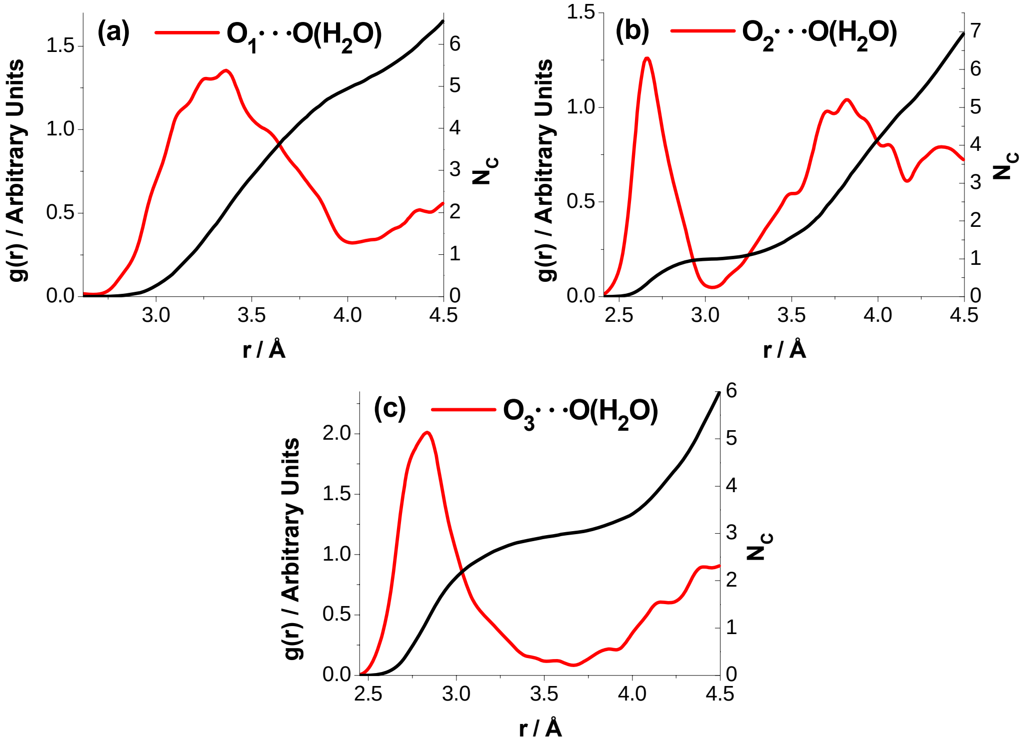

Figure 5.8 (A) – (C) Partial pair correlation functions, g(r), of the monodentate SO_4^{2-} $O_n\cdot\cdot\cdot O(H_2O)$ atomic pairs (n = 1, 2, or 3). The monodentate SO_4^{2-} O_n atoms are labeled O_1, O_2, and O_3 in Figure 5.1(D). The calculation of g(r) included all of the solvent H_2O molecules within a maximum distance of 4.5 Å (i.e., approximately half the length of the shortest simulation cell vector). The black curves represent the integrated PCFs and correspond to the coordination numbers, N_C, of the monodentate SO_4^{2-} $O_n\cdot\cdot\cdot O(H_2O)$ atomic pairs.

As previously mentioned, the shorter (P)O-Fe bond distance, compared to the (S)O-Fe bond distance, provided evidence that monodentate PO_4^{3-} forms a stronger complex at the (101) α-FeOOH-H_2O interface (Figure 5.3(A)). A comparison of Figures 5.5 and 5.6 provides additional qualitative evidence that monodentate PO_4^{3-} forms a stronger complex. First, monodentate PO_4^{3-} formed four H-bonds with OH functional groups: one singly coordinated OH_2, one singly coordinated OH, and two μ_3 OH. In contrast, monodentate SO_4^{2-} only formed three H-bonds with OH functional groups: one singly coordinated OH_2, one singly coordinated OH, and one μ_3 OH. Second, the mean H-bond distances to equivalent OH functional groups were generally shorter for monodentate PO_4^{3-}. A comparison of the mean H-bond distances formed by monodentate PO_4^{3-} and SO_4^{2-}, respectively, reveals the following: 1.66 (0.12) vs. 1.72 (0.12); 1.82 (0.13) vs. 2.03 (0.20); 2.14 (0.20) vs. 2.30 (0.27) Å. Note that monodentate PO_4^{3-} H-bonded with two μ_3 OH functional groups, one of which had a slightly longer mean distance compared to the equivalent monodentate SO_4^{2-} H-bond, specifically 2.09 (0.18) Å.

In general, with respect to sulfate and phosphate adsorption on α-FeOOH, IR vibrational spectroscopic [4-15] and DFT cluster modeling [16, 17] studies have focused on determining whether monodentate and/or bidentate bridging complexes had formed (i.e., number of (S)O-Fe and (P)O-Fe bonds). Consequently, the H-bonding interactions of sulfate and phosphate complexes with OH functional groups on α-FeOOH surfaces are not well understood. In a DFT study, Paul *et al.* [23]

investigated how singly coordinated OH functional groups affected the energy of monodentate SO_4^{2-} adsorption, using edge-sharing dioctahedral Al^{3+} cluster models. Paul *et al.* [23] reported that the adsorption energy was more exergonic when monodentate SO_4^{2-} H-bonded with an OH_2 functional group, in comparison with an OH functional group (e.g. -48 versus -19 kJ mol^{-1}). The QMD results are in qualitative agreement with the finding by Paul *et al.* [23]. Specifically, the strongest H-bonds formed were between monodentate PO_4^{3-} or SO_4^{2-} and a singly coordinated OH_2 functional group (Figures 5.5 and 5.6).

The relative strengths of the H-bonds formed with OH functional groups may provide an important clue regarding sulfate and phosphate ligand exchange mechanisms. It is reasonable to propose, for example, that monodentate sulfate and phosphate complexes are stable intermediates in ligand exchange pathways leading to bidentate bridging complexes. Accordingly, monodentate sulfate or phosphate complexes would undergo ligand exchange with a singly coordinated OH_2 or OH functional group. It is unlikely that the ligand exchange pathways would advance through a μ or μ_3 OH functional group (two or three Fe-O bonds would have to be broken). The QMD simulations provide evidence that a H-bond formed to a singly coordinated OH_2 functional group is significantly stronger than a H-bond formed to a singly coordinated OH functional group (Figures 5.5 and 5.6). Therefore, conversion of a monodentate sulfate or phosphate complex to a bidentate bridging complex would likely proceed through a ligand exchange pathway involving a singly coordinated OH_2 functional group.

5.4.2 Bidentate Bridging Complexes

Snapshots from the QMD simulations of the bidentate bridging HPO_4^{2-} and SO_4^{2-} complexes at the (101) α-FeOOH-H_2O interface are displayed in Figure 5.9. The compositions of the simulation cells, in their entirety, are displayed in Figure 5.9(A) and (C). In Figure 5.9(B) and (D), close-up views of the bidentate bridging HPO_4^{2-} and SO_4^{2-} complexes, respectively, are displayed. Selected atoms that are represented as ball-and-stick and/or labeled in Figure 5.9(B) and (D) will be discussed in detail. Specifically, the H-bonding interactions of bidentate bridging HPO_4^{2-} and SO_4^{2-} with one μ_3 and one μ OH functional group, respectively, will be discussed. In addition, the H-bonding interactions of the bidentate bridging HPO_4^{2-} and SO_4^{2-} atoms labeled O_1 and O_2 with solvent H_2O molecules will be examined.

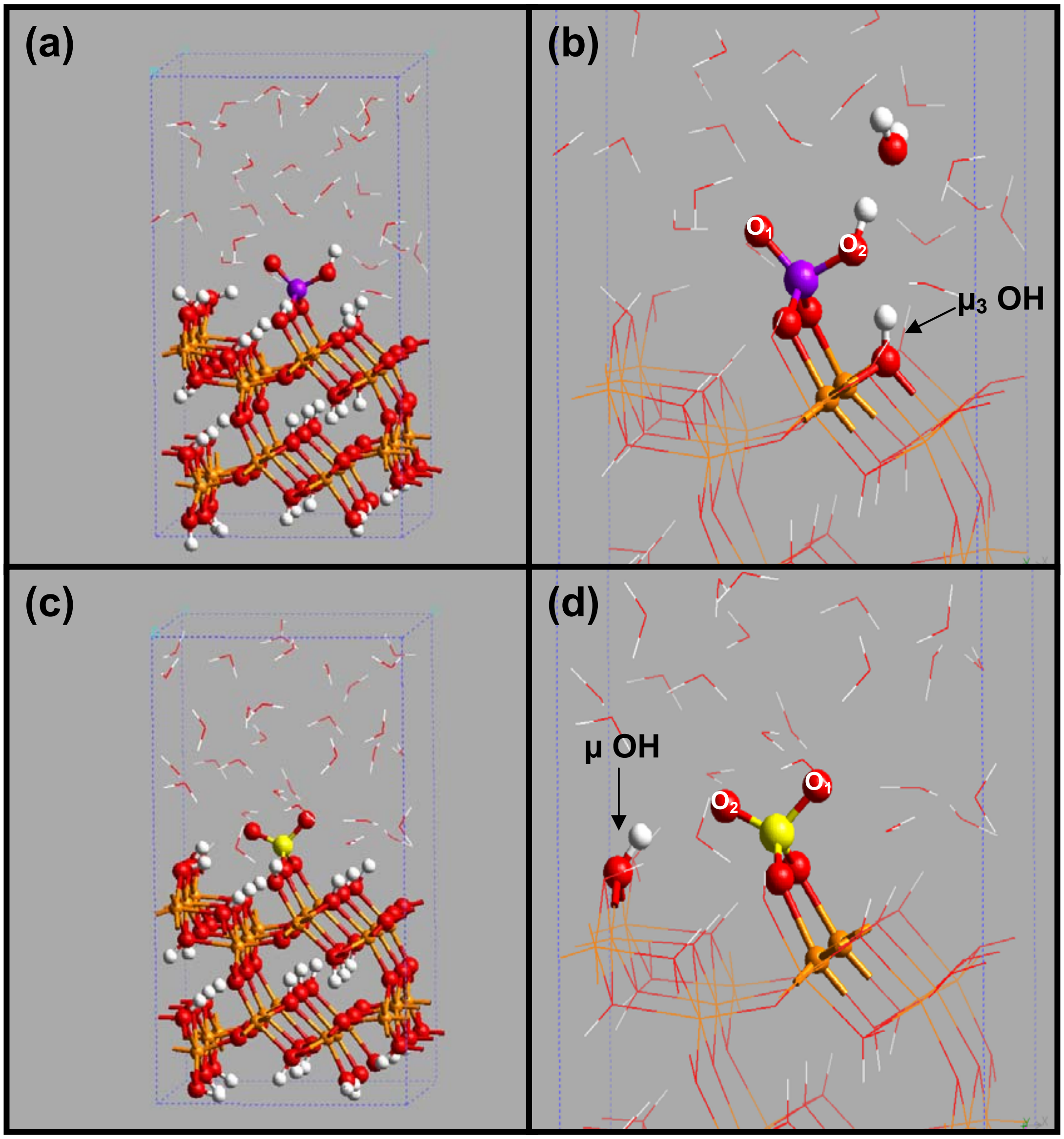

Figure 5.9 Snapshots of the bidentate bridging HPO_4^{2-} and SO_4^{2-} complexes at the (101) α-FeOOH-H_2O interface selected from the production phase of the QMD simulations. (A) and (C) display the compositions of the simulation cells for the bidentate bridging HPO_4^{2-} and SO_4^{2-} systems, respectively. (B) and (D) display close-up views of the bidentate bridging HPO_4^{2-} and SO_4^{2-} complexes, respectively. Selected atoms represented in (B) and (D) as ball-and-stick and/or labeled will be discussed in Section 5.4.2. Red, oxygen; white, hydrogen; purple, phosphorus; yellow, sulfur; and orange, iron.

Figure 5.10 displays the H^+ transfer dynamics of bidentate bridging HPO_4^{2-} and a short-range network of three H_2O molecules. Within 100 fs, the bidentate bridging HPO_4^{2-} complex transferred its H^+ (H_1) to a nearby H_2O molecule (O_3). In Figure 5.10(A) and (B), this particular H^+ transfer corresponded to the black trajectory ($(P)O_2\text{-}H_1 \cdot\cdot\cdot O_3$) crossing y = 0, from negative to positive y-values. Between approximately 100 and 1300 fs, a bidentate bridging PO_4^{3-} complex persisted at the (101) α-FeOOH-H_2O interface. From approximately 1300 to 3500 fs, transient H^+ transfers occurred between the predominantly bidentate bridging PO_4^{3-} complex and the H_3O^+ molecule. These transient H^+ transfers are shown by frequent oscillations of the black trajectory above and below y = 0 (Figure 5.10(A)). After approximately 3500 fs, however, a bidentate bridging HPO_4^{2-} complex persisted throughout the remainder of the QMD simulation (i.e., black trajectory below y = 0). After approximately 3500 fs, Figure 5.10(B) shows that H^+ transfers seldom occurred from the bidentate bridging HPO_4^{2-} complex to a nearby H_2O molecule (e.g. approximately 15000 fs).

The H^+ transfer dynamics of monodentate and bidentate bridging HPO_4^{2-} were quite different. After the initial H^+ transfer had occurred from bidentate bridging HPO_4^{2-} to the nearby H_2O molecule, for example, a subsequent H^+ transfer from the H_3O^+ molecule to another H_2O molecule did not occur. In other words, Figure 5.10(B) shows that the red ($O_3\text{-}H_2 \cdot\cdot\cdot O_4$) and blue ($O_3\text{-}H_3 \cdot\cdot\cdot O_5$) trajectories did not cross y = 0 at any point during the QMD simulation. Consequently, the H^+ transfers occurred exclusively between the bidentate bridging HPO_4^{2-} complex and a single H_2O molecule. In all likelihood, differences in the H^+ transfer dynamics were probably related to the unique H-bonding interactions of monodentate and bidentate bridging HPO_4^{2-} with μ_3 OH functional groups.

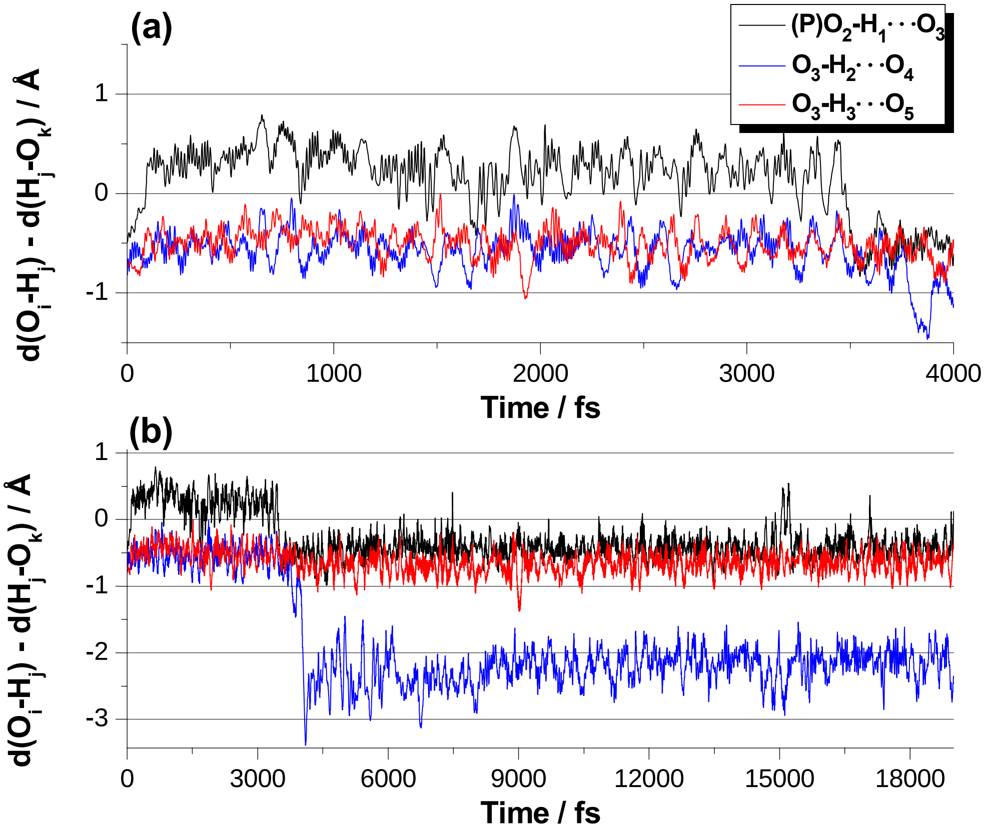

Figure 5.10 H^+ transfer dynamics involving bidentate bridging HPO_4^{2-} and a short-range network of three H_2O molecules (i.e., $(P)O_2\text{-}H_1\cdot\cdot\cdot O_3$, $O_3\text{-}H_2\cdot\cdot\cdot O_4$, and $O_3\text{-}H_3\cdot\cdot\cdot O_5$ – black, red, and blue trajectories, respectively): (A) 0 – 4000 fs and (B) 0 – 19000 fs. The H^+ transfers are plotted as the difference in H-bond distances between selected pairs of atoms. The O_2 label corresponds to the O_2 atom displayed in Figure 5.9(B). The remaining labels for the solvent O and H atoms are arbitrary. The H_2 and H_3 atoms both initially resided on the O_3 atom.

As previously mentioned, the H-bonds formed between monodentate HPO_4^{2-} and two μ_3 OH functional groups probably resulted in the formation of a stable monodentate PO_4^{3-} complex. In contrast, bidentate bridging HPO_4^{2-} could only H-bond with one μ_3 OH functional group (Figure 5.9(B)). Consequently, a bidentate bridging HPO_4^{2-} complex persisted throughout the QMD simulation at the (101) α-FeOOH-H_2O interface. Previous *in situ* IR vibrational spectroscopic studies performed by Tejedor-Tejedor and Anderson [14] and Luengo *et al.* [15] have proposed that bidentate bridging HPO_4^{2-} and PO_4^{3-} complexes could exist at the α-FeOOH-H_2O interface. It is important to note, however, that differences in the local structure of the solvent could have potentially influenced the H^+ transfer dynamics displayed in Figures 5.2 and 5.10.

In Figure 5.11, selected features of the bidentate bridging HPO_4^{2-} and SO_4^{2-} binding geometries at the (101) α-FeOOH-H_2O interface are displayed. Figure 5.11(A) displays PCFs of the (P)O-Fe and (S)O-Fe bond distances. The mean (P)O-Fe bond distance, 2.08 Å, was shorter than the mean (S)O-Fe bond distance, 2.12 Å. Therefore, despite having practically equivalent overall negative charges (i.e., -2), bidentate bridging HPO_4^{2-} formed a slightly stronger complex. As shown below, in comparison to the mean S-O(Fe) bond distance, the bidentate bridging HPO_4^{2-} complex had a longer mean P-O(Fe) bond distance. A longer mean P-O(Fe) bond distance resulted in a longer mean O-O interatomic distance (2.57 versus 2.51 Å for bidentate bridging HPO_4^{2-} and SO_4^{2-}, respectively – data not shown), thereby reducing the relative bond strain of the bidentate bridging HPO_4^{2-} complex. Figure 5.11(B) displays PCFs of the P-Fe and S-Fe interatomic distances. The mean P-Fe interatomic distance, 3.23 Å, was significantly shorter than the mean S-Fe interatomic distance, 3.34 Å. The difference between the mean P-Fe and S-Fe interatomic distances for the monodentate and bidentate bridging complexes, respectively, were similar, namely 0.08 and 0.11 Å (Figures 5.3(B) and 5.11(B)).

In Figure 5.11(C) and (D), the bidentate bridging P-O-Fe and S-O-Fe bond angle distributions, respectively, are displayed. The individual P-O-Fe and S-O-Fe bond angle distributions were slightly different for the bidentate bridging HPO_4^{2-} and SO_4^{2-} complexes. The small differences were due to perturbations in the HPO_4^{2-} and SO_4^{2-} binding geometries, which resulted from H-bonding with μ_3 and μ OH functional groups, respectively (Figure 5.9(B) and (D)). These H-bonding interactions will be discussed shortly. Consequently, the mean P-O-Fe and S-O-Fe bond angles differed by 3.6 – 4.0°. Also note from Figure 5.11 that the larger mean S-O-Fe bond angles (129.2 and 132.8°), in comparison with the mean P-O-Fe bond angles (121.3 and 125.3°), resulted from the comparatively longer mean S-Fe interatomic distance (3.34 versus 3.23 Å).

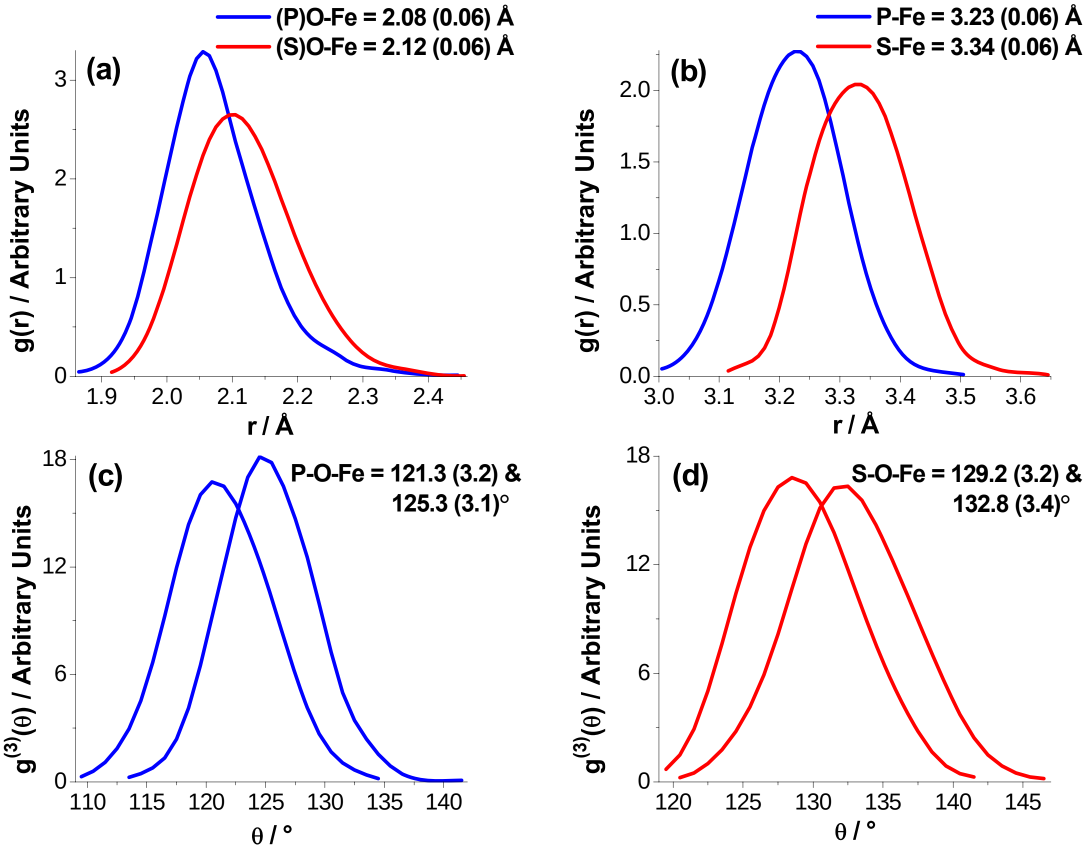

Figure 5.11 Partial pair correlation functions, g(r), of the bidentate bridging HPO_4^{2-} and SO_4^{2-} complexes corresponding to the (A) (P)O-Fe and (S)O-Fe bond distances, and the (B) P-Fe and S-Fe interatomic distances. In (A) and (B), the individual (P)O-Fe, (S)O-Fe, P-Fe, and S-Fe atomic pairs were treated equivalently in the calculation of g(r). Bond angle distribution functions, $g^{(3)}(\theta)$, correspond to the (C) P-O-Fe and (D) S-O-Fe angles. Means and average deviations (in parentheses) are provided in the g(r) and $g^{(3)}(\theta)$ plots.

Extended X-ray absorption fine structure (EXAFS) is a prominent spectroscopic method for studying adsorption at the mineral-H_2O interface. EXAFS can differentiate between monodentate and bidentate bridging complexes, assuming their second shell interatomic distances are sufficiently different (e.g. [47]). Paul *et al.* [48] investigated the binding geometries of monodentate and bidentate bridging SO_4^{2-} complexes at the (100) α-FeOOH-H_2O interface, using periodic DFT. The second shell S-Fe interatomic distances predicted for monodentate and bidentate bridging SO_4^{2-} were significantly different (0.1 – 0.2 Å). Paul *et al.* [48] suggested that EXAFS could therefore distinguish between these binding geometries. As discussed in Section 5.4.1, the mean P-O-Fe and S-O-Fe bond angles of monodentate PO_4^{3-} and SO_4^{2-} were unexpectedly small, due to H-bonding with μ_3 OH functional groups. Consequently, the mean P-Fe and S-Fe interatomic distances of the monodentate and bidentate bridging complexes were very similar (Figures 5.3(B) and 5.11(B)). Therefore, based solely upon the P-Fe and S-Fe interatomic distances, EXAFS probably cannot distinguish between these binding geometries at the (101) α-FeOOH-H_2O interface. It should be noted that, in contrast to the (101) α-FeOOH surface, the monodentate and bidentate bridging SO_4^{2-} complexes did not interact with μ_3 OH functional groups on the (100) α-FeOOH surface [48].

Figure 5.12(A) displays PCFs of the P-O, P-O(Fe), and P-O(H) bond distances for bidentate bridging HPO_4^{2-}. Similar to monodentate PO_4^{3-} and SO_4^{2-}, the mean P-O(Fe) bond distance, 1.58 Å, was longer than the mean P-O bond distance, 1.53 Å, due to bonding with the (101) α-FeOOH surface Fe atoms. As a result of protonation, the mean P-O(H) bond distance, 1.60 Å, was longest. The mean P-O bond distance was in qualitative agreement with an MP2/6-31+G(d) study of $HPO_4^{2-}(H_2O)_n$ (n = 0 – 6), in which the P-O bond distances ranged from approximately 1.54 – 1.57 Å for n = 6 [49]. The difference between the mean P-O and P-O(H) bond distances was also in qualitative agreement with the MP2/6-31+G(d) study [49], although it was smaller in the present study due to sporadic deprotonation and H^+ sharing with a nearby H_2O molecule (Figure 5.10). Figure 5.12(B) displays PCFs of the S-O and S-O(Fe) bonds for bidentate bridging SO_4^{2-}. The difference between the mean S-O and S-O(Fe) bond distances, 0.05 Å, was identical to the difference for monodentate SO_4^{2-} (Figures 5.4(B) and 5.12(B)). Qualitatively, the mean S-O bond distance, 1.49 Å, was in agreement with the LAXS and QMD study of aqueous SO_4^{2-} performed by Vchirawongkwin *et al.* [45].

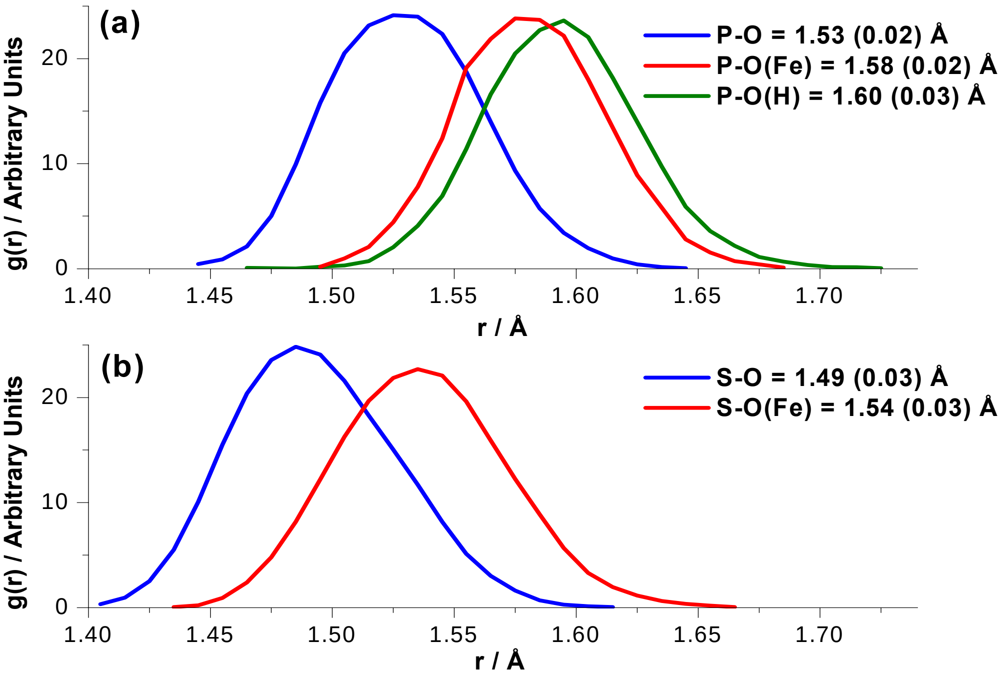

Figure 5.12 Partial pair correlation functions, g(r), of the (A) P-O, P-O(Fe), and P-O(H) bond distances of bidentate bridging HPO_4^{2-}, and the (B) S-O and S-O(Fe) bond distances of bidentate bridging SO_4^{2-}. Means and average deviations (in parentheses) are provided in the g(r) plots. The y-values of the P-O and P-O(H) PCFs were multiplied by 2.0 for visual aid. The x-axes of (A) and (B) are on the same scale to highlight differences between the bidentate bridging HPO_4^{2-} and SO_4^{2-} complexes.

Figure 5.13(A) and (C) display PCFs of the H-bonds formed by bidentate bridging HPO_4^{2-} and SO_4^{2-}, respectively. For visual aid, these OH functional groups are labeled in Figure 5.9(B) and (D). The corresponding dynamics of the H-bonding interactions are displayed in Figure 5.13(B) and (D). Due to the rotational inflexibility of bidentate bridging HPO_4^{2-} and SO_4^{2-}, in contrast to monodentate PO_4^{3-} and SO_4^{2-}, only one H-bond was formed to an OH functional group on the (101) α-FeOOH surface. The bidentate bridging HPO_4^{2-} complex H-bonded with a μ_3 OH functional group, which had a mean distance of 1.87 (0.12) Å (Figure 5.13(B)). This particular μ_3 OH functional group also H-bonded with monodentate PO_4^{3-}, which had a mean distance of 1.82 (0.13) Å (Figure 5.5(C)). Hence, the strengths of these H-bonds were similar. Interestingly, the bidentate bridging SO_4^{2-} complex H-bonded with a μ OH functional group, which had a mean distance of 1.92 (0.12) Å (Figure 5.13(D)). The starting configurations of bidentate bridging HPO_4^{2-} and SO_4^{2-} were similar, in which both complexes H-bonded with the μ_3 OH functional group displayed in Figure 5.9(B). Despite their similar starting configurations, however, the bidentate bridging SO_4^{2-} complex assumed a more upright binding geometry and H-bonded with a μ OH functional group.

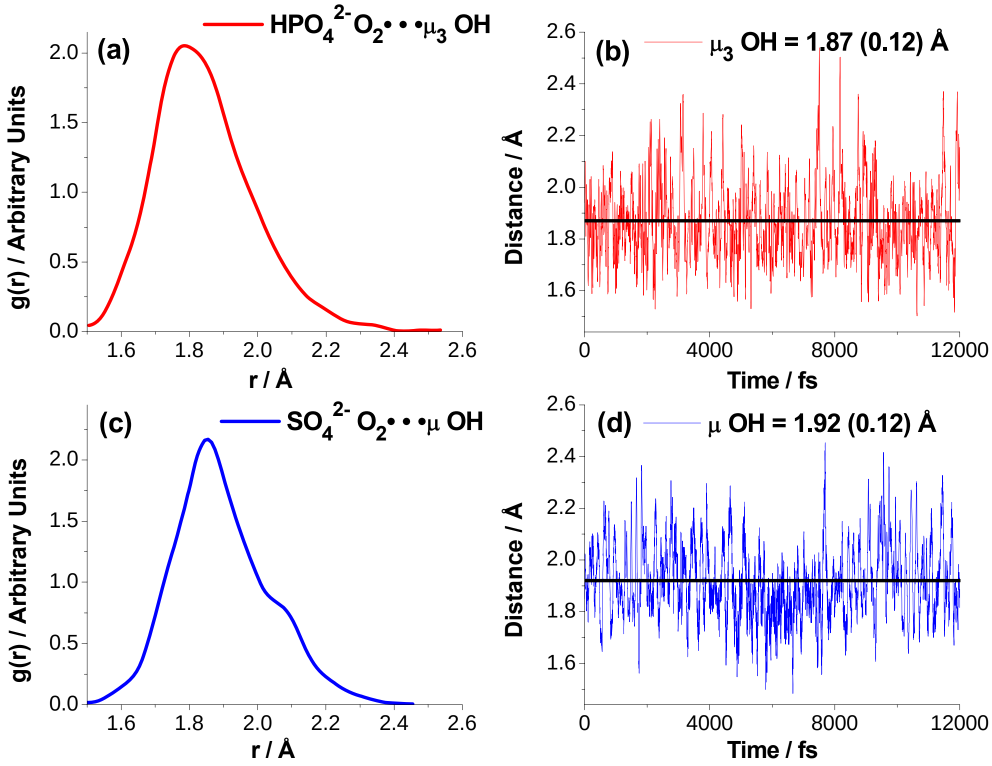

Figure 5.13 H-bonding interactions of bidentate bridging HPO_4^{2-} and SO_4^{2-} with OH functional groups on the (101) α-FeOOH surface, represented as ball-and-stick and labeled in Figure 5.9(B) and (D), respectively. (A) Partial pair correlation function, g(r), of the bidentate bridging $HPO_4^{2-}\cdot\cdot\cdot HO$ bond. (B) Dynamics of the H-bonding interaction of HPO_4^{2-} with a μ_3 OH functional group. (C) Partial pair correlation function, g(r), of the bidentate bridging $SO_4^{2-}\cdot\cdot\cdot HO$ bond. (D) Dynamics of the H-bonding interaction of SO_4^{2-} with a μ OH functional group. The solid black horizontal lines in (B) and (D) represent the means, provided in each panel. The average deviations are provided in parentheses. Time on the x-axis of (B) and (D) corresponds to the 12 ps production phase of the QMD simulation. The y-axes of (B) and (D) are on the same scale.

The bidentate bridging HPO_4^{2-} and SO_4^{2-} O atoms labeled O_1 and O_2 in Figure 5.9(B) and (D), respectively, interacted to a varying extent with solvent H_2O molecules. In Figure 5.14(A) and (B), PCFs of the bidentate bridging HPO_4^{2-} $O_n\cdot\cdot\cdot O(H_2O)$ atomic pairs, where n = 1 or 2, are displayed as solid red lines. The integrated PCFs are displayed as solid black curves. The integrated PCF in Figure 5.14(A) shows that the O_1 atom H-bonded with two solvent H_2O molecules (i.e., $N_C = 2$). On the other hand, Figure 5.14(B) shows that the O_2 atom only H-bonded with one solvent H_2O molecule (i.e., $N_C = 1$). The smaller N_C for the first hydration shell of O_2 was presumably due to its interaction with the μ_3 OH functional group on the (101) α-FeOOH surface. In Figure 5.14(C) and (D), PCFs of the bidentate bridging SO_4^{2-} $O_n\cdot\cdot\cdot O(H_2O)$ atomic pairs, where n = 1 or 2, are displayed. The integrated PCF in Figure 5.14(C) shows that the O_1 atom H-bonded with three solvent H_2O molecules (i.e., $N_C = 3$). This result was identical to the O_3 atom of monodentate SO_4^{2-}, which also did not interact with an OH functional group on the (101) α-FeOOH surface (Figure 5.8(C)). As shown in Figure 5.14(D), the O_2 atom did not clearly form a first hydration shell because the distance, r, of the first peak in the $O_2\cdot\cdot\cdot O(H_2O)$ PCF was approximately 3.4 Å.

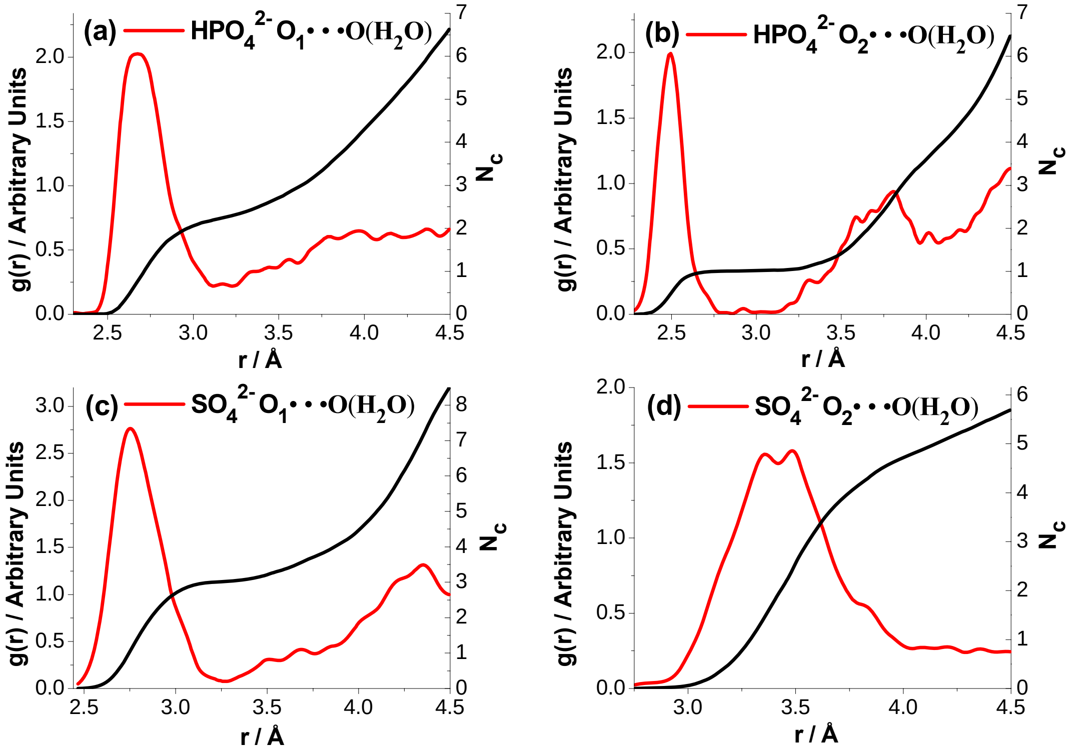

Figure 5.14 (A) – (B) Partial pair correlation functions, g(r), of the bidentate bridging HPO_4^{2-} $O_n\cdot\cdot\cdot O(H_2O)$ atomic pairs (n = 1 or 2). (C) – (D) Partial pair correlation functions, g(r), of the bidentate bridging SO_4^{2-} $O_n\cdot\cdot\cdot O(H_2O)$ atomic pairs (n = 1 or 2). The bidentate bridging HPO_4^{2-} and SO_4^{2-} O_n atoms are labeled O_1 and O_2 in Figure 5.9(B) and (D), respectively. The calculation of g(r) included all of the solvent H_2O molecules within a maximum distance of 4.5 Å (i.e., approximately half the length of the shortest simulation cell vector). The black curves represent the integrated PCFs and correspond to the coordination numbers, N_C, of the bidentate bridging HPO_4^{2-} and SO_4^{2-} $O_n\cdot\cdot\cdot O(H_2O)$ atomic pairs.

5.4.3 Proposed Mechanism for $H_2PO_4^-$ and HPO_4^{2-} Adsorption

In Sections 5.4.1 and 5.4.2, we suggested that monodentate PO_4^{3-} and bidentate bridging HPO_4^{2-} form stronger complexes than monodentate and bidentate bridging SO_4^{2-}, respectively, at the (101) α-FeOOH-H_2O interface. In a macroscopic batch study, Geelhoed *et al.* [50] investigated the competitive adsorption of $H_2PO_4^-$/HPO_4^{2-} and SO_4^{2-} at the α-FeOOH-H_2O interface. Except at pH values less than 4, $H_2PO_4^-$ and HPO_4^{2-} were observed to be stronger competitors than SO_4^{2-} for adsorption sites on α-FeOOH. In addition, Hansmann and Anderson [51] observed that the net free energy of phosphate adsorption on α-FeOOH, as a function of pH and reactant concentration, was significantly greater than the net free energy of sulfate adsorption. To the best of our knowledge, however, a mechanism has not been proposed to explain why $H_2PO_4^-$ and HPO_4^{2-} are stronger competitors than SO_4^{2-} for adsorption sites on α-FeOOH.

In the soil solution pH range of 4 – 9, the predominant sulfate species is SO_4^{2-} and the predominant phosphate species are $H_2PO_4^-$ and HPO_4^{2-}. It is reasonable to assume, therefore, that $H_2PO_4^-$ and HPO_4^{2-} are not stronger competitors than SO_4^{2-} because of different overall negative charges (i.e., Coulombic attraction). In contrast, the fundamental difference between SO_4^{2-} and $H_2PO_4^-$/HPO_4^{2-} adsorption on α-FeOOH is probably related to the protonation states of $H_2PO_4^-$/HPO_4^{2-}. We propose that $H_2PO_4^-$ and HPO_4^{2-} are stronger competitors than SO_4^{2-} for adsorption sites on α-FeOOH because of an intrinsic role that H^+ plays in the mechanisms of $H_2PO_4^-$ and

HPO_4^{2-} adsorption. Several investigators have proposed that deprotonated phosphate complexes form at the α-FeOOH-H_2O interface well below pH 9 [14, 15, 46], which qualitatively suggests an intrinsic role of H^+ in the mechanisms of $H_2PO_4^-$ and HPO_4^{2-} adsorption.

To investigate the potential role of H^+ in the mechanisms of $H_2PO_4^-$ and HPO_4^{2-} adsorption, several bidentate bridging pathways were modeled with DFT cluster calculations. Previous DFT studies have used similar methods to interpret experimental results of oxyanion adsorption on Fe-oxides (e.g. [17, 23, 52, 53]). It is important to note that only one configuration was geometry-optimized for each reactant and product cluster. As a result, the configurational entropy was neglected. The absolute values of the $H_2PO_4^-$ and HPO_4^{2-} adsorption energies should therefore be interpreted cautiously as the magnitude of their error is unknown. The relative differences of the adsorption energies, however, are meaningful and provide insight into the thermodynamic favorability of similar pathways. In Table 5.1, the DFT-calculated energies for each reactant and product cluster are listed. The energies corresponding to the potential $H_2PO_4^-$ and HPO_4^{2-} adsorption pathways are listed in Table 5.2. By way of illustration, Figure 5.15 displays one bidentate bridging $H_2PO_4^-$ adsorption pathway (Pathway 2 listed in Table 5.2).

Table 5.1 DFT-calculated energies for each reactant and product cluster contained in the bidentate bridging $H_2PO_4^-$ and HPO_4^{2-} adsorption pathways listed in Table 5.2. The energies are in Hartrees/molecule. Some of the calculated energies are from [23].

	E_{Gas}^a	$E_{Thermal}^b$	E_{IEFPCM}^c
Reactants			
$H_2PO_4^- \cdot (H_2O)_9$	-1331.738	0.204	-1332.165
$HPO_4^{2-} \cdot (H_2O)_9$	-1331.125	0.194	-1331.695
$Fe_2(OH_6)(OH_2)_4 \cdot (H_2O)_6$	-1466.393	0.272	-1466.840
$[Fe_2(OH_5)(OH_2)_5 \cdot (H_2O)_6]^+$	-1466.788	0.276	-1467.296
Products			
$[Fe_2(OH_4)(OH_2)_4H_2PO_4 \cdot (H_2O)_6]^+$	-1958.112	0.272	-1958.717
$Fe_2(OH_4)(OH_2)_4HPO_4 \cdot (H_2O)_6$	-1957.731	0.269	-1958.277
$[Fe_2(OH_4)(OH_2)_4PO_4 \cdot (H_2O)_6]^-$	-1957.218	0.260	-1957.804
$OH^-(H_2O)_{10}$	-840.413	0.214	-840.751
$(H_2O)_{10}$	-764.493	0.201	-764.762
$(OH^-)_2(H_2O)_9$	-839.767	0.199	-840.269

[a] Gas-phase electronic energy of geometry-optimized reactants and products (B3LYP/6-31+G(d,p)). [b] Thermal correction to the Gibbs free energy derived from the frequency calculations. [c] Total free energy in solution, including all non-electrostatic terms, derived from single-point IEFPCM energy calculations (B3LYP/6-311++G(df,pd)). Note that the CEP-121G basis set was used for the Fe atoms.

Table 5.2 DFT-calculated energies of bidentate bridging $H_2PO_4^-$ and HPO_4^{2-} adsorption pathways on edge-sharing dioctahedral Fe^{3+} cluster models, using the reactant and product energies listed in Table 5.1. The energies are in kJ mol^{-1} (1 Hartree = 2625.5 kJ mol^{-1}).

Pathways

1 – $H_2PO_4^-\cdot(H_2O)_9 + [Fe_2(OH_5)(OH_2)_5\cdot(H_2O)_6]^+ \rightarrow [Fe_2(OH_4)(OH_2)_4H_2PO_4\cdot(H_2O)_6]^+ + OH^-(H_2O)_{10}$
ΔG = -5.7
2 – $H_2PO_4^-\cdot(H_2O)_9 + [Fe_2(OH_5)(OH_2)_5\cdot(H_2O)_6]^+ \rightarrow Fe_2(OH_4)(OH_2)_4HPO_4\cdot(H_2O)_6 + 1.1(H_2O)_{10}$
ΔG = -117.0
3 – $HPO_4^{2-}\cdot(H_2O)_9 + [Fe_2(OH_5)(OH_2)_5\cdot(H_2O)_6]^+ \rightarrow Fe_2(OH_4)(OH_2)_4HPO_4\cdot(H_2O)_6 + OH^-(H_2O)_{10}$
ΔG = -61.8
4 – $HPO_4^{2-}\cdot(H_2O)_9 + [Fe_2(OH_5)(OH_2)_5\cdot(H_2O)_6]^+ \rightarrow [Fe_2(OH_4)(OH_2)_4PO_4\cdot(H_2O)_6]^- + 1.1(H_2O)_{10}$
ΔG = -104.2
5 – $H_2PO_4^-\cdot(H_2O)_9 + Fe_2(OH_6)(OH_2)_4\cdot(H_2O)_6 \rightarrow [Fe_2(OH_4)(OH_2)_4H_2PO_4\cdot(H_2O)_6]^+ + (OH^-)_2(H_2O)_9$
ΔG = 34.2
6 – $H_2PO_4^-\cdot(H_2O)_9 + Fe_2(OH_6)(OH_2)_4\cdot(H_2O)_6 \rightarrow Fe_2(OH_4)(OH_2)_4HPO_4\cdot(H_2O)_6 + OH^-(H_2O)_{10}$
ΔG = -44.3
7– $H_2PO_4^-\cdot(H_2O)_9 + Fe_2(OH_6)(OH_2)_4\cdot(H_2O)_6 \rightarrow [Fe_2(OH_4)(OH_2)_4PO_4\cdot(H_2O)_6]^- + 1.1(H_2O)_{10}$
ΔG = -86.7

$$\mathbf{H_2PO_4^{-}\cdot(H_2O)_9 + [\ Fe_2(OH_5)(OH_2)_5\cdot(H_2O)_6\ ]^{+} \longrightarrow Fe_2(OH_4)(OH_2)_4HPO_4\cdot(H_2O)_6 + 1.1(H_2O)_{10}}$$

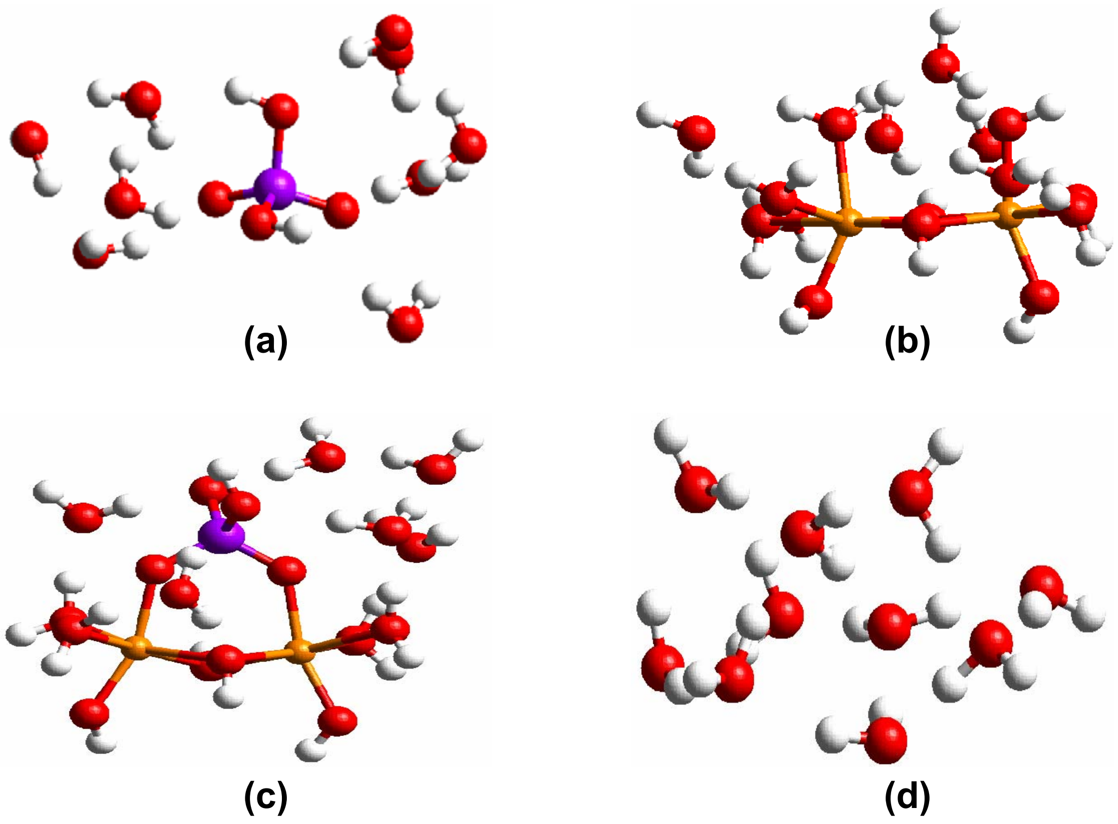

Figure 5.15 Bidentate bridging $H_2PO_4^-$ adsorption pathway corresponding to Pathway 2 listed in Table 5.2. The adsorption pathway is characterized by $H_2PO_4^-$ exchanging with two singly coordinated OH_2 functional groups. (A) $H_2PO_4^-(H_2O)_9$ reactant. (B) $[Fe_2(OH)_5(OH_2)_5\cdot(H_2O)_6]^+$ reactant. (C) $Fe_2(OH)_4(OH_2)_4HPO_4\cdot(H_2O)_6$ product. (D) $(H_2O)_{10}$ product. Red, oxygen; white, hydrogen; purple, phosphorus; and orange, iron.

The bidentate bridging $H_2PO_4^-$ and HPO_4^{2-} adsorption pathways listed in Table 5.2 will now be briefly discussed. In Pathway 1, an $H_2PO_4^-$ adsorption pathway was modeled whereby singly coordinated OH and OH_2 functional groups were exchanged. In Pathway 2, an $H_2PO_4^-$ adsorption pathway was modeled whereby two singly coordinated OH_2 functional groups were exchanged. For Pathways 1 and 2, the products were modeled as bidentate bridging $H_2PO_4^-$ and HPO_4^{2-} complexes, respectively. Consequently, in Pathway 1 it was assumed that an H^+ of $H_2PO_4^-$ did not participate in the adsorption reaction. In Pathway 2, however, it was assumed that one H^+ of $H_2PO_4^-$ was transferred to the singly coordinated OH functional group, prior to exchange with two singly coordinated OH_2 functional groups. The justifications for this particular assumption will be discussed shortly. Pathway 1 was predicted to be only slightly exergonic (-5.7 kJ mol^{-1}). In contrast, due to exchange with two singly coordinated OH_2 functional groups, Pathway 2 was significantly more exergonic (-117.0 kJ mol^{-1}).

In an identical manner, Pathways 3 and 4 modeled bidentate bridging HPO_4^{2-} adsorption. In Pathway 3, it was assumed that an H^+ of HPO_4^{2-} did not participate in the adsorption reaction, whereas it did in Pathway 4. Similar to the preceding discussion, Pathway 3 was significantly less exergonic than Pathway 4 (-61.8 versus -104.2 kJ mol^{-1}). An interesting aspect of $H_2PO_4^-$ and HPO_4^{2-} adsorption is revealed by comparing Pathways 2 and 3. Although the adsorption product was identical for Pathways 2 and 3, namely bidentate bridging HPO_4^{2-}, the adsorption energies were significantly different. Pathway 2 was more thermodynamically favorable, presumably because exchange occurred with two singly coordinated OH_2 functional groups, in contrast to Pathway 3. Another interesting comparison is noted for Pathways 2 and 4. In Pathways 2 and 4, exchange occurred with two singly coordinated OH_2 functional groups and the adsorption products were bidentate bridging HPO_4^{2-} and PO_4^{3-}, respectively. Interestingly, the adsorption energies were quite similar. Tejedor-Tejedor and Anderson [14] and Luengo *et al.* [15] proposed that both bidentate bridging HPO_4^{2-} and PO_4^{3-} complexes form at the α-FeOOH-H_2O interface. The coexistence of bidentate bridging HPO_4^{2-} and PO_4^{3-} may be due, in part, to similar adsorption energies, as estimated by the DFT calculations.

For Pathways 5 – 7, bidentate bridging $H_2PO_4^-$ adsorption was modeled in which the pathways involved a neutral edge-sharing dioctahedral Fe^{3+} cluster. In Pathway 5, $H_2PO_4^-$ adsorption was modeled whereby two singly coordinated OH functional groups were exchanged (i.e., $H_2PO_4^-$ product). In Pathway 6, singly coordinated OH and OH_2 functional groups were exchanged (i.e., HPO_4^{2-} product). In Pathway 7, two singly coordinated OH_2 functional groups were exchanged (i.e., PO_4^{3-} product). The DFT-calculated adsorption energies for Pathways 5 – 7 were: 34.2, -44.3, and -86.7 kJ mol^{-1}, respectively. Pathway 5 was the most endergonic pathway modeled in this study. Pathways 1 and 5 were similar, with respect to an $H_2PO_4^-$ adsorption product, and provide evidence that this complex, regardless of the adsorption pathway, is relatively less thermodynamically favorable.

The thermodynamic favorability of the bidentate bridging $H_2PO_4^-$ and HPO_4^{2-} adsorption pathways (Table 5.2) were significantly affected by ligand exchange with OH versus OH_2 functional groups. In Figure 5.16, we propose a proton-assisted ligand exchange mechanism to illustrate how the H^+ of $H_2PO_4^-$ and

HPO_4^{2-} can participate in adsorption reactions at the α-FeOOH-H_2O interface. The mechanism corresponds to Pathway 7 of Table 5.2. Similar mechanisms could describe the remaining adsorption pathways listed in Table 5.2. It is important to note that the mechanism proposed in Figure 5.16 represents a single adsorption pathway and other pathways should be considered as potentially viable (e.g. coadsorption of H^+ from the solvent).

Step 1 of the proton-assisted ligand exchange mechanism involves an H^+ transfer from $H_2PO_4^-$ to a singly coordinated OH functional group. This H^+ transfer should be thermodynamically favorable for two reasons. First, as $H_2PO_4^-$ is converted to HPO_4^{2-}, the Coulombic attraction between the reactants increases (i.e., $>FeOH_2^+$ + HPO_4^{2-} versus >FeOH + $H_2PO_4^-$). Second, a singly coordinated OH_2 functional group is a significantly better leaving group than a singly coordinated OH functional group. Step 2 involves the formation of an intermediate monodentate HPO_4^{2-} complex. In Step 2, ligand exchange advances through the previously formed singly coordinated OH_2 functional group. Step 3 is another H^+ transfer from the intermediate monodentate HPO_4^{2-} complex to an adjacent singly coordinated OH functional group. Similar to Step 1, the Coulombic attraction at Step 3 increases and an OH_2 functional group is an excellent leaving group. Step 4 involves the formation of a bidentate bridging PO_4^{3-} complex, in which the ligand exchange advances through the singly coordinated OH_2 functional group. As previously mentioned, investigators have proposed that bidentate bridging HPO_4^{2-} complexes could also form at the α-FeOOH-

H_2O interface [14, 15]. The formation of a bidentate bridging HPO_4^{2-} complex can be readily envisioned from Figure 5.16. The pathway would simply begin at Step 2 with an $H_2PO_4^-$ reactant (e.g. Pathway 2 listed in Table 5.2).

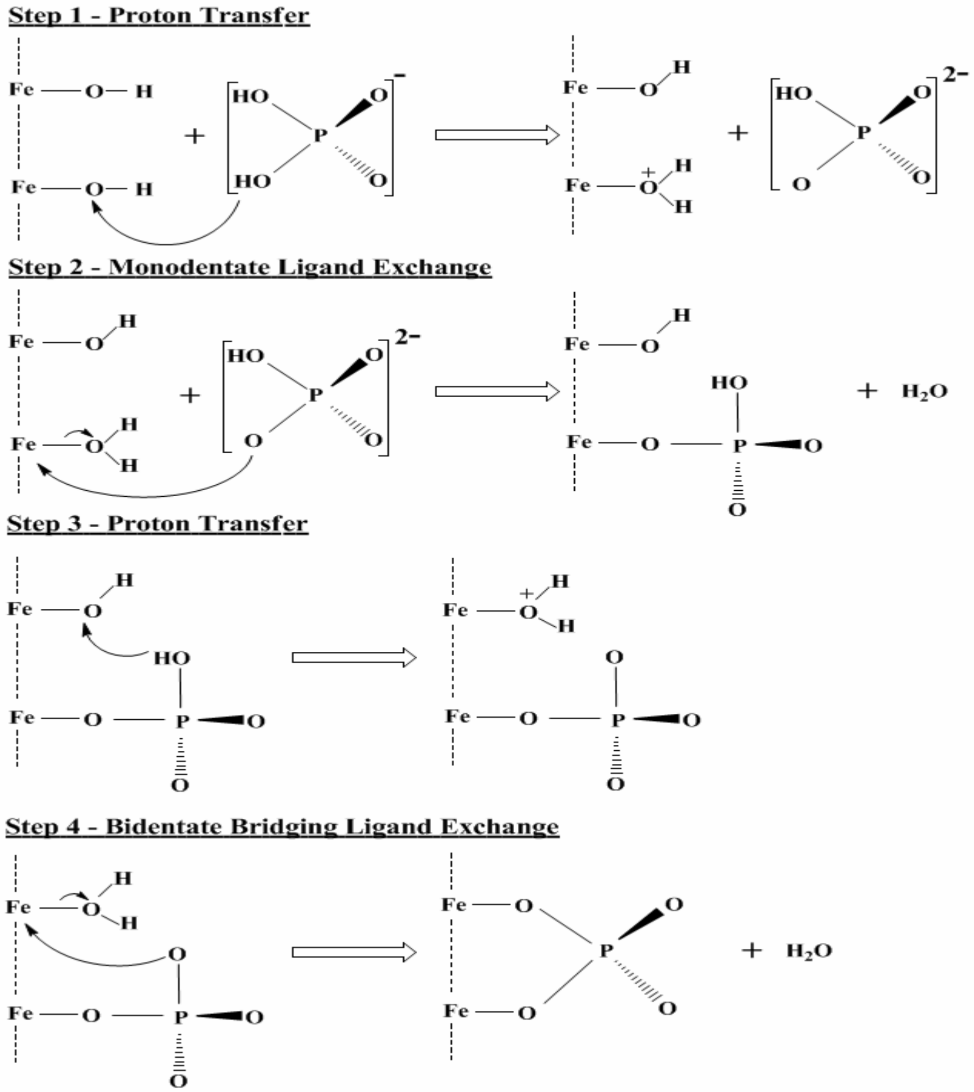

Figure 5.16 A proposed proton-assisted ligand exchange mechanism for $H_2PO_4^-$ adsorption at the α-FeOOH-H_2O interface resulting in a bidentate bridging PO_4^{3-} complex. Note that alternate pathways probably occur concurrently.

We propose that $H_2PO_4^-$ and HPO_4^{2-} are stronger competitors than SO_4^{2-} for adsorption sites on α-FeOOH primarily because of their ability to participate in proton-assisted ligand exchange mechanisms. Between pH 4 and 9, Geelhoed *et al.* [50] did not observe decreased $H_2PO_4^-/HPO_4^{2-}$ adsorption in the presence of SO_4^{2-}. By being able to participate in proton-assisted ligand exchange mechanisms, a significantly greater number of thermodynamically favorable pathways are available for $H_2PO_4^-/HPO_4^{2-}$ adsorption. It is reasonable to assume that SO_4^{2-} can only undergo ligand exchange with singly coordinated OH_2 functional groups. In contrast, $H_2PO_4^-$ and HPO_4^{2-} can undergo ligand exchange with OH functional groups by virtue of H^+ transfer reactions (e.g. Steps 1 and 3 in Figure 5.16). Interestingly, Geelhoed *et al.* [50] did observe decreased $H_2PO_4^-/HPO_4^{2-}$ adsorption in the presence of SO_4^{2-} below pH 4. Below pH 4, the proton-assisted ligand exchange mechanism would become less important due to an increased population of singly coordinated OH_2 functional groups, which can be readily exchanged by SO_4^{2-}.

5.5 Conclusions

In this study, QMD simulations of SO_4^{2-} and HPO_4^{2-} complexes at the (101) α-FeOOH-H_2O interface were performed. The monodentate HPO_4^{2-} complex participated in several H^+ transfers during the initial stages of the equilibration phase. Ultimately, the monodentate HPO_4^{2-} complex converted to a monodentate PO_4^{3-} complex, which remained stable throughout the production phase. Conversely, a bidentate bridging HPO_4^{2-} complex persisted throughout the production phase. The monodentate PO_4^{3-} and SO_4^{2-} complexes formed H-bonds with several OH functional groups on the (101) α-FeOOH surface. The order of H-bonds, from strongest to weakest, was as follows: singly coordinated OH_2, μ_3 OH, and singly coordinated OH functional groups. The bidentate bridging HPO_4^{2-} and SO_4^{2-} complexes, though to a significantly lesser extent, also formed H-bonds with OH functional groups on the (101) α-FeOOH surface. The bidentate bridging HPO_4^{2-} complex formed one H-bond with a μ_3 OH functional group, while the bidentate bridging SO_4^{2-} complex formed one H-bond with a μ OH functional group.

To investigate the potential role of H^+ in the mechanisms of $H_2PO_4^-$ and HPO_4^{2-} adsorption, several bidentate bridging pathways were modeled with DFT cluster calculations. The thermodynamic favorability of the bidentate bridging $H_2PO_4^-$ and HPO_4^{2-} adsorption pathways were significantly affected by ligand exchange with OH versus OH_2 functional groups. A proton-assisted ligand exchange mechanism was proposed to explain why $H_2PO_4^-$ and HPO_4^{2-} are stronger competitors than SO_4^{2-} for adsorption sites on α-FeOOH, particularly above pH 4.0.

5.6 References

1. Schwertmann, U.; Taylor, R. M., Iron Oxides. In *J.B. Dixon and S.B. Weed (ed.) Minerals in Soil Environments*, 2nd ed.; Book Series No. 1, SSSA: Madison, WI, 1989; pp 379–438.

2. Cornell, R. M.; Schwertmann, U., *The Iron Oxides: Structure, Properties, Reactions, Occurrences and Uses*. Wiley-VCH: 2003.

3. Gaboriaud, F.; Ehrhardt, J. J., Effects of Different Crystal Faces on the Surface Charge of Colloidal Goethite (α-FeOOH) Particles: An Experimental and Modeling Study. *Geochimica et Cosmochimica Acta* **2003,** *67*, 967-983.

4. Parfitt, R. L.; Smart, R. S. C., Infrared Spectra from Binuclear Bridging Complexes of Sulfate Adsorbed on Goethite (α-FeOOH). *Journal of the Chemical Society-Faraday Transactions I* **1977,** *73*, 796-802.

5. Parfitt, R. L.; Smart, R. S. C., The Mechanism of Sulfate Adsorption on Iron Oxides. *Soil Science Society of America Journal* **1978,** *42*, (1), 48-50.

6. Turner, L. J.; Kramer, J. R., Sulfate Ion Binding on Goethite and Hematite. *Soil Science* **1991,** *152*, (3), 226-230.

7. Parfitt, R. L.; Atkinson, R. J., Phosphate Adsorption on Goethite (α-FeOOH). *Nature* **1976,** *264*, (5588), 740-742.

8. Parfitt, R. L.; Atkinson, R. J.; Smart, R. S. C., The Mechanism of Phosphate Fixation by Iron Oxides. *Soil Science Society of America Proceedings* **1975,** *39*, (5).

9. Parfitt, R. L.; Atkinson, R. J.; Smart, R. S. C., Mechanism of Phosphate Fixation by Iron Oxides. *Soil Science Society of America Journal* **1975,** *39*, (5), 837-841.

10. Parfitt, R. L.; Russell, J. D.; Farmer, V. C., Confirmation of Surface Structures of Goethite (α-FeOOH) and Phosphated Goethite by Infrared Spectroscopy. *Journal of the Chemical Society-Faraday Transactions I* **1976,** *72*, 1082-1087.

11. Persson, P.; Nilsson, N.; Sjoberg, S., Structure and Bonding of Orthophosphate Ions at the Iron Oxide-Aqueous Interface. *Journal of Colloid and Interface Science* **1996,** *177*, 263-275.

12. Peak, D.; Ford, R. G.; Sparks, D. L., An In Situ ATR-FTIR Investigation of Sulfate Bonding Mechanisms on Goethite. *Journal of Colloid and Interface Science* **1999,** *218*, (1), 289-299.

13. Wijnja, H.; Schulthess, C. P., Vibrational Spectroscopy Study of Selenate and Sulfate Adsorption Mechanisms on Fe and Al (hydr)oxide Surfaces. *Journal of Colloid and Interface Science* **2000,** *229*, (1), 286-297.

14. Tejedor-Tejedor, M. I.; Anderson, M. A., Protonation of Phosphate on the Surface of Goethite as Studied by CIR-FTIR and Electrophoretic Mobility. *Langmuir* **1990,** *6*, (3), 602-611.

15. Luengo, C.; Brigante, M.; Antelo, J.; Avena, M., Kinetics of Phosphate Adsorption on Goethite: Comparing Batch Adsorption and ATR-IR Measurements. *Journal of Colloid and Interface Science* **2006,** *300*, (2), 511-518.

16. Paul, K. W.; Borda, M. J.; Kubicki, J. D.; Sparks, D. L., Effect of Dehydration on Sulfate Coordination and Speciation at the Fe-(hydr)oxide-Water Interface: A Molecular Orbital/Density Functional Theory and Fourier Transform Infrared Spectroscopic Investigation. *Langmuir* **2005,** *21*, (24), 11071-11078.

17. Kwon, K. D.; Kubicki, J. D., Molecular Orbital Theory Study on Surface Complex Structures of Phosphates to Iron Hydroxides: Calculation of Vibrational Frequencies and Adsorption Energies. *Langmuir* **2004,** *20*, (21), 9249-9254.

18. Tunega, D.; Gerzabek, M. H.; Haberhauer, G.; Lischka, H., Formation of 2,4-D complexes on Montmorillonites - An *Ab Initio* Molecular Dynamics Study. *European Journal of Soil Science* **2007,** *58*, (3), 680-691.

19. Kerisit, S.; Ilton, E. S.; Parker, S. C., Molecular Dynamics Simulations of Electrolyte Solutions at the (100) Goethite Surface. *J. Phys. Chem. B* **2006,** *110*, (41), 20491-20501.

20. Aquino, A. J. A.; Tunega, D.; Haberhauer, G.; Gerzabek, M. H.; Lischka, H., Quantum Chemical Adsorption Studies on the (110) Surface of the Mineral Goethite. *J. Phys. Chem. C* **2007,** *111*, (2), 877-885.

21. Szytula, A.; Burewicz, A.; Dimitrij.Z; Krasnick.S; Rzany, H.; Todorovi.J; Wanic, A.; Wolski, W., Neutron Diffraction Studies of Alpha-FeOOH. *Physica Status Solidi* **1968,** *26*, (2), 429-434.

22. Hahn, T., ed, *International Tables of Crystallography*. Kluwer Academic Publishers: Norwell, MA, 1996.

23. Paul, K. W.; Kubicki, J. D.; Sparks, D. L., Quantum Chemical Calculations of Sulfate Adsorption at the Al- and Fe-(Hydr)oxide-H_2O Interface-Estimation of Gibbs Free Energies. *Environmental Science and Technology* **2006,** *40*, (24), 7717-7724.

24. Kresse, G.; Furthmuller, J., Efficient Iterative Schemes for *Ab Initio* Total-Energy Calculations Using a Plane-Wave Basis Set. *Physical Review B* **1996,** *54*, (16), 11169-11186.

25. Kresse, G.; Furthmuller, J., Efficiency of Ab-Initio Total Energy Calculations for Metals and Semiconductors Using a Plane-Wave Basis Set. *Computational Materials Science* **1996,** *6*, (1), 15-50.

26. Kohn, W.; Sham, L. J., Self-Consistent Equations Including Exchange and Correlation Effects. *Physical Review* **1965,** *140*, A1133-A1138.

27. Perdew, J. P.; Burke, K.; Ernzerhof, M., Generalized Gradient Approximation Made Simple. *Physical Review Letters* **1996,** *77*, (18), 3865-3868.

28. Pulay, P., Convergence Acceleration of Iterative Sequences. The Case of SCF Iteration. *Chemical Physics Letters* **1980,** *73*, (2), 393-398.

29. Wood, D. M.; Zunger, A., A New Method for Diagonalising Large Matrices. *Journal of Physics A: Mathematical and General* **1985,** *18*, (9), 1343-1359.

30. Blochl, P. E., Projector Augmented-Wave Method. *Physical Review B* **1994,** *50*, (24), 17953-17979.

31. Kresse, G.; Joubert, D., From Ultrasoft Pseudopotentials to the Projector Augmented-Wave Method. *Physical Review B* **1999,** *59*, (3), 1758-1775.

32. Monkhorst, H. J.; Pack, J. D., Special Points for Brillouin-Zone Integrations. *Physical Review B* **1976,** *13*, (12), 5188-5192.

33. Methfessel, M.; Paxton, A. T., High-Precision Sampling for Brillouin-Zone Integration in Metals. *Physical Review B* **1989,** *40*, (6), 3616-3621.

34. Rollmann, G.; Rohrbach, A.; Entel, P.; Hafner, J., First-Principles Calculation of the Structure and Magnetic Phases of Hematite. *Physical Review B* **2004,** *69*, (16), 165107.

35. Rohrbach, A.; Hafner, J.; Kresse, G., Electronic Correlation Effects in Transition-Metal Sulfides. *Journal of Physics: Condensed Matter* **2003,** *15*, (6), 979.

36. Dudarev, S. L.; Botton, G. A.; Savrasov, S. Y.; Humphreys, C. J.; Sutton, A. P., Electron-Energy-Loss Spectra and the Structural Stability of Nickel Oxide: An LSDA+U Study. *Physical Review B* **1998,** *57*, (3), 1505-1509.

37. Nosé, S., A Unified Formulation of the Constant Temperature Molecular Dynamics Methods. *The Journal of Chemical Physics* **1984,** *81*, (1), 511-519.

38. Frisch, M. J., Trucks, G. W., Schlegel, H. B., Scuseria, G. E., Robb, M. A., Cheeseman, J. R., Montgomery, Jr., J. A., Vreven, T., Kudin, K. N., Burant, J. C., Millam, J. M., Iyengar, S. S., Tomasi, J., Barone, V., Mennucci, B., Cossi, M., Scalmani, G., Rega, N., Petersson, G. A., Nakatsuji, H., Hada, M., Ehara, M., Toyota, K., Fukuda, R., Hasegawa, J., Ishida, M., Nakajima, T., Honda, Y., Kitao, O., Nakai, H., Klene, M., Li, X., Knox, J. E., Hratchian, H. P., Cross, J. B., Bakken, V., Adamo, C., Jaramillo, J., Gomperts, R., Stratmann, R. E., Yazyev, O., Austin, A. J., Cammi, R., Pomelli, C., Ochterski, J. W., Ayala, P. Y., Morokuma, K., Voth, G. A., Salvador, P., Dannenberg, J. J., Zakrzewski, V. G., Dapprich, S., Daniels, A. D., Strain, M. C., Farkas, O., Malick, D. K., Rabuck, A. D., Raghavachari, K., Foresman, J. B., Ortiz, J. V., Cui, Q., Baboul, A. G., Clifford, S., Cioslowski, J., Stefanov, B. B., Liu, G., Liashenko, A., Piskorz, P., Komaromi, I., Martin, R. L., Fox, D. J., Keith, T., Al-Laham, M. A., Peng, C. Y., Nanayakkara, A., Challacombe, M., Gill, P. M. W., Johnson, B., Chen, W., Wong, M. W., Gonzalez, C., and Pople, J. A. *Gaussian 03, revision B.05; Gaussian, Inc.;*, Wallingford CT, 2004.

39. Becke, A. D., Density-Functional Thermochemistry 3. The Role of Exact Exchange. *Journal of Chemical Physics* **1993,** *98*, (7), 5648-5652.

40. Lee, C. T.; Yang, W. T.; Parr, R. G., Development of the Colle-Salvetti Correlation-Energy Formula into a Functional of the Electron-Density. *Physical Review B* **1988,** *37*, (2), 785-789.

41. Stevens, W. J.; Krauss, M.; Basch, H.; Jasien, P. G., Relativistic Compact Effective Potentials and Efficient, Shared-Exponent Basis-Sets for the 3rd-Row, 4th-Row, and 5th-Row Atoms. *Canadian Journal of Chemistry-Revue Canadienne De Chimie* **1992,** *70*, (2), 612-630.

42. Cances, E.; Mennucci, B.; Tomasi, J., A New Integral Equation Formalism for the Polarizable Continuum Model: Theoretical Background and Applications to Isotropic and Anisotropic Dielectrics. *Journal of Chemical Physics* **1997,** *107*, (8), 3032-3041.

43. Origin7.5 OriginLab Corp., Northampton, MA., 2003.

44. Pye, C. C.; Rudolph, W. W., An *Ab Initio*, Infrared, and Raman Investigation of Phosphate Ion Hydration. *J. Phys. Chem. A* **2003,** *107*, (41), 8746-8755.

45. Vchirawongkwin, V.; Rode, B. M.; Persson, I., Structure and Dynamics of Sulfate Ion in Aqueous Solution - An *Ab Initio* QMCF MD Simulation and Large Angle X-ray Scattering Study. *J. Phys. Chem. B* **2007,** *111*, (16), 4150-4155.

46. Rahnemaie, R.; Hiemstra, T.; vanRiemsdijk, W. H., Geometry, Charge Distribution, and Surface Speciation of Phosphate on Goethite. *Langmuir* **2007,** *23*, (7), 3680-3689.

47. Fendorf, S.; Eick, M. J.; Grossl, P.; Sparks, D. L., Arsenate and chromate retention mechanisms on goethite .1. Surface structure. *Environmental Science & Technology* **1997,** *31*, (2), 315-320.

48. Paul, K. W.; Kubicki, J. D.; Sparks, D. L., Sulphate Adsorption at the Fe (hydr)oxide–H_2O Interface: Comparison of Cluster and Periodic Slab DFT Predictions. *European Journal of Soil Science* **2007** (accepted for publication).

49. Pye, C. C.; Michel, M. R., An *Ab Initio* Investigation of Hydrogen Phosphate Ion Hydration. *Canadian Journal of Analytical Sciences and Spectroscopy* **2004,** *49*, (3), 175-184.

50. Geelhoed, J. S.; Hiemstra, T.; VanRiemsdijk, W. H., Phosphate and Sulfate Adsorption on Goethite: Single Anion and Competitive Adsorption. *Geochimica Et Cosmochimica Acta* **1997,** *61*, (12), 2389-2396.

51. Hansmann, D. D.; Anderson, M. A., Using Electrophoresis in Modeling Sulfate, Selenite, and Phosphate Adsorption onto Goethite. *Environmental Science & Technology* **1985,** *19*, (6), 544-551.

52. Zhang, N. L.; Blowers, P.; Farrell, J., Evaluation of Density Functional Theory Methods for Studying Chemisorption of Arsenite on Ferric Hydroxides. *Environmental Science and Technology* **2005,** *39*, (13), 4816-4822.

53. Kubicki, J. D., Comparison of As(III) and As(V) Complexation onto Al- and Fe-Hydroxides. In *Advances in Arsenic Research*, 2005; Vol. 915, pp 104-117.

Chapter 6

CONSIDERATIONS FOR FUTURE EXPERIMENTAL AND COMPUTATIONAL RESEARCH

6.1 Overview

The transport and bioavailability of nutrients and contaminants in soils are largely controlled by sorption reactions with mineral surfaces (e.g. adsorption, surface precipitation, and polymerization). During the past 20 years, numerous extended X-ray absorption fine structure (EXAFS) spectroscopic studies were performed to determine how nutrients and contaminants react with bulk mineral samples (see relatively recent review by Brown and Sturchio [1]). The EXAFS spectroscopic studies provided novel molecular-scale insight into the adsorption of nutrients and contaminants at the mineral-H_2O interface, occasionally in the presence of counterions (e.g. [2, 3]). During the past 10 – 15 years, attenuated total reflectance Fourier transform infrared (ATR-FTIR) spectroscopic studies provided complementary information regarding the adsorption of inorganic ions (see relatively recent review by Lefevre [4]) and organic acids (e.g. [5]), as a function of pH, ionic strength, and reactant concentration.

At present, the analysis of EXAFS and ATR-FTIR spectroscopic data can be ambiguous and remains a significant challenge to soil chemistry. In the majority of

EXAFS studies, nutrient and contaminant adsorption at the mineral-H_2O interface has been investigated with the use of bulk mineral samples. Minerals commonly possess multiple surface terminations with unique structures and compositions. Unfortunately, the structure and composition of mineral surfaces, particularly how the surfaces relax and reconstruct as a function of hydration, are largely unknown. As a result, the type and density of adsorption sites (e.g. Fe_3O, Fe_2OH, and $FeOH_2$) cannot be precisely determined for different mineral surfaces. Therefore, a fundamental understanding of nutrient and contaminant adsorption remains elusive. In other words, until the structure and composition of mineral surfaces are known, nutrient and contaminant adsorption mechanisms cannot be elucidated solely by EXAFS measurements [6].

The use of qualitative methods to interpret the IR-active vibrational modes of an adsorption complex has restricted the analysis of ATR-FTIR spectroscopic data. To determine the binding geometry of an adsorption complex, previous studies have typically performed point group symmetry analyses of the ATR-FTIR spectra (see [4] and references therein). Hence, ATR-FTIR spectroscopy has been referred to as an "indirect structural" method [7]. Unfortunately, the IR-activity and energies of the vibrational modes of an adsorption complex depend upon its binding geometry, protonation state, and H-bonding to hydroxyl functional groups. Based solely upon experimental evidence, therefore, it is challenging to discern how each of these factors affects the IR-activity and energies of the vibrational modes. In this regard, computational chemistry has become increasingly helpful with respect to quantitative analysis of ATR-FTIR spectroscopic data (e.g. Chapter 2 and references therein).

To improve our understanding of the mechanisms of nutrient and contaminant adsorption at the mineral-H_2O interface, three principal experimental challenges need to be surmounted. First, the structure and composition of hydrated soil mineral surfaces need to be precisely known. The structure and composition of a hydrated soil mineral surface will place an important crystallographic constraint on the mechanisms of nutrient and contaminant adsorption. Second, the binding geometries of nutrient and contaminant complexes on single-crystal mineral surfaces need to be accurately measured using *in situ*, surface-sensitive spectroscopic methods. Third, the nutrient and contaminant adsorption energies on single-crystal mineral surfaces (and bulk mineral samples) need to be accurately measured, using, for example, flow-adsorption calorimetry (Section 6.2.2).

If these experimental challenges can be surmounted, then computational chemistry should be able to successfully interpret the experimental measurements and to rigorously test and support proposed adsorption mechanisms. However, one important assumption may preclude the application of computational chemistry to rigorously test and validate proposed adsorption mechanisms. Specifically, a single reaction pathway should dominate nutrient or contaminant adsorption on single-crystal mineral surfaces, throughout a narrow range of experimental conditions. In other words, the adsorption reaction should be dominated by a single binding geometry.

Fortunately, a growing body of experimental evidence supports this assumption (see references in Section 6.2.1). Regardless, computational chemistry predictions are expected to be central in improving our understanding of the mechanisms of nutrient and contaminant adsorption at the mineral-H_2O interface.

6.2 Experimental Research

6.2.1 GI-EXAFS and CTR Measurements

In recent years, nutrient and contaminant adsorption have been investigated *in situ* on single-crystal mineral surfaces, using grazing-incidence (GI) EXAFS spectroscopy. The principal advantage of GI-EXAFS spectroscopy, in comparison with bulk EXAFS, is that the background X-ray scattering is minimal on single-crystal mineral surfaces. In addition, the X-ray intensity at the surface of a single-crystal can be significantly enhanced by the superposition of incident and reflected X-ray fields. Consequently, the signal-to-noise ratio of a GI-EXAFS spectrum is typically 500 times greater than the signal-to-noise ratio of a bulk EXAFS spectrum [7]. Many noteworthy studies have applied GI-EXAFS spectroscopy to the investigation of nutrient and contaminant adsorption on single-crystal mineral surfaces. For example, Bargar *et al.* investigated Pb^{2+} and Co^{2+} adsorption on single-crystal alumina (α-Al_2O_3) surfaces [8, 9]. Towle *et al.* investigated Co^{2+} adsorption on single-crystal rutile (TiO_2) [10] and α-Al_2O_3 surfaces [11]. Trainor *et al.* investigated Zn^{2+} adsorption on single-crystal α-Al_2O_3 surfaces [12]. The adsorption of uranyl complexes has also been investigated on single-crystal surfaces of TiO_2 [13] and other various soil minerals [14].

Despite the progress achieved by the aforementioned GI-EXAFS spectroscopic studies, two important assumptions significantly affected the data analysis and interpretations. First, the structure and composition of the hydrated, single-crystal mineral surfaces were assumed to be equivalent to their ideal, bulk-terminated (i.e., vacuum-terminated) surfaces. Second, it was assumed that the hydrated, single-crystal mineral surfaces, with and without an adsorbate, had not relaxed or reconstructed [7]. Consequently, the binding geometries of the adsorption complexes were proposed without precise knowledge of the single-crystal mineral surface structures or compositions.

In 2000, Eng *et al.* [15] published a seminal study that reported the structure of the hydrated (0001) surface of α-Al_2O_3. Eng *et al.* [15] used synchrotron-based crystal truncation rod (CTR) diffraction to measure the structure of the hydrated (0001) surface of α-Al_2O_3. In principle, therefore, the aforementioned assumptions regarding the surface termination, relaxation, and reconstruction could be eliminated from GI-EXAFS spectroscopic data analyses [7]. Since the seminal study by Eng *et al.* [15], additional CTR diffraction studies have been published, reporting the structures of several hydrated α-Al_2O_3 and α-Fe_2O_3 single-crystal surfaces (e.g. [16-18]). GI-EXAFS spectroscopic and CTR diffraction measurements are now routinely performed in combination, to determine the binding geometries of nutrient and contaminant complexes on single-crystal surfaces with known structures (e.g. [6, 7]).

Since the structures of several hydrated α-Al_2O_3 and α-Fe_2O_3 single-crystal surfaces are now known, substantial progress in computational chemistry modeling of nutrient and contaminant adsorption is anticipated. Unfortunately, without detailed knowledge of the structures of hydrated mineral surfaces, computational chemistry modeling of nutrient and contaminant adsorption at the mineral-H_2O interface will be hindered. It is important to note, however, that CTR diffraction measurements do not yield information regarding the protonation states of O atoms on single-crystal surfaces. In other words, the exact composition of the single-crystal mineral surfaces remains unknown. Knowledge of both the structure and composition of hydrated mineral surfaces is essential to modeling nutrient and contaminant adsorption, using computational chemistry methods. Furthermore, GI-EXAFS spectroscopic measurements do not provide the energies of nutrient and contaminant adsorption reactions on single-crystal surfaces.

6.2.2 SHG and Flow-Adsorption Calorimetry Measurements

Under typical soil solution conditions, a multitude of aqueous species will compete for identical mineral surface adsorption sites. The equilibrium distribution of nutrient complexes, for example, will depend upon the thermodynamic favorability of the various adsorption pathways. Most importantly, the equilibrium distribution of nutrient or contaminant complexes at the mineral-H_2O interface directly affects their transport and bioavailability in soils. Therefore, it is important to measure the energies of nutrient and contaminant adsorption reactions, using both single-crystal mineral surfaces and bulk mineral samples. Computational chemistry methods can be used to predict the energies of nutrient and contaminant adsorption reactions at the mineral-H_2O interface (e.g. [19-21]). However, it is necessary that the predictions be compared with reliable experimental measurements, which are often scarce.

Two *in situ* methods that can measure nutrient and contaminant adsorption energies at the mineral-H_2O interface are second harmonic generation (SHG) spectroscopy and flow-adsorption calorimetry. SHG spectroscopy is a nonlinear optical laser-based method capable of surface-specific spectroscopic, kinetic, and thermodynamic adsorption measurements. For example, SHG spectroscopy was recently applied to the investigation of chromate (Cr^{6+}) adsorption at the fused quartz-H_2O interface [22, 23]. Assuming that the SHG-measured Cr^{6+} adsorption isotherm could be analyzed with a simple Langmuir model, the free energy of Cr^{6+} adsorption was estimated to be 38 kJ mol^{-1} at pH 7 [23]. Additional SHG spectroscopic studies are needed to investigate nutrient and contaminant adsorption reactions at the mineral-H_2O interface, particularly using single-crystal mineral surfaces with known structures (i.e., based upon CTR diffraction measurements; see Section 6.2.1).

Many metal oxides in soils lack long-range structural order and are therefore amorphous. Flow-adsorption calorimetry may emerge as an important method to measure the energies of nutrient and contaminant adsorption reactions on amorphous metal oxides. Kabengi *et al.* [24], for example, measured the enthalpies of arsenate (As^{5+}) adsorption on amorphous aluminum hydroxide, using flow-adsorption calorimetry. At pH 5.7, the As^{5+} adsorption reactions were exothermic, with molar heats of adsorption ranging from -3.0 to -66 kJ mol^{-1} [24]. Flow-adsorption calorimetry measurements of nutrient and contaminant adsorption enthalpies (or free energies), using bulk mineral samples, would be particularly valuable for comparison with computational chemistry predictions (e.g. Chapter 3).

6.3 Computational Research

6.3.1 Experimental Measurements and DFT Predictions

Synchrotron-based EXAFS spectroscopic and CTR diffraction measurements have provided unprecedented detail regarding the structures of hydrated, single-crystal mineral surfaces and the binding geometries of nutrient and contaminant complexes. From a computational chemistry standpoint, the adsorption of nutrients and contaminants can now be modeled with increasing confidence on a small number of hydrated soil mineral surfaces, for which the structures are known. Computational chemistry predictions of the binding geometries of nutrient and contaminant complexes provide a direct means to rigorously test and validate experimental interpretations (e.g. Chapter 4). As a result, significant progress is anticipated in our understanding of nutrient and contaminant adsorption mechanisms at the mineral-H_2O interface.

Although the structures of several hydrated, single-crystal mineral surfaces are now known, knowledge of their compositions has remained elusive. In particular, because X-ray scattering methods are insensitive to H atom positions, the protonation states of surface O atoms have not been precisely determined as a function of solution conditions (e.g. pH). Without a complete understanding of both the structure and composition of hydrated soil mineral surfaces, assumptions must be made regarding the protonation states of the surface O atoms. The importance of determining the protonation states of the surface O atoms cannot be overestimated, as they exert an overwhelming influence on nutrient and contaminant adsorption.

Fortunately, significant progress was recently achieved in our understanding of the composition of hydrated, single-crystal mineral surfaces. A seminal study was published that reported both the structure and composition of the hydrated $(1\bar{1}02)$ α-Fe_2O_3 surface [25]. Tanwar *et al.* [25] combined CTR diffraction measurements with periodic density functional theory (DFT) calculations to determine the protonation states of the O atoms on the hydrated $(1\bar{1}02)$ α-Fe_2O_3 surface. The study by Tanwar *et al.* [25] underscores the importance of combining experimental measurements with computational chemistry predictions, in order to advance our understanding of nutrient and contaminant adsorption at the mineral-H_2O interface. However, it remains a sobering reality that the structure and composition have only been determined for one hydrated, single-crystal mineral surface.

Another area of importance regarding the advancement of our understanding of nutrient and contaminant adsorption at the mineral-H_2O interface, from a computational chemistry standpoint, is the development of empirical force fields (i.e., interatomic potentials). A great need exists to develop accurate, empirical force fields which will now be briefly discussed.

6.3.2 Force-Field Development

At present, a realistic theoretical treatment of the interactions of complex soil solutions with mineral surfaces, using large-scale molecular models, is unattainable. Furthermore, the dynamics of nutrient and contaminant adsorption reactions at the mineral-H_2O interface (e.g. outer- versus inner-sphere adsorption or surface precipitation) cannot be reliably predicted. These shortcomings are principally related to the lack of development of accurate, empirical force fields. The development of accurate, empirical force fields is prerequisite to performing classical molecular dynamics (MD) or Monte Carlo (MC) simulations using realistic, large-scale molecular models of mineral surfaces interacting with complex soil solutions. Although quantum MD simulations are much more reliable, such computationally demanding calculations of quasi-environmentally relevant systems have only become possible in recent years (e.g. [26] and Chapter 5). Furthermore, quantum MD simulations of quasi-environmentally relevant systems are currently only practical on time scales of approximately 15 – 25 ps. Therefore, a significant demand remains with respect to the development of accurate, empirical force fields.

Despite the scarcity of accurate, empirical force fields available for environmental systems, progress has been recently achieved. For example, Bandura and coworkers derived force field parameters for TiO_2-H_2O [27] and SnO_2-H_2O [28] surface systems based upon periodic DFT calculations. In addition, Kerisit *et al.* [29, 30] performed classical MD simulations of electrolyte solutions interacting with the (100) goethite (α-FeOOH) surface. Interestingly, the predicted distribution of electrolyte solutions at the (100) α-FeOOH-H_2O interface was significantly different from the classical view based upon electrical double layer theory. In Chapter 5, quantum MD simulations were performed for sulfate and phosphate complexes at the (101) α-FeOOH-H_2O interface. In principle, force field parameters could be derived for these systems, allowing classical MD simulations to be performed on significantly longer time scales.

Though a significant amount of work remains to elucidate the dynamics of nutrient and contaminant adsorption at the mineral-H_2O interface, a bright future lies ahead. The application of computational chemistry methods in this endeavor will be essential. However, greater efforts must be made to integrate experimental results with theoretical predictions based upon computational chemistry calculations.

6.4 References

1. Brown, G. E.; Sturchio, N. C., An Overview of Synchrotron Radiation Applications to Low Temperature Geochemistry and Environmental Science. In *Applications of Synchrotron Radiation in Low-Temperature Geochemistry and Environmental Sciences*, 2002; Vol. 49, pp 1-115.

2. Elzinga, E. J.; Peak, D.; Sparks, D. L., Spectroscopic Studies of Pb(II)-Sulfate Interactions at the Goethite-Water Interface. *Geochimica Et Cosmochimica Acta* **2001,** *65*, (14), 2219-2230.

3. Kim, C. S.; Rytuba, J.; Brown, G. E., EXAFS Study of Mercury(II) Sorption to Fe- and Al-(hydr)oxides - II. Effects of Chloride and Sulfate. *Journal of Colloid and Interface Science* **2004,** *270*, (1), 9-20.

4. Lefevre, G., *In Situ* Fourier-Transform Infrared Spectroscopy Studies of Inorganic Ions Adsorption on Metal Oxides and Hydroxides. *Advances in Colloid and Interface Science* **2004,** *107*, (2-3), 109-123.

5. Duckworth, O. W.; Martin, S. T., Surface Complexation and Dissolution of Hematite by C-1-C-6 Dicarboxylic Acids at pH=5.0. *Geochimica Et Cosmochimica Acta* **2001,** *65*, (23), 4289-4301.

6. Catalano, J. G.; Trainor, T. P.; Eng, P. J.; Waychunas, G. A.; Brown, J. G. E., CTR Diffraction and Grazing-Incidence EXAFS Study of U(VI) Adsorption onto α-Al_2O_3 and α-Fe_2O_3 (1-102) Surfaces. *Geochimica et Cosmochimica Acta* **2005,** *69*, (14), 3555-3572.

7. Waychunas, G.; Trainor, T.; Eng, P.; Catalano, J.; Brown, G.; Davis, J.; Rogers, J.; Bargar, J., Surface Complexation Studied via Combined Grazing-Incidence EXAFS and Surface Diffraction: Arsenate an Hematite (0001) and (10-12). *Analytical and Bioanalytical Chemistry* **2005,** *383*, (1), 12-27.

8. Bargar, J. R.; Towle, S. N.; Brown, G. E.; Parks, G. A., Outer-Sphere Pb(II) Adsorbed at Specific Surface Sites on Single Crystal α-Alumina. *Geochimica Et Cosmochimica Acta* **1996,** *60*, (18), 3541-3547.

9. Bargar, J. R.; Towle, S. N.; Brown, G. E.; Parks, G. A., XAFS and Bond-Valence Determination of the Structures and Compositions of Surface Functional Groups and Pb(II) and Co(II) Sorption Products on Single-Crystal α-Al_2O_3. *Journal of Colloid and Interface Science* **1997,** *185*, (2), 473-492.

10. Towle, S. N.; Brown, G. E.; Parks, G. A., Sorption of Co(II) on Metal Oxide Surfaces I. Identification of Specific Binding Sites of Co(II) on (110) and (001) Surfaces of TiO_2 (Rutile) by Grazing-Incidence XAFS Spectroscopy. *Journal of Colloid and Interface Science* **1999,** *217*, (2), 299-311.

11. Towle, S. N.; Bargar, J. R.; Brown, G. E.; Parks, G. A., Sorption of Co(II) on Metal Oxide Surfaces II. Identification of Co(II)(aq) Adsorption Sites on the

(0001) and (1-102) Surfaces of α-Al_2O_3 by Grazing-Incidence XAFS Spectroscopy. *Journal of Colloid and Interface Science* **1999,** *217*, (2), 312-321.

12. Trainor, T. P.; Fitts, J. P.; Templeton, A. S.; Grolimund, D.; Brown, G. E., Grazing-Incidence XAFS Study of Aqueous Zn(II) Sorption on α-Al_2O_3 Single Crystals. *Journal of Colloid and Interface Science* **2001,** *244*, (2), 239-244.

13. Den Auwer, C.; Drot, R.; Simoni, E.; Conradson, S. D.; Gailhanou, M.; de Leon, J. M., Grazing Incidence XAFS Spectroscopy of Uranyl Sorbed onto TiO_2 Rutile Surfaces. *New Journal of Chemistry* **2003,** *27*, (3), 648-655.

14. Denecke, M. A.; Rothe, J.; Dardenne, K.; Lindqvist-Reis, P., Grazing Incidence (GI) XAFS Measurements of Hf(IV) and U(VI) Sorption onto Mineral Surfaces. *Physical Chemistry Chemical Physics* **2003,** *5*, (5), 939-946.

15. Eng, P. J.; Trainor, T. P.; Brown, G. E.; Waychunas, G. A.; Newville, M.; Sutton, S. R.; Rivers, M. L., Structure of the Hydrated α-Al_2O_3 (0001) Surface. *Science* **2000,** *288*, (5468), 1029-1033.

16. Catalano, J. G.; Park, C.; Zhang, Z.; Fenter, P., Termination and Water Adsorption at the α-Al_2O_3 (012) - Aqueous Solution Interface. *Langmuir* **2006,** *22*, (10), 4668-4673.

17. Trainor, T. P.; Chaka, A. M.; Eng, P. J.; Newville, M.; Waychunas, G. A.; Catalano, J. G.; Brown, G. E., Structure and Reactivity of the Hydrated Hematite (0001) Surface. *Surface Science* **2004,** *573*, (2), 204-224.

18. Trainor, T. P.; Eng, P. J.; Brown, G. E.; Robinson, I. K.; De Santis, M., Crystal Truncation Rod Diffraction Study of the α-Al_2O_3 (1-102) Surface. *Surface Science* **2002,** *496*, (3), 238-250.

19. Kwon, K. D.; Kubicki, J. D., Molecular Orbital Theory Study on Surface Complex Structures of Phosphates to Iron Hydroxides: Calculation of Vibrational Frequencies and Adsorption Energies. *Langmuir* **2004,** *20*, (21), 9249-9254.

20. Paul, K. W.; Kubicki, J. D.; Sparks, D. L., Quantum Chemical Calculations of Sulfate Adsorption at the Al- and Fe-(Hydr)oxide-H_2O Interface-Estimation of Gibbs Free Energies. *Environmental Science and Technology* **2006,** *40*, (24), 7717-7724.

21. Zhang, N. L.; Blowers, P.; Farrell, J., Evaluation of Density Functional Theory Methods for Studying Chemisorption of Arsenite on Ferric Hydroxides. *Environmental Science and Technology* **2005,** *39*, (13), 4816-4822.

22. Mifflin, A. L.; Gerth, K. A.; Geiger, F. M., Kinetics of chromate adsorption and desorption at fused quartz/water interfaces studied by second harmonic generation. *Journal of Physical Chemistry A* **2003,** *107*, (45), 9620-9627.

23. Mifflin, A. L.; Gerth, K. A.; Weiss, B. M.; Geiger, F. M., Surface studies of chromate binding to fused quartz/water interfaces. *Journal of Physical Chemistry A* **2003,** *107*, (32), 6212-6217.

24. Kabengi, N. J.; Daroub, S. H.; Rhue, R. D., Energetics of Arsenate Sorption on Amorphous Aluminum Hydroxides Studied Using Flow Adsorption Calorimetry. *Journal of Colloid and Interface Science* **2006,** *297*, (1), 86-94.

25. Tanwar, K. S.; Lo, C. S.; Eng, P. J.; Catalano, J. G.; Walko, D. A.; Brown, J. G. E.; Waychunas, G. A.; Chaka, A. M.; Trainor, T. P., Surface Diffraction Study of the Hydrated Hematite (1-102) Surface. *Surface Science* **2007,** *601*, (2), 460-474.

26. Tunega, D.; Gerzabek, M. H.; Haberhauer, G.; Lischka, H., Formation of 2,4-D complexes on Montmorillonites - An *Ab Initio* Molecular Dynamics Study. *European Journal of Soil Science* **2007,** *58*, (3), 680-691.

27. Bandura, A. V.; Kubicki, J. D., Derivation of Force Field Parameters for TiO_2-H_2O Systems from *Ab Initio* Calculations. *Journal of Physical Chemistry B* **2003,** *107*, (40), 11072-11081.

28. Bandura, A. V.; Sofo, J. O.; Kubicki, J. D., Derivation of Force Field Parameters for SnO_2-H_2O Surface Systems from Plane-Wave Density Functional Theory Calculations. *J. Phys. Chem. B* **2006,** *110*, (16), 8386-8397.

29. Kerisit, S.; Cooke, D. J.; Marmier, A.; Parker, S. C., Atomistic Simulation of Charged Iron Oxyhydroxide Surfaces in Contact with Aqueous Solution. *Chemical Communications* **2005**, (24), 3027-3029.

30. Kerisit, S.; Ilton, E. S.; Parker, S. C., Molecular Dynamics Simulations of Electrolyte Solutions at the (100) Goethite Surface. *J. Phys. Chem. B* **2006,** *110*, (41), 20491-20501.

Appendix A

CHAPTER 2 COPYRIGHT PERMISSIONS

Reproduced in part with permission from Paul, K. W.; Borda, M. J.; Kubicki, J. D.; Sparks, D. L., Effect of Dehydration on Sulfate Coordination and Speciation at the Fe-(hydr)oxide-Water Interface: A Molecular Orbital/Density Functional Theory and Fourier Transform Infrared Spectroscopic Investigation. *Langmuir* **2005,** *21*, (24), 11071-11078. DOI: 10.1021/la050648v. Copyright © 2005 American Chemical Society.

Appendix B

CHAPTER 3 COPYRIGHT PERMISSIONS

Reproduced in part with permission from Paul, K. W.; Kubicki, J. D.; Sparks, D. L., Quantum Chemical Calculations of Sulfate Adsorption at the Al- and Fe-(Hydr)oxide-H_2O Interface-Estimation of Gibbs Free Energies. *Environmental Science and Technology* **2006,** *40*, (24), 7717-7724. DOI: 10.1021/es061139y. Copyright © 2006 American Chemical Society.

Appendix C

CHAPTER 4 COPYRIGHT PERMISSIONS

Reproduced in part with permission from Paul, K. W.; Kubicki, J. D.; Sparks, D. L., Sulphate Adsorption at the Fe (hydr)oxide-H_2O Interface: Comparison of Cluster and Periodic Slab DFT Predictions. *European Journal of Soil Science* **2007,** *58*, (4), 978-988. DOI: 10.1111/j.1365-2389.2007.00936.x. Copyright © 2007 Published with the British Society of Soil Science and Blackwell Publishing Ltd. on behalf of the National Societies of Soil Science in Europe.

Appendix D

CHAPTER 5 COPYRIGHT PERMISSIONS